UNIVERSITÀ DEGLI STUDI DI PARMA

Dottorato di ricerca in Farmacologia e Tossicologia Sperimentali

Ciclo XXVII

TOWARDS THE IDENTIFICATION OF STRUCTURAL DETERMINANTS OF TOXICITY OF AMORPHOUS SILICA NANOPARTICLES AND CARBON NANOTUBES: AN IN VITRO STUDY

Coordinatore:
Chiar.ma Prof.ssa Elisabetta Barocelli

Tutor:
Chiar.mo Prof. Ovidio Bussolati

Dottoranda: Luisana Di Cristo

Triennio 2012-14

TABLE OF CONTENTS

LIST OF ABBREVIATIONS

ASNP	Amorphous silica nanoparticles
BSA	Bovine serum albumin
CM-H_2DCF-DA	5-(and-6)-chloromethyl-2',7' dichlorodihydrofluorescein diacetate, acetyl ester
CNT	Carbon nanotubes
DAN	2,3- diaminonaphthalene
DAPI	4',6-diamidino-2-phenylindole
ELISA	Enzyme-linked immunosorbent assay
FBS	Fetal bovine serum
GAPDH	Glyceraldehyde 3-phosphate dehydrogenase
HIM	He-Ion Microscopy
HMOX-1	Heme oxygenase-1
IL-1 β	Interleukin-1beta
IL-6	Interleukin-6
LPS	Lipopolysaccharides
MWCNT	Multi-walled carbon nanotubes
NM	Nanomaterials
NO	Nitric oxide
Nos2	Nitric oxide synthase inducible
NP	Nanoparticles
PBS	Phosphate Buffered Saline
PCR	Polymerase Chain Reaction
ROS	Reactive oxygen species
SDS	Sodium dodecyl sulfate
SiO_2	Silicon dioxide
SWCNT	Single-walled carbon nanotubes
TBS	Tris-buffered saline
TEER	Trans-epithelial electrical resistance
TNF- α	Tumor necrosis factor-alpha

ABSTRACT

Nanomaterials (NM) contain particles, in an unbound state or as an aggregate or as an agglomerate, which, for a percentage of 50% or more, have one or more external dimensions in the range 1-100 nm. The great development of nanotechnology has produced an increasing quantity of nanomaterials of different types in several productive sectors (food, chemicals, pharmaceuticals). For this reason, several studies are aimed at characterizing the physical and chemical properties of nanomaterials and the determination of their effects on human health and the environment.

Multi walled carbon nanotubes (MWCNT) and amorphous silica nanoparticles (ASNP) are examples of nanomaterials widely used in many industrial fields. The overall aim of this thesis is the elucidation of the potential hazards of MWCNT and ASNP, evaluating their interaction with relevant cell models. Attention is given to the assessment of potential toxic effects on cells of innate immunity and to the identification of structural determinants of toxicity.

Since inhalation is the major way of interaction with nanomaterials, we decided to study the biological effects of MWCNT and ASNP on two cell lines (MH-S and RAW264.7), as representative models of macrophages, which are the first to contact the inhaled particles, and on airway epithelial cells (Calu-3), which represents one of the first body barriers encountered by nanomaterials dispersed in the environment.

The first part of the thesis is focused on the identification of structural determinants of toxicity, *in vitro*, of four preparations of multi-walled carbon nanotubes with different length, morphology (rigid, *needle-like* or flexible, *tangle-like* shape), and level of metal contaminants. We have assessed the biological effects of the four MWCNT preparations (NM400, NM401, NM402 and MWCNT-SA) on macrophages and airway epithelial cells, in order to identify the determinants of toxicity, thus far incompletely elucidated. To study the biological effects of MWCNT on macrophage cell lines we analyzed different endpoints, such as cell viability, phagocytic activity and pro-inflammatory M1 macrophage activation. We found that the main determinants of toxicity for macrophages are the length and the *needle-like* shape, which hinder, or even prevent, phagocytosis. Indeed, the greater toxicity of NM401 and MWCNT-SA, as demonstrated by the decrease in cell viability and the alteration of functional activity, are ascribable to their greater length and to their morphological features. On the contrary, reduced length and *tangle-like* shape (NM400 and NM402) promote M1 macrophage activation. Since these materials can be engulfed by macrophages, these results suggest that phagocytosis is a main step for the M1 macrophage activation by nanomaterials, endowed with low acute toxicity.

Given the high tendency of MWCNT to aggregate and the presence of aggregates in the airway walls of exposed animals, as reported in several *in vivo* studies, we have investigated if MWCNT produced a barrier impairment. The behavior of epithelial cells was studied both at the monolayer (cell population) and at the single-cell level. At a cell-population level, Trans-Epithelial Electrical Resistance (TEER) was used as a synthetic indicator of barrier competence, caspase activity was assessed with standard biochemical assays, and cell viability was investigated with both standard biochemical techniques and an high throughput (HTP) technique, based on automated epifluorescence microscopy; at single-cell level, cell responses to MWCNT were investigated with confocal microscopy, by evaluating cell death (calcein/propidium iodide), proliferation (Ki-67), inflammation triggering (NF-κB) and apoptosis (caspase activity). We found that the main determinant of toxicity for epithelial cells depends on the actual shape in which MWCNT get in contact with the cells and, in particular, if they form aggregates.

The second part of the thesis is focused on the identification of structural determinants of toxicity of two preparations of amorphous silica nanoparticles (ASNP, a material usually considered endowed with modest toxicity). This study has evaluated the capability of ASNP, of comparable size and specific surface area, but produced through different synthetic procedures (colloidal NM200 *vs* pyrogenic NM203), to induce macrophage activation in MH-S and RAW264.7 cell lines. To study the biological effects of ASNP we analyzed different endpoints, such as cell viability, oxidative stress (ROS formation and the induction of *Hmox-1*), the induction of the inducible nitric oxide synthase *Nos2*, the production of NO and the secretion of cytokines like TNF-α, IL-6 and IL-1β. Helium Ion microscopy (HIM) and confocal microscopy were adopted for imaging the interaction between ASNP and the cell surface. The results demonstrate that pyrogenic ASNP are more potentially inflammogenic than colloidal ASNP. Moreover, an additional mechanism of toxicity is proposed, consisting in the greater capability of pyrogenic ASNP to bind biologically active compounds, such as LPS, enhancing their effects. Thus we found that the preparation route procedure may constitute a main determinant of toxicity of ASNP, likely because of the different surface chemistry established by high-temperature synthesis.

In conclusion, this thesis highlights that determinants of toxicity of nanomaterials are strongly dependent on several parameters. The identification of these determinants, which appear essential for a "safety-by-design" approach, will therefore require an in-depth characterization of the toxicological properties of each type of nanomaterial.

CHAPTER 1

INTRODUCTION

1.1 Nanotechnology and nanoparticles

1.1.1 Nanotechnology

Nanotechnology is the understanding and control of matter at dimensions between approximately 1 and 100 nanometers, where unique phenomena enable novel applications. Encompassing nanoscale science, engineering, and technology, nanotechnology involves imaging, measuring, modelling and manipulating matter at this length scale. Unusual physical, chemical, and biological properties can emerge in materials at the nanoscale. These properties may differ in important ways from the properties of bulk materials and single atoms or molecules.

Nanotechnology has been recognized as a revolutionary field of science and technology, comparable to the introduction of electricity, biotechnology, and digital information revolutions. Between 2001 and 2008, the numbers of discoveries, inventions, nanotechnology workers and markets all increased by an average annual rate of 25 percent. The global market value for nanotechnology is expected to increase to nearly $27 billion in 2015. Current trends suggest that the number of nanotechnology workers and products worldwide will double every three years, reaching a $3 trillion market with 6 million jobs by 2020. There is the potential to incorporate nanotechnology-enabled products and services into almost all industrial sectors and medical fields. The increasing integration of nanoscale science and engineering promises mass applications of nanotechnology in industry, medicine, and computing, and in conservation of nature.

The areas of nanotechnology involve a wide range of applications: energy (production, catalysis, accumulation), consumer products (lubricants, abrasives, paints, rubber, sportswear), electronic components (chips, screens), reconditioning (absorption of pollutants, water filtration, disinfection), medicine (diagnosis, drug delivery), cosmetics (creams and sunscreens), textiles and even food (additives, packaging).

Nanotechnologies play a relevant role in the following areas:

<u>Microelectronics and semiconductors</u>

1. “Nano on Micro” (integration of nanomaterials on micro-finished sensors and biochip platforms).

2. Optoelectronic and photonic component technologies (nanotechnologies for high-level of optical component and of a new generation of sensors).

Chemistry

1. Nanomaterials for chemical catalysis (nanomaterials for solid catalyst, for catalyst membranes, of high-efficiency and sustainable gas purification and storage).

2. Food packaging (nanomaterials able to extend the shelf-live, sensors for the monitoring of the preservation of the packaged contents).

3. Concrete-based formulas for the construction industry (new potential technological discontinuity due to nanoscale control of the structure of matter).

Pharmaceutics and biotechnologies

1. Medical applications of nanotechnologies (drug delivery systems, nanomaterials for medical devices, biosensors, nano-scalpels, new *in vivo* imaging diagnostic systems, mixed “theragnostic” devices for either therapeutic and diagnostic purposes).

2. Transportation systems (phospholipid particles containing molecules with a pharmacological activity for targeted drug delivery).

Energy

1. Innovative technologies for solar energy development (third-generation photovoltaic technologies: semiconductor crystals; nanoscale network for organic solar cells)

2. Hydrogen storage technologies (solid storage in alloys and innovative intermetallic compounds, nanostructured oxides, etc.).

Environment

1. New technologies for water treatment and reuse (development of new zeolitelike nanoporous materials).

2. Systems for pollution reduction and quality air control (sensitive nanostructured materials, sensors, catalysts).

The growing production of these materials and the relative potential exposure risk for an increasing number of workers, make it necessary to implement the knowledge on the potential biological effects (either at the molecular-cellular or organ-system level).

1.1.2 Definition of Nanoparticles

On 18 October 2011 the European Commission adopted the Recommendation on the definition of a nanomaterial (2011/696/EU). According to this Recommendation a "Nanomaterial (NM)" means:

A natural, incidental or manufactured material containing particles, in an unbound state or as an aggregate or as an agglomerate and where, for 50 % or more of the particles in the number size distribution, one or more external dimensions is in the size range 1 nm - 100 nm.

In specific cases and where warranted by concerns for the environment, health, safety or competitiveness the number size distribution threshold of 50 % may be replaced by a threshold between 1 and 50 %. By derogation from the above, fullerenes, graphene flakes and single wall carbon nanotubes with one or more external dimensions below 1 nm should be considered as nanomaterials.

The definition will be used primarily to identify materials for which special provisions might apply (e.g. for risk assessment or ingredient labelling). Those special provisions are not part of the definition but of specific legislation in which the definition will be used.

Nanomaterials (NMs) are not intrinsically hazardous per se but there may be a need to take into account specific considerations in their risk assessment. Therefore one purpose of the definition is to provide clear and unambiguous criteria to identify materials for which such considerations apply. It is only the results of the risk assessment that will determine whether the nanomaterial is hazardous and whether or not further action is justified.

Today there are several pieces of EU legislation, and technical guidance supporting implementation of legislation, with specific references to nanomaterials. To ensure conformity across legislative areas, where often the same materials are used in different contexts, the purpose of the Recommendation is to enable a coherent cross-cutting reference. Therefore, another basic purpose is to ensure that a material which is a nanomaterial in one sector will also be treated as such when it is used in another sector.

1.1.3 Origin of Nanoparticles

Nanoparticles (NP) can be divided into:

- natural particles
- anthropogenic particles formed as a by-product, mostly during combustion
- anthropogenic particles produced intentionally due to their particular characteristics
- (ENP, Engineered Nanoparticles or ENM, Engineered Nanomaterials)

The natural NP are divided into biogenic (such as humic and fulvic acids or virus), geogenic (originate from geosphere as metal particles or carbon), and pyrogenic (produced during combustion, for example the emission of volcanic fumes). The anthropogenic NP formed as a by-product are, for example, those obtained during the combustion in internal combustion engines or those that can be unintentionally released into the atmosphere by the work in mines.

Engineered nanoparticles represent the last frontier of the Industry. They can be further subdivided according to the production process: "top down" or "bottom up" techniques[1]. Top-down processing involves cutting or milling of a larger single sample of material to obtain the nanoscale material in the desired configuration, while bottom-up approaches assemble smaller subunits to obtain the larger nanoscale material through processes such as the chemical synthesis. Many top-down applications, such as the lithographic processes used to manufacture computer chips have been used for years, while other bottom-up approaches, such as the production of carbon nanotubes (CNT), are relatively new.

It should be stressed that the specific technique used to produce a nanoscale material could influence the human health risk associated with that material[2], especially when the surface characteristixcs of the particle are modified This peculiarity must be considered in the investigations concerning the toxic properties of nanomaterials (see below). Indeed, the extremely small size of the ENP gives the engineered nanomaterials novel properties, mainly due to the following aspect: an high surface area that allows the possibility, for these materials, to provide a "wide exchange surface for the reactions, considering that the 40 - 50% of their atoms are on the surface[3-4]. Compared to the bulk, the results are a greater chemical reactivity, different physico-chemical and electromagnetic properties. Examples of engineered NP are fullerenes and CNT, both pristine and functionalized, and metals and metal oxides, such as TiO_2 and Ag NP.

1.1.4 Classification of Nanoparticles

Many NMs used in nanotechnologies consist of NPs or fibrous materials that are initially produced as aerosols or colloidal suspensions. The Organization for Economic Co-operation and Development (OECD) has subdivided most of NMs produced today, or about to enter the market, into the following types[5]:

- Fullerenes (C60)*:* any molecule composed entirely of carbon, in the form of a hollow sphere or cage. The most known of fullerenes is the C60 which consists of 60 carbon atoms, arranged to form a sphere made up of pentagon or hexagon panels.
- Carbon Nanotubes (CNT): They may be single-walled (SWCNT) or multi-walled (MWCNT) depending on the number of coaxial layers they are made up. Because of their dimensions (length/diameter ratio, the aspect ratio, >3), they fall under the category of fibers, they are highly electrostatic and appear agglomerated in beams or filaments with a diameter of approximately 20 to 50 nm. As the productive process involves the use of metallic catalysts, the final product may contain metals, such as iron, nickel, aluminium, or cobalt.
- Metallic, metal-oxide or metalloid-oxide materials such as:
    - Silver, gold and iron NPs
    - Titanium and silicon dioxides
    - Aluminium, cerium and zinc oxides
- Carbon black
- Polystyrene
- Dendrimers: nanoscale synthetic polymers built up from branched units (from the Greek, *dendron* - tree). The surfaces of dendrimers are characterized by several chain terminals which can be adapted enabling specific chemical functions (their use, for example, as catalysts or drug vectors due to the inner cavities in their 3D structure)
- Nanoclays: NPs of layered mineral clays
- Nanodots: nanoscale crystalline structures made from cadmium, selenium, tellurium and sulphur; their nominal diameter is of the order of some nanometres; they can be found suspended in a vehiculated agent or englobed in a solid (polystyrene, polyurethane, polycarbonate, silicium).
- Carbon nanofoam: it is the fifth known allotropic form of carbon, and consists of a cluster assembly of carbon atoms with a diameter of 6-9 nm, casually linked in a fabric-like structure. It is an extremely light, porous semiconductor solid that exhibits magnetic properties and contains impurities such as iron and nickel.
- Quantum dots: crystalline NPs with specific size-dependent properties due to the effects of the quantum confinement on the electrons.

1.1.5 Physico-chemical properties of nanoparticles

One of the most active research lines in this field is investigating on whether NM exposure represents a risk to workers' health and to what extent the chemico-physical and chemical properties may influence such risk. Different studies demonstrated that the presence of NM and aerosols in various workplaces, either intentionally produced and manipulated or involuntary released during particular physicochemical processes, may represent potential risks to workers' health and safety, on the basis of experimental evidences supporting a correlation between exposure and diseases affecting, in particular, the respiratory tract and the immune and nervous systems[6-7].

Particular attention must be focused on the metrological aspects, since different parameters (such as dimensions, mass, chemical composition, surface area, concentration, aggregation and agglomeration state, water solubility, surface chemistry and morphological structure) may contribute to the hazardous interactions of NP with the human body. The surface and the shell properties are of great interest as they are the points through which NP come in contact with organisms[8]. As for dimensions, it has been demonstrated that they deeply influence the site of deposition of NPs (in particular, in the respiratory tract) which is likely the alveoli for those particles with a diameter smaller than 100 nm[9-12]. Also, NP may move into the cells through the membrane and translocate, via diffusion, into other parts of the organism eluding alveolar macrophages and penetrating into the pulmonary interstitium, although this has not yet been demonstrated in humans[13-14]. Shrinkage in size may create discontinuous crystal planes that increase the number of structural defects and disrupt the well-structured electronic configuration of the material[15]. The aggregation/agglomeration states may exert a major influence on deposition, local toxicity and toxic kinetics of NP, due to significant variations of the diameter (wider in aggregates) and of the reduction of the surface area occupied by NP; hence, the behaviour of large NP aggregates may be compared to that of the ultrafine particles which are common air pollutant [16-17]. Aggregation/agglomeration depends upon the inner features and concentration (expressed as number of particles per unit of volume) of NP but also upon the properties of the medium in which they are contained (pH, ionic force, other solutes present in the medium)[8].

The volume occupied by particles and the mass decrease with dimensions but, consequently, the surface area per unit mass, as well as the potential for biological interactions, increases [9, 17, 18]. As the particle reduces its dimensions, in fact, the percentage of atoms localized on the surface increases depending upon the percentage of atoms occupying the rest of the volume. This may exert a significant influence on both the charge surface composition and the catalytic activities of the surface and may determine an increase in the number of potential reactive groups on the cell surface[9, 15, 18-20]. Hence, reactive groups may, supposedly, modify the biological activity of NP and

may be crucial for the definition of their toxicity. For NP of the same chemical composition, therefore, different surface areas per unit mass are extremely relevant parameter for predicting toxicity[9].

Surface reactivity is correlated with the chemical composition of the particle itself (presence of reactive groups on the surface), surface charge (deeply influencing the deposition of particles at the pulmonary level), catalytic activity, absorption and desorption capacities of molecules, imperfections in crystals and impurities[9, 20-22]. Also the porosity contributes to a significant increase in the total surface area which is to be added to the geometric surface area[23]. In some cases, an increased surface reactivity (and a consequent increased biological activity) produces positive effects (such as, for example, antioxidant activity, or transportation and release of therapeutic substances, due to a large penetration capacity of NP); in other cases, toxic effects may appear (such as the induction of oxidative stress and cytotoxicity)[9, 20, 21, 24], and sometimes positive and toxic effects may simultaneously appear [9, 21]. Finally, surface reactivity is fundamental to define the interactions between NP and biological macromolecules (proteins, elements of the cytoskeleton; collagen, membrane structures, receptors, DNA, etc.). In many cases, specific coatings may be used to modify NP surface properties, reduce their reactivity, prevent aggregation or agglomeration, favour dispersion and keep the main properties unaltered. However, translocation of particles from the respiratory tract to the systemic circulation can be accelerated by altering the distribution of NP in the human body[19, 25-33]. NP shape is another fundamental parameter that potentially affects toxicity. It is known that also porosity influences deposition and absorption of NP in the human body.

Fibrous materials deserve separate consideration. Indeed, it is known that exposure to fibres increases the risk of fibrosis and lung cancer after prolonged exposure. For these materials, the major parameters for evaluating NP toxicity are doses, size and bio-persistence. The penetration of fibres in lungs depends only indirectly upon the diameter. This is particularly true for some NPs of great industrial interest, such as carbon nanotubes [3, 9].

On the basis of some studies[22, 33] the European Agency for Safety and Health at Work (EU-OSHA, 2009) has proposed to consider the following parameters to perform toxicology studies under controlled conditions: size, shape, surface area, surface chemistry, charge (in biological fluids), composition, solubility, crystalline structure, aggregation/agglomeration.

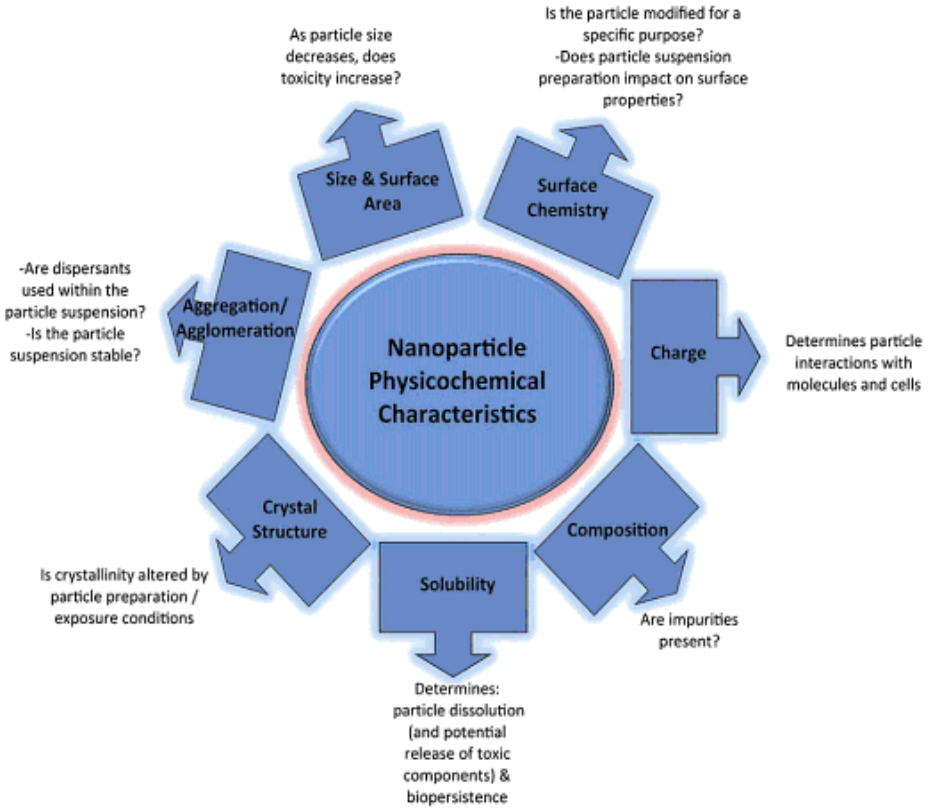

Figure 1. Engineered nanomaterials physicochemical properties. Physico-chemical properties of nanomaterials that should be considered with high priority in the toxicological assessments are outlined[34].

1.2 Nanotoxicology: Health effects

1.2.1 Nanotoxicology

The growing production and use of engineered nanomaterials in workplaces, the potential exposure risk for an increasing number of workers and the paucity of data available on health risks associated with such compounds make it necessary to implement the knowledge regarding the potential biological effects (either at the molecular-cellular or organ-system level). Due to the recent production, dissemination and use of engineered nanomaterials and the complexity of exposure assessment, no epidemiological studies and information on the toxic effect of NMs on exposed populations are available today. Any existing information on potential adverse effects is largely

based on animal and *in vitro* studies with (human and animal) cell lines or primary cultures. The relevance of *in vitro* studies for the *in vivo* effects may be limited, although they are useful for screening purposed and mechanistic studies[35]. Figure 2 shows the potential interactions of ENM with the cell and subcellular structures, and indicates possible mechanisms of action of ENM.

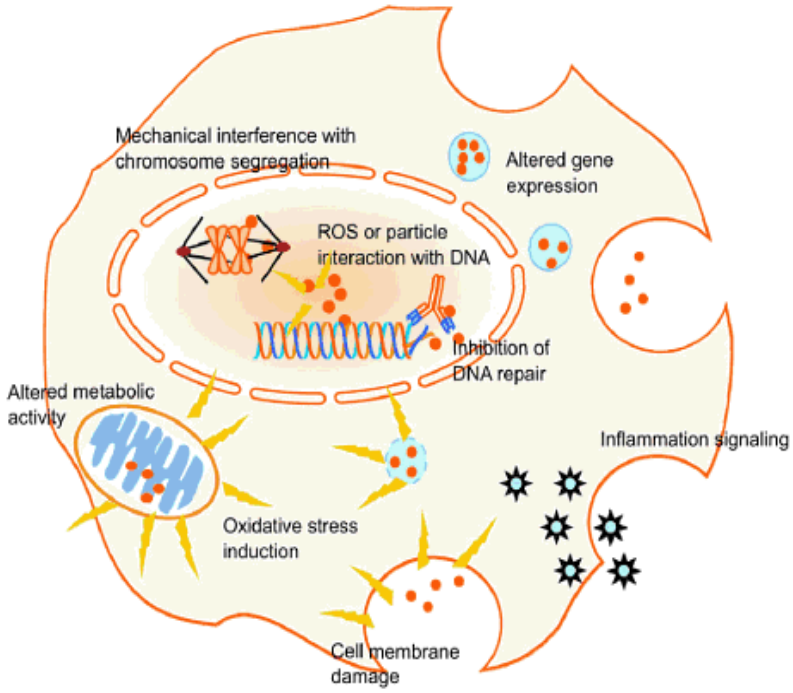

Figure 2. Possible interactions of ENM with the cell and subcellular structures. Suggested mechanisms underlying nanoparticle-induced responses at the cellular level which, at sufficiently high or persistent levels, can lead to altered tissue function and damage[34].

1.2.2 Genotoxic and oxidative effects

Most of the studies on the effects of NM have focused on high-dose exposures. Recent research data, on the exposure to low concentration of engineered NM, however, demonstrated that they may cause DNA damage and induce oxidative and inflammatory effects that could be involved in the carcinogenic process[36]; great uncertainty, however, still exists and results remain contradictory. Most of these studies use carbon nanotubes and metal oxide particles which may cause, directly or indirectly, DNA damage by induction of oxidative stress. The genotoxic effects of NM are dependent on size, high surface area and chemico-physical properties (such as metal contaminants, in the case of CNT, and surface charges), which determine their reactivity and aggregation state.

These properties give NM unexpected genotoxic properties which make complex the study of their effects and mechanisms of action[21]. According to their size and state of aggregation, NM are able to penetrate the cell by passive diffusion or receptor-mediated or protein-mediated endocytosis, then they enter the nucleus through the nuclear membrane (if sufficiently small), through the nuclear pore complexes or after the dissolution of the nuclear membrane during the cell division (if large or aggregated). Once penetrated in the nucleus, they can damage the genetic material directly through the interaction with the DNA and histone proteins or indirectly through the inhibition of nuclear proteins involved in the processes of DNA replication and transcription. The genotoxic damage can be indirectly induced also through the interaction with other cell proteins like those involved in the cell division process, through the induction of oxygen free radicals, produced for instance during triggered inflammatory processes, or through altered functionality of proteins involved in the DNA damage recovery.

1.2.3 Respiratory effects

Given that inhalation is the primary route of NP uptake, lungs are the main target organ for NP toxicity. Furthermore,. While airways are a strong barrier to NP penetration, in the alveoli the interstitial thickness is of only 5 μm since gas exchange between air and blood do take place at this site. . As most of the engineered NP are present in both occupational and environmental settings as aerosols or colloidal suspensions, the lung exposure resulting from inhalation is the most likely route of human exposure [37]. Spherical NPs deposit in lung regions according to their size and physical structure[3]. Once deposited in the alveoli, spherical NPs appear to translocate into the pulmonary interstitial sites probably by transcytosis and, then, penetrate into the systemic circulation. Unlike spherical NPs, fibre-like particles (i.e. carbon nanotubes) are not completely enclosed by macrophages produced frustrated phagocytosis, and, they cannot be effectively cleared. therefore[38].

1.2.4 Dermal effects

Dermal exposure to NPs may induce irritative and allergic local effects on the skin that may represent the entryway into systemic circulation. To date, few data are available on dermal risks associated to NPs but preliminary experimental results suggest their potential ability to trigger dermal effects and penetrate skin layers; however, today, further research on the wide range of NP is recommended as their diffusion since dermal effects on the skin may differ significantly. For

example, the exposure to carbon nanotubes and to TiO_2 NP is known to induce different dermal effects [39-40]. Additionally, to date, most of the knowledge in this field comes from the pharmaceutical industry which has observed the effects of titanium dioxide (TiO_2) and zinc oxide (ZnO) nanoparticles used in skin care formulations, whereas very little information relating to other type of NPs is available.

1.2.5 Immunological effects

Giving special attention to the immune system is well justified in the context of nanosafety. Immune cells are enriched close to body surfaces (like skin, airways, gastrointestinal tract), where pathogenic microorganisms, but also nanomaterials, are most likely to enter the body. Since engineered nanoparticles are not associated with dangerous pathogens, most immune mechanisms do not come into play as they are not the appropriate response. Activation of cellular stress mechanisms may occur if nanoparticles do act as stressors, but full-blown immune responses like those involving inflammation, complement activation or antibody production are not useful and may even be detrimental to the organism itself, so the decision of tolerance is usually the most appropriate. Tolerance is not the same as failure to recognize non-self. The decision for tolerance is an active one and is reinforced by immune mechanisms preventing future response, like making reactiveT cells permanently unresponsive (anergic) or inducing regulatory T cells (Treg) which maintain tolerance by secreting immunosuppressive cytochines[41-42]. Innate immunity cells, and in particular macrophages, are professional defense cells and their paramount role is to patrol the body looking for potential dangers. In this perspective, it is likely that immune cells meet and handle nanomaterials more frequently than many other cell types. Phagocytic immune cells are also often the first to come in contact with nanomaterials, either in blood (for instance when NP are used in nanomedicine), at the body surfaces (in particular respiratory mucosa, gastrointestinal tract, skin) and the internal tissues (e.g. in case of wounds or after extravasation). The scarce data (mostly *in vitro*) currently available on the potential effects of NPs on the immune system suggest that NP, once entered the systemic circulation, might be able to interact with proteins deposited or circulating on the cell surface, thereby exposing amino acid residues normally not exposed (cryptic epitopes), and stimulating a potential autoimmune response[43]. Another potential damage mechanism may be triggered by the interference with opsonization processes and, as a consequence, with the clearance of foreign materials (i.e. microorganisms) usually eliminated by the process itself[44]. *In vivo* studies demonstrated a series of potential effects of CNT on the immune system. Koyama et al, 2006[45] evaluated the immune response of rats to subcutaneous administration of

single-walled carbon nanotubes (SWCNT) and multi-walled carbon nanotubes (MWCNT) for 3 months. Authors observed that this material is able to induce major histocompatibility complex Class I and Class II within two weeks from administration. This response could underlie the peculiar hystopathological picture (granuloma formation) detected after lung exposure.

An indirect correlation between engineered NP and the immune system is represented by the interaction between nanoparticles and the natural history of diseases with an immune component such as amyloidosis. Primary amyloidosis is induced by monoclonal alterations of plasma cells (cells normally involved in the humoral adaptive immune response) responsible for the extracellular deposition of the fibrillar substance called amyloid. Linse et al, 2007[46] observed that the presence of MWCNTs induced a dose-dependent increase in the formation of the critical nucleus, a crucial stage in the fibril formation. Therefore, the interaction with engineered NP might reveal or accelerate the course of some autoimmune diseases.

However due to the high doses used, existing data are insufficient to conclusively express an opinion regarding toxic effects of engineered NPs on the immune system

1.2.6 Gastrointestinal tract effects

Despite substantial ongoing research effort in the nanotoxicology field, relatively little attention has been given to the impact, behavior and interaction of ENM in the gastrointestinal tract (GIT). The widespread use of NM such silver, zinc, titanium and amorphous silica nanoparticles in food packaging and drug industry, carries a clear risk of ingestion for a large proportion of the population. Furthermore, the more widely studied inhalation route of ENM will also result in secondary exposure of GIT following clearance from the respiratory tract. It is clear that multiple routes exist for ENM to cross the GIT epithelial barrier and to be disseminated throughout the body, raising the possibility that ingested ENM may have adverse effects in peripheral organs. Significant uptake of some ENM (e.g. copper, silver and gold) has been demonstrated in animal models following oral administration but these studies have largely focused on relatively high doses[47-50]. The highly acidic environment encountered in the stomach has been proposed to play a major role in the toxicity of copper NP triggering release of ions[51].

Most *in vitro* assessments of ENM uptake and toxicity in GIT cells has focused on the Caco-2 adenocarcinoma cell line. For example a range of food-related ENM, including TiO_2, SiO_2 and ZnO, induced significant cytotoxicity and oxidative DNA damage in cultured Caco-2 cells[52], but the significance of these findings for real GIT exposure remains uncertain due to limitation of these studies to non-polarized cells, which poorly reflect the GIT epithelium, and the continuing

uncertainty about realistic exposure levels. Animal studies and cell culture models have highlighted the potential high capacity uptake route provided by the specialized M cells and also demonstrated that these specialized cells, which are massively outnumbered by other enterocytes, are not the only portal for ENM penetration of the GIT wall. It is not yet clear to what extent uptake routes differ for ENM types and the extent to which additional barrier (e.g. mucus and glycocalyx) and the changing GIT environment affect/influence ENM uptake[53-54].Significant questions remain about the potential for ENM to have adverse effects in GIT or elsewhere, via GIT uptake. To date studies have identified several potential uptake and toxicity mechanisms that will require further research to be fully characterized.

1.3 Carbon nanotubes

Carbon nanotubes (CNT), a distinct molecular form of carbon atoms that was discovered in the late 1980s, were first described by Sumio Iijima in 1991. Essentially, CNT are cylindrical molecules composed solely of carbon atoms. The simplest type of CNT is the single-walled CNT (SWCNT): this can be thought of as a single sheet of graphite rolled up to form a seamless cylinder. If a number of sheets are rolled up to form concentric tubes, we obtain multi-walled CNT (MWCNT). The spacing between cylinders in MWCNT is close to that of graphite (about 0.34 nm)[55], (Figure 4).

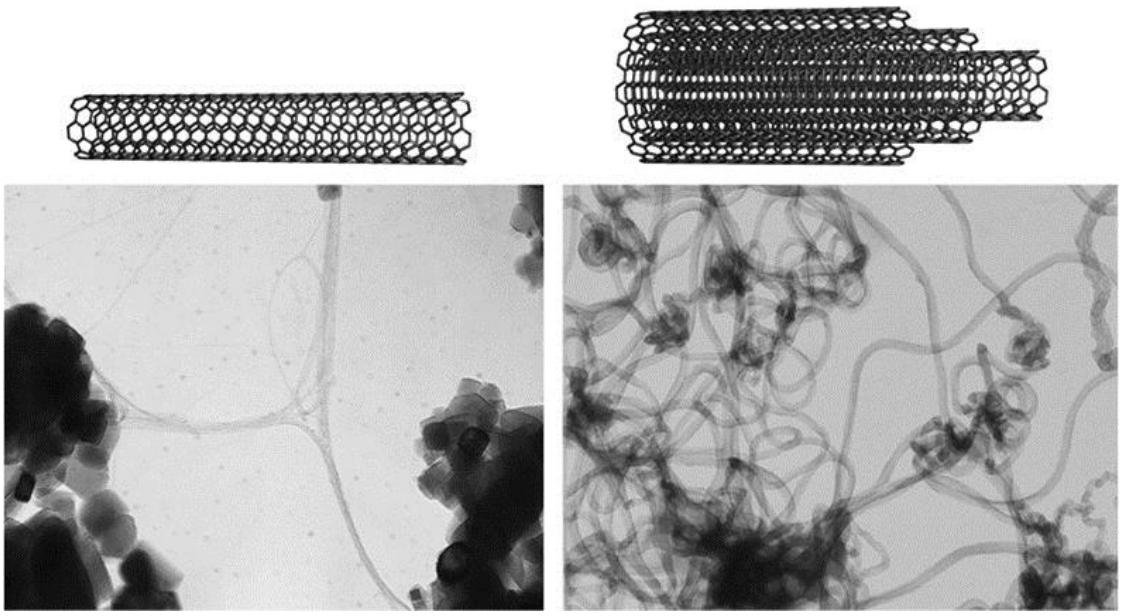

Figure 3. Basic types of CNT, SWCNT (top left) and MWCNT (top right) with typical trasmission electron micrographs below)[55].

The synthesis of CNT is critical in determining the structure, side-products, impurities and, therefore, potential toxic activity of any given sample. Tube widths are dependent on synthesis, but are generally found in the range from 0.7 to 3 nm (SWCNT)[56] and from 10 to 100 nm (MWCNT)[57]. Tube lengths may be anywhere from a few nanometers to tens of microns, but aggregates and bundles can be significantly longer and wider.

There are three major methods of CNT synthesis: arc-discharge, laser ablation and chemical vapor deposition (CVD)[58]. The underlying principle involves producing fragments of carbon that are then reconstituted to form the tube, usually with the aid of a metallic catalyst, at quite high temperatures (500-1200°C). It is possible to produce CNT without metal catalysts, although the

yields are exceedingly low. The most common method of synthesis is CVD. In addition to heat (600°C), there are three key ingredients: carbon source (e.g. methane, methanol, benzene); catalyst support (e.g. zeolite, aluminates or silicates); metal catalyst (this is usually transition metals, commonly Fe, Co, Ni and Mo, and sometimes a mix or alloy, of these)[55]. The unique and diverse properties of CNT, in addition to the wide range of functionalities afforded by chemical modification, allow for many exciting applications, including electronic, field emission device, composite materials; in addition, they have numerous biological and medical applications. The CNT have a unique absorption in the near-infrared region, which could be used for biological sensing[59-62].

Toxicity of CNT is related to the properties of CNT materials, such as their structure (SWCNT or MWCNT), length and aspects ratio, surface area, degree of aggregation, extent of oxidation, bound functional group(s), method of manufacturing (which can leave the catalytic residues and produce impurities), as well as to their concentration and dose[55].

MWCNT can exist as compact tangles that are essentially particles (*tangle-like* MWCNT), or as longer, rigid, straight fibres (*needle-like* MWCNT). Particle effects would be confined to the lungs as fibrosis and cancer whilst fibres, exemplified by asbestos, are known have the same types of pulmonary effect but to also affect pleura. Several decades of fibre toxicology have led to an overarching fibre toxicology concept, based on length, diameter and biopersistence (the "fibre paradigm", Figure 5).

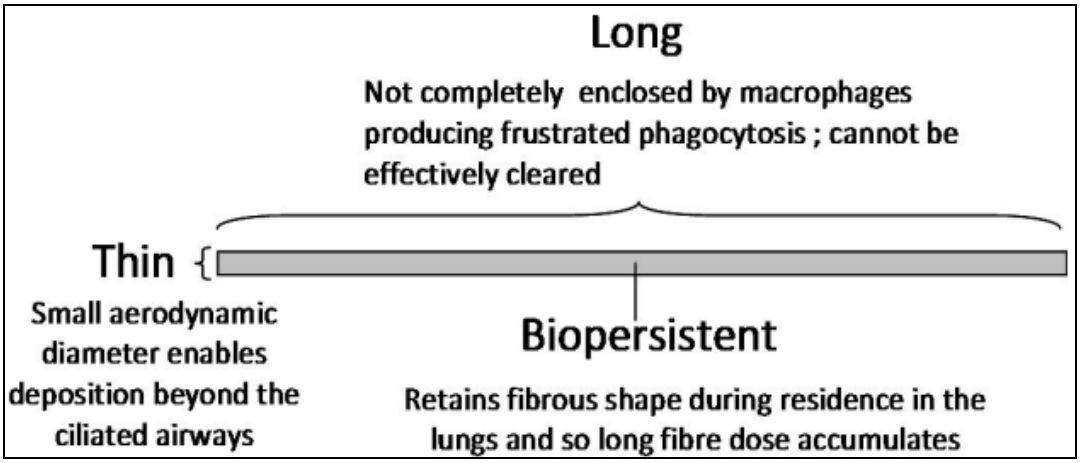

Figure 4. Diagram illustrating a pathogenic fibre according to the pathogenicity paradigm and the role of particles characteristics[63].

The fibre paradigm identifies the geometry of fibres as their most important toxicological characteristic[63]. Diameter is important because of the central role that fibre diameter plays in defining aerodynamic diameter (D_{ae}) and the dependence of pulmonary depositions on D_{ae}[64].

Clearance from sites beyond ciliated airway is dominated by slow, macrophage-mediated clearance[65] and so fibres which deposit there have the potential to contribute most to build-up of high doses. Biopersistence and length interact in determining the clearance of long fibres from the lungs since long fibres might undergo dissolution which could result in complete dissolution, or most likely weakening of the fibre such that it undergoes breakage into shorter fibres, which can be more rapidly cleared than long fibres. On the contrary, if fibres remain long (> 8 μm) they are slowly cleared as they cannot be easily engulfed by macrophages[66] leading to frustrated phagocytosis. Thus, long fibres are more likely to accumulate in the lungs allowing the dose to build up. Conversely, long fibres that are composed of bio-soluble (non biopersistent) structural components can undergo weaking and breakage in the lung[67-68].

A study where the peritoneal mesothelium was exposed to carbon nanotubes revealed that long MWCNT showed similar, or greater, propensity to produce inflammation and fibrosis in the peritoneal cavity, compared to that produced by long asbestos. In contrast, neither short asbestos fibres not short, tangle MWCNT cause any significant inflammation. Frustrated phagocytosis of long fibres as it likely applies to asbestos and carbon nanotubes is illustrated in Figure 6.

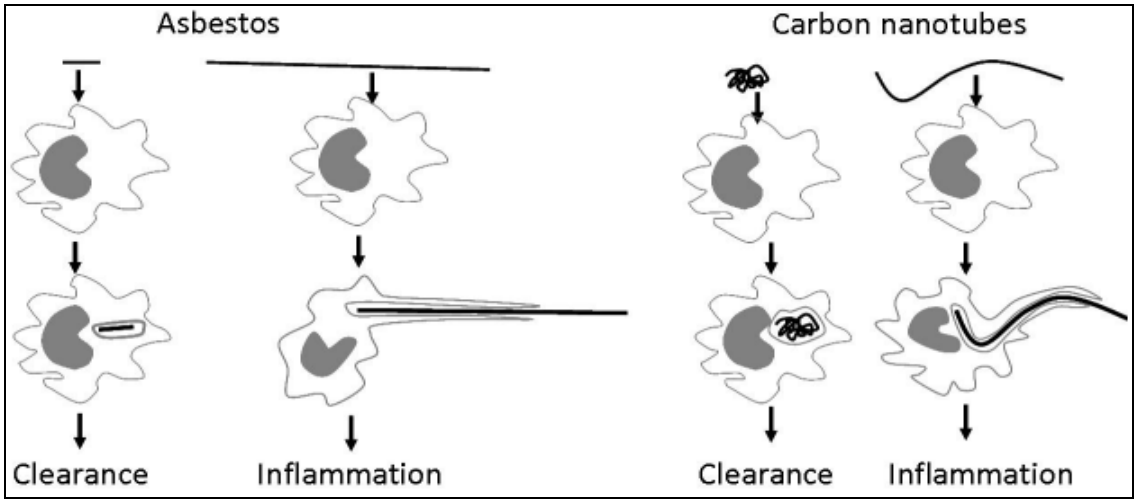

Figure 5. The frustrated phagocytosis paradigm ad it relates to long and short fibres of asbestos (left) and various forms of carbon nanotubes (right). When confronted by short asbestos fibres or tangle, compact carbon nanotubes "particles" the macrophage can enclose them and clear them. However,,the macrophage cannot extend itself sufficiently to enclose long asbestos or long nanoubes, resulting in incomplete or frustrated phagocytosis, which eventually lead to chronic inflammation[63].

Overall, MWCNT with a diameter of 50nm were the most pathogenic, whereas those with a diameter of 145nm were much less pathogenic, and those with a diameter of 15nm (tangled) were

the least pathogenic[69]. One report suggests a link between the diameter of MWCNT and their toxicity to alveolar macrophages, with the thinner MWCNT (9.4 nm vs 70nm) being more toxic[70].

1.4 Amorphous silica nanoparticles

Silica refers to the chemical compound SiO_2 (silicon dioxide) that occurs in two specific and distinct forms: amorphous and crystalline. The word "crystalline" implies that the silicon and oxygen atoms are oriented and related to each other in a fixed pattern as opposed to the random fashion that predominates in the amorphous form of silica. The most common crystalline forms of silica involved in workplace exposures include quartz, tridymite, and cristobalite. Silica may also occur naturally and at varying concentrations in rocks such as sandstone (67% silica) and granite (25 to 40% silica).

Silicates are structures composed of silicon dioxide bound to cations such as magnesium, aluminum, or iron. Examples of silicates include mica, soapstone, talc tremolite, Portland Cement, and others. Occupational exposure to dust of crystalline silica has been shown to induce silicosis, a chronic lung disease characterised by granulomas and several fibrosis in the lungs.[71-74].

Amorphous silicas are divided into naturally occurring amorphous silicas and synthetic forms. The naturally occurring amorphous silicas such as diatomaceous earth usually contain significant amounts of crystalline silica, sometimes up to 60 wt%. Certain industrial process produce silica fume and fused silica as by-products. These materials often contain a number of impurities including crystalline silica and should not be confused with the commercial product known as fumed silica[75]. Synthetic amorphous silicas (SAS) are intentionally manufactured amorphous silicas that do not contain measurable levels of crystalline silica and as such are not associated with the negative health impacts attributed to crystalline silica or the naturally occurring amorphous silicas. The synthetic forms may be classified as: wet process manufactured silica and pyrogenic (thermal or fumed) silica. These two types of SAS can be further modified by surface treatments (Figure 3). SAS are used in many materials such as synthetic resins, plastics, lacquers, vinyl coatings, varnishes, adhesives, paints, printing inks, silicone rubber, fillers in the rubber industry, tyre compounds, insulation materials, liquid systems in coating, as free-flow and anti-caking agents in powder materials, as tooth paste additives, pharmaceuticals, cosmetics, as liquid carriers particularly in the manufacture of agrochemicals and animal feed, and food, resulting in widespread exposure to these materials[76].

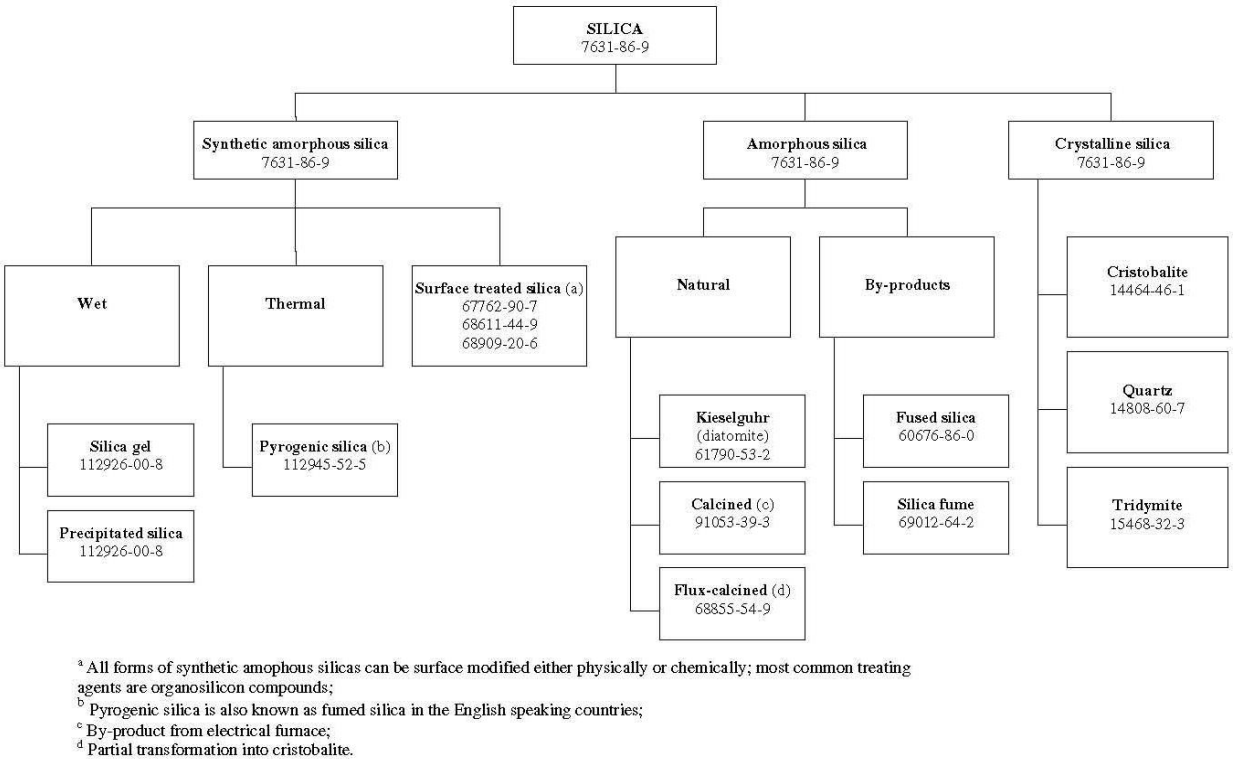

Figure 6. Different polymorphs of silica with CAS No. 7631-86-9numbers[76].

Aggregates of amorphous silica of micrometer size have been used for years in oral and dermatological formulations, other drug formulations, food, and cosmetics; hence, new nanomaterials containing SiO_2 are considered low toxic and moderately biocompatible. However, the fast growing knowledge in the nanoscience fields has confirmed that, at nano-dimension, materials can acquire new feature. This is true also for the amorphous silica: in fact, if nanoparticle aggregates ranging from a few micrometers up to millimeter are rather irritant but non-toxic, on the other hand, SiO_2 nanoparticles (ASNP) show a dose-related toxicity in *in vitro* experiments. In water, SiO_2 surface exhibits silanol groups (Si–O–H). At nanoscale, the high density of silanol groups on SiO_2 NPs form several siloxane framework architectures making SiO_2 NPs extremely reactive and prone to be modified by environmental factors. These architectures are combinations of closed siloxane rings, along with the spatial arrangement, pattern, and degree of hydrogen bonding that terminate the siloxane rings at the silica NP surface; in addition, some scientists have also hypothesized surface-associated radicals inducing ROS species. In recent years, many new synthetic routes to produce stabilized amorphous silica nanoparticles have been developed. A few publications demonstrate that even the synthetic procedure can influence their effects on cells and living systems. The assessment of the structure–activity relationships for amorphous silica is,

therefore, problematic. While crystalline silica is structurally well-defined, amorphous silica lack long-range order, and, due to a flat energy landscape, their structures are strongly dependent on synthetic procedures. Therefore, it is necessary to associate to each synthetic procedure an exhaustive description of the effects produced in living organisms: (i) to explain the mechanism of action of new materials, (ii) to open new ways on novel material application potentialities, (iii) to create a database of material/living-systems interactions.[77-80]. As a consequence, due to such a variety of possible ASNP structures, the toxicological behaviour of amorphous silica is not well characterized.

CHAPTER 2

AIM OF THE THESIS

The overall aim of the thesis project is the elucidation of the potential hazards of several common types of engineered nanomaterials (ENM) evaluating their interactions with relevant cell models. Particular attention is given to the assessment of potential toxic effects on cells of innate immunity and to the identification of structural determinants of toxicity.

The specific aims of this study are:

- the comparison among four preparations of multi-walled carbon nanotubes (MWCNT, suspected to have potential toxic properties analogous to those observed with other fibrous particles, such as asbestos), with different length, morphology, and level of metal contaminants. We have assessed the biological effects of the four MWCNT preparations on macrophages and airway epithelial cells, in order to identify the determinants of toxicity, thus far incompletely elucidated.
- the comparison between two preparations of amorphous silica nanoparticles (ASNP, a material usually considered endowed with modest toxicity), characterized by different structural features. This study assesses the capability of ASNP, of comparable size but produced through different synthetic procedures (colloidal *vs* pyrogenic), to induce macrophage activation in two murine cell lines widely employed in nanotoxicological studies.

CHAPTER 3

MATERIALS AND METHODS

3.1. Materials

The three preparations of MWCNT (NM400, NM401 and NM402) and two preparations of ASNP (NM200 and NM203) were obtained from the Joint Research Centre of Ispra (VA, Italy). These materials are classified as representative test materials (RTM) and include a (random) sample from one industrial production batch. They are within the scope of the EU FP7 project "Managing risks of nanomaterials" (MARINA)". Commercially available MWCNT (MWCNT-SA) were obtained from Sigma-Aldrich (Milan, Italy, cat. No. 659258). Before the experiments, ASNP and MWCNT were heated at 230 °C for 4h to eliminate possible contamination from lipopolysaccharide (LPS).

3.2 Cells

MH-S murine alveolar macrophages were obtained from prof. Dario Ghigo, University of Torino (Italy). RAW264.7 murine peritoneal macrophages were obtained from the Istituto Zooprofilattico Sperimentale della Lombardia ed Emilia-Romagna (Brescia, Italy). Cells were routinely cultured in 10-cm diameter dishes in RPMI1640 medium supplemented with 10% FBS, streptomycin (100 µg/ml) - penicillin (100 U/ml), L-glutamine (2 mM) and (for MH-S cells only) β-mercaptoethanol (0.05 mM) in a humidified atmosphere of 5% CO_2 in air. For viability experiments, macrophages were seeded in 96-well plates, at the density of $30x10^3$ cells. For microscopy analysis and phagocytosis assay, they were seeded in 4-chamber glass culture slides (BD Falcon,MA,USA), at the density of $20x10^4$ and $25x10^4$, respectively. For the other experiments, cells were seeded in 24-well plates, at the density of $20x10^4$.

Calu-3 cells, obtained from a human lung adenocarcinoma and derived from serous cells of proximal bronchial airways, were obtained from the Istituto Zooprofilattico Sperimentale della Lombardia ed Emilia-Romagna (Brescia, Italy). Cells were routinely cultured in 10-cm diameter dishes in EMEM supplemented with 1 mM sodium pyruvate, 10 % FBS and streptomycin (100 µg/ml) and penicillin (100 U/ml) in a humidified atmosphere of 5% CO_2 in air. BEAS-2B, human bronchial epithelial cells, and A549, human alveolar basal epithelial cells, were cultured in Dulbecco's Modified Eagle Medium (DMEM) (Euroclone, Italy), supplemented with Gln (4 mM) and 10% FBS in a humidified atmosphere of 5% CO_2 in air. For the experiments, epithelial cells

were seeded into culture inserts with permeable membrane filters (pore size of 0.4 μm) for Falcon 24-well-multitrays (BD Bioscience, USA), at a density of 75×10^3 cells/well.

3.3 Exposure to nanomaterials

After cooling at room temperature, NM400, NM401, NM402, NM200 and NM203, were dispersed in a stock solution at a concentration of 2.5 mg/mL by prewetting powder in 0.5% ethanol (96% purity) followed by dispersion in 0.05 wt% Bovine Serum Albumin (BSA, A9418, Sigma Aldrich) in water, according to Nanogenotox protocol (EU NANOGENOTOX Joint Action)[81]. MWCNT-SA were dispersed in a stock solution at a concentration of 1 mg/mL in sterile Phosphate Buffered Saline (PBS). After 15 min of bath sonication, working concentrations of all the nanomaterials were obtained by serial dilutions.

For permeability experiments MWCNT dispersions were added to the growth medium at the apical side of the permeable filter on which cell monolayers had grown.

Taking into account the volume/surface ratio of the various culture systems adopted and the use of sub-confluent (for cytotoxicity experiments) or confluent monolayers (for other studies), we have expressed the nominal doses as μg of materials per cm^2 of monolayer.

3.4 Resazurin assay

Resazurin is a non-fluorescent molecule which is converted by intracellular reductases in the fluorescent compound resorufin (λ_{em} = 572 nm). After its production, resorufin accumulates into the medium and can be readily determinated with a fluorometer[82]. For the measurement of the viability of Calu-3 cells monolayers, they were incubated for 2 hours with resazurin, added to both the basolateral and the apical compartments. Because the culture inserts did not allow direct fluorescence reading from the wells, the measurement has been performed on the medium of apical chamber transferred in a clean 96-well dish. Fluorescence was measured at 572 nm with a multimode plate reader Perkin Elmer Enspire (Waltham, Massachusetts, USA).

For macrophages, after the selected incubation periods in the presence of ASNP or MWCNT, medium was replaced with a solution of resazurin (44 μM) in serum-free medium. Fluorescence was read after 30 min. Since nanomaterials can interfere with viability tests, the dye was preliminarily incubated with the four preparations of MWCNT and the two ASNP preparations (at the maximal dose used), and the fluorescence was then measured. No fluorescence signal was detected above the blank. Data were expressed as the % of the value obtained for the untreated control.

3.5 Phagocytosis assay

Fluorescent yellow-green polystyrene latex beads (2 μm, Sigma-Aldrich, Milano, Italy) were opsonized with 50% human serum for 30 min at 37°C before the experiments. After the treatment in presence of MWCNT, macrophages were incubated for 2 h at 37 °C in complete growth medium in the presence of latex beads (20 microspheres/cell). Cell monolayers were then washed vigorously with PBS to remove extracellular beads, counterstained with 2 μM of the vital cytoplasmic dye CellTracker Red CMTPX (Invitrogen, Milano, Italy) and fixed with 2% paraformaldehyde for 10 min. The number of internalized latex particles was determined by counting intracellular fluorescent beads with a fluorescent microscope. For each culture, at least 3–5 fields containing about 100–150 cells were analysed. Percent of phagocytosis was calculated as the number of cells with at least one bead inside/total number of cells counted[83].

3.6 Gene expression analysis

After the selected incubation periods in presence of ASNP or MWCNT, the expression of *Nos2* (in macrophages treated with ASNP and MWCNT) and *Hmox-1* (in macrophages treated with ASNP) was assessed with Real Time PCR. 1μg of total RNA, isolated with GenElute Mammalian Total RNA Miniprep Kit (Sigma-Aldrich) was reverse transcribed. For Real-Time qPCR, cDNA was amplified with Go Taq PCR Master Mix (Promega, Italia, Milan, Italy), using the forward and reverse primers indicated in Table 1 (5pmol each). The expression of the gene of interest under each experimental condition was normalized to that of *Gapdh* and shown relative to its expression level control, untreated cells following the method of Relative Standard Curve Method[84].

Gene	Protein	Forward primer	Reverse primer	T(°C)	Amplicone size (bp)
Nos2	Nos2	5'-GTT CTC AGC CCA ACA ATA CAA GA-3'	5'-GTG GAC GGG TCG ATG TCA C-3'	57°C	127
Hmox-1	HO-1	5'-AGGTACACATCCAAGCCGAGA-3'	5'-CATCACCAGCTTAAAGCC TTCT-3'	57°C	86
Gapdh	Gapdh	5'-TGT TCC TAC CCC CAA TGT GT-3'	5'-GGT CCT CAG TGT AGC CCA AG-3'	57°C	137

Table 1. Primers and temperatures of annealing adopted for RT-PCR experiments

3.7 Western blot

After treatments with ASNP, macrophages were lysed in a buffer containing 20 mMTris–HCl, pH 7.5, 150 mM NaCl, 1 mM EDTA, 1 mM EGTA, 1% Triton, 2.5 mM sodium pyrophosphate, 1 mM

β-glycerophosphate, 1 mM Na_3VO_4, 1 mM NaF, 2 mM imidazole and a cocktail of protease inhibitors (Complete, Mini, EDTA-free, Roche, Milan, Italy). Lysates were sonicated for 15s and centrifuged at 12,000g for 20min at 4°C. After quantification with the Bio-Rad protein assay, aliquots of 40 μg of proteins were mixed with Laemmli buffer 4× (250 mMTris–HCl, pH 6.8, 8% SDS, 40% glycerol, and 0.4M DTT), warmed at 95°C for 10 min and loaded on a 8% gel for SDS-PAGE. After electrophoresis, proteins were transferred to PVDF membranes (Immobilon-P, Millipore, Millipore Corporation, MA, USA). Non-specific binding sites were blocked with an incubation of 1h at room temperature in BSA 5% in TBS-Tween. The blots were then exposed at 4 °C overnight to anti-Nos2 (rabbit policlonal, 1:400, Santa Cruz Biotechnology) or anti-Actin (rabbit polyclonal, 1:30,000, Cell Signaling Technology diluted in the same solution). After washing, the blots were exposed for 1h at room temperature to HRP-conjugated anti-rabbit antibody (Cell Signaling Technology), diluted 1:20.000 in blocking solution. Immunoreactivity was visualized with Immobilon Western Chemiluminescent HRP Substrate (Millipore, Milan, Italy).

3.8 Determination of NO production

After the selected incubation periods in presence of ASNP and MWCNT, Nitrite concentration in the culture media of macrophages treated with ASNP and MWCNT, as an indicator of NO production, was determined through a fluorometric approach, as previously described[85]. The method is based on the production of the fluorescent molecule 1H-naphthotriazole from 2,3-diaminonaphthalene (DAN) in acid environment. For nitrite determination, 100 μl of medium were put in wells of a black 96-well plate with a clear bottom (Corning, Cambridge, MA, USA). DAN (20 μl of a solution of 0.025 mg/ml in 0.31 M HCl) was then added and, after 10 min at room temperature, the reaction was stopped with 20 μl of 0.7 N NaOH. Standards were performed in the same medium from a solution of 1 mM sodium nitrite. Fluorescence was determined with an EnSpire plate reader (Perkin Elmer). Nitrite production was expressed in nmoles per ml of extracellular medium (μM).

3.9 Trans-epithelial electrical resistance (TEER)

Measurements of the TEER of Calu-3 cells monolayers treated with MWCNT were made with an epithelial voltmeter (EVOM, World Precision Instruments Inc., Sarasota, FL, USA) that produces an AC current. Before the permeability experiments, cells were allowed to grow, usually for 10–14 days, until a value of TEER higher than 1,000 Ω cm^2 was reached, indicating the formation of a

tight epithelial layer. TEER changes were expressed as the percentage of the initial value adjusted for control cell layers according to the equation[86]:

$$TEER\% = \frac{final\,TEER_{treated}}{final\,TEER_{control}} \times \frac{initial\,TEER_{control}}{initial\,TEER_{treated}} \times 100$$

3.10 Caspase activity (cell extracts)

Calu-3 cells monolayers treated with MWCNT-SA were mechanically detached from the filter and centrifuged at 300g. for 5 min Pellets were resuspended in 500 µl of assay buffer (50 mM Hepes, 0.1% CHAPS, 10 mM EDTA, 5% glycerol, and 10 mM DTT) and vigorously vortexed. After centrifugation at 12000g for 10 min at 4°C, the protein content in the supernatant was determined with the Bio-Rad protein assay. Aliquots of 10 µg protein were distributed in each well of a 96-well plate, along with the caspase substrate Ac-DEVD-pNA (200 µM, Alexis Biochemicals, San Diego, CA). The absorbance at 405 nM was read with EnSpire plate reader after 16h at 37°C. Caspase activity under each condition was expressed as the % of the value obtained for the untreated control cells after subtraction of the blank value.

3.11 Confocal microscopy

3.11.1 Confocal laser scanning microscopy on Calu-3 cells monolayers

Confocal analysis was carried out with a LSM 510 Meta scan head integrated with an inverted microscope (Carl Zeiss, Jena, Germany). Calu-3 cells monolayers treated with MWCNT-SA were observed through a 40x (1.3 NA) or a 63x (1.4 NA) oil objectives. Image acquisition was carried out in multitrack mode, i.e. through consecutive and independent optical pathways. Vertical sections were obtained with the function Display – Cut (Expert Mode) of the LSM 510 confocal microscope (Carl Zeiss, Jena, Germany) software (Microscopy Systems, Hartford, CT). Reconstructions were performed from z-stacks of digital images (minimum 32 confocal sections, z-axis acquisition interval of 0.39 µm), processed with the Axiovision module inside 4D release 4.5, applying the shadow or the transparency algorithm.

3.11.2 Cellular internalization of ASNP

After 24h of treatment with ASNP, three washings with PBS were carried out. After fixation with 4% paraformaldehyde (PFA) for 10 min at room temperature, cells were stained with Hoechst 33342 for nuclei and rhodamine phalloidin (Invitrogen, Oregon, USA) for F-actin. The slides were incubated at room temperature for 1h in the dark, rinsed with PBS and mounted in transparent mounting medium (VECTASHIELD, Vector Laboratories Inc., CA, USA) prior to confocal microscopy analysis by a ZEISS 510 Meta confocal microscope equipped with a Zeiss LSM 5 software (Carl Zeiss, Germany). ASNP were imaged in reflection mode at λ_{exc} = 561 nm. Qualitative confocal imaging was carried out by acquiring a series of z-stack images. Surface rendering of z-stack images was carried out by the open-source software BioImageXD.

3.12 Cytotoxicity analysis: live cell monolayers

3.12.1 Calcein/PI assay

After exposure to MWCNT-SA, cell culture medium was replaced with fresh, complete medium containing 2.5μM calcein-acetoxymethylester (Calcein-AM, Invitrogen, Paisley, UK) and 4 μg/ml propidium iodide (PI). Calcein-AM is a non-fluorescent molecule that passively enters live cells, where it is converted into a green fluorescent dye (calcein) by intracellular esterases. Calcein is retained by live cells until plasma membrane is intact. Propidium iodide (PI) is a red fluorescent dye that stains cells with compromised cell membrane binding to nucleic acids. Cells were incubated for 15 min at 37°C and then washed with fresh medium. The permeable filters were then detached from the culture inserts and live specimens were imaged by an inverted LSM 510 Meta confocal microscope (Carl Zeiss, Jena, Germany) while incubated with fresh medium in a Kit Cell Observer (Carl Zeiss, Jena, Germany), which allows a fine control of temperature, CO_2 percentage and humidity[87]. Samples were observed through 40x (1.3 NA) or a 63x (1.4 NA) oil objectives. Calcein, excited with a 488 nm laser with the emission recorded through a 505–530 nm band pass barrier filter, was rendered with a green pseudo-colour. PI, excited with a 543 nm laser with the emission recorded through a 560 long pass barrier filter, was rendered in red. MWCNT agglomerates were imaged in reflection mode at λ_{exc} = 633 nm and are shown in grey pseudo-colour. Images were then processed as previously described. For quantification of PI-positive cells, six random chosen fields (approximately 0.1 mm^2) were analysed through a series of vertical sections. Quantitative analysis for live/dead accounts was carried out on large areas (approximately

1 cm^2each) of the prepared samples by high throughput (HTP) technique based on automated epifluorescence microscopy (Nikon TE2000, Japan). HTP analysis of the data was carried out by bioinformatics algorithm based on cell live/dead counting. To provide statistical sample populations, two membranes where analysed for Calu-3 cells: Calu-3 exposed to MWCNT-SA for 8d and Calu-3 only as negative control. PI or Calcein staining were recorded based on their respective emission wavelengths. On average 400 cells were counted for each membrane. The percentage (%) of live cells was then calculated from the counting readings as described in equation:

$$\%\, live\, cells = \frac{Live\, cells\, (calcein)}{Total\, number\, of\ cells\, (cell\, count)} \times 100$$

3.12.2 Caspase activity in situ

After exposure to MWCNT-SA, the cell culture medium at the apical side of the cell monolayers was replaced for 1h by fresh, complete medium supplemented with a sulforhodamine-labelled inhibitor of active caspases (CaspaTag™ Pan-Caspase in Situ Assay kit, Chemicon International, CA, USA). The inhibitor covalently binds to a reactive cysteine residue. Upon washing, the bound reagent is retained while the unbound reagent diffuses out of the cell, so that only cells with high caspase activity remain labelled. Negative (untreated) and positive (doxorubicin, 1 µM, 24h) controls were included in the experimental design. The permeable filters were then detached from the culture inserts and analysed by confocal microscopy as previously described for the calcein/PI assay. The sulforhodamine label was excited with a 543 nm laser and its emission recorded through a 560 long pass barrier filter.

3.13 Immunofluorescence staining: fixed cell monolayers

Cell monolayers, after treatments with MWCNT-SA were rinsed in PBS and fixed with 3.7% paraformaldehyde (PFA) at room temperature for 15 min. Following staining procedures, specimens were mounted on glass slides with fluorescence mounting medium (Dako Italia SpA, Milan, cat. N° S3023) and imaged by confocal microscopy (excitation at 488 nm; emission recorded through a 505–530 nm band pass barrier filter).

3.13.1 Proliferative activity

Actively proliferating cells were detected from the positivity to the nuclear antigen Ki-67, a protein expressed by cells in G_1, S, G_2, or M phases, but not by quiescent cells in G_0[88]. For this assay, cells

were permeabilized with methanol at -10 °C (5 min), incubated in blocking solution (10% goat serum) at room temperature, and incubated with primary anti-Ki-67 mouse monoclonal antibody (Santa Cruz Biotechnology, (USA), 1:000 + 1.5% goat serum) for 60 min. Filters were then washed in PBS and incubated with 1:400 Alexa 488 anti-mouse IgG (Invitrogen, Paisley, UK) for 45 min at 37 °C. After washing in Tween 0.1%, detached filters were mounted on glass slides with mounting medium prior to confocal imaging. Quantitative analysis of cell proliferation was carried out by HTP technique based on automated epifluorescence microscopy (Nikon, TE2000, Japan).

At monolayer level, HTP analysis of cell proliferation was carried out by bioinformatics algorithm based on nuclear counting and positive nuclear Ki-67-green fluorescent staining average intensity per cell. Two stained samples containing Calu-3 cell only (negative control) and Calu-3 exposed to MWCNT-SA for 8d were analysed based on the intensity level of localised nuclear Ki-67-green fluorescent staining. The percentage (%) of proliferating cells was calculated from the following equation:

$$\%\ proliferatng\ cells = \frac{Ki67 - positive\ fluorescence}{Total\ cell\ count} \times 100$$

The total cell count was based on the fluorescence intensity of nuclear staining (4',6-diamidino-2-phenylindole (DAPI) staining, emission wavelength = 461 nm). On average, 400 cells were counted for each well.

3.13.2 Organization of F-actin filaments

After fixation, MWCNT-SA-exposed cells were permeabilized with 0.1% Triton X-100 (10 min), incubated for 20 min at 37°Cwith Alexa Fluor-Phalloidin 488 (10 U/ml, Invitrogen, UK). After washing with PBS, detached filters were mounted on glass slides prior to confocal imaging.

3.13.3 NF-κB

After the treatment, Calu-3 monolayers were rinsed twice in PBS, fixed and permeabilized with methanol at -20 °C for 5 min. After fixation, cells were washed twice in PBS and incubated in blocking solution (3% BSA in PBS) at 37°C for 30 min. After blocking, cells were incubated with primary anti-NF-κb p65 rabbit polyclonal antibody (Abcam16502, 1:400 in PBS 1.5% BSA) overnight at 4°C. Filters were then washed twice in PBS and incubated with 1:400 Alexa fluor 488, goat anti-rabbit IgG (Invitrogen) for 45 min at 37°C. Cell nuclei were stained with DAPI (4',6-Diamidino-2-Phenylindole, Dihydrochloride) for 10 min. Detached filters were mounted (Dako, fluorescent mounting medium) and monolayers visualized in confocal microscopy.

3.14 He-Ion Microscopy (HIM)

The helium ion microscope is a unique imaging instrument. Based on an atomic level imaging system using the principle of field ion microscopy, the helium ion source has been shown to be incredibly stable and reliable, itself a remarkable engineering feat. The advantages of the contrast mechanisms offered by this instrument for imaging nanomaterials are clearly apparent due to the high resolution and surface sensitivity afforded in the images[89].

After 24h of treatments with ASNP, cells were fixed at room temperature in 2.5% glutaraldehyde in 0.1 M Sørensen's phosphate buffer (0.133 M, pH 7.3, 0.133 M Na_2HPO_4 and 0.133 M KH_2PO_4, pH 7.3) and rinsed with the same buffer. Samples were dehydrated in increasing concentrations of EtOH (from 70% up to 100%). The final wash was carried out in absolute EtOH for 20 min. The samples were then air dried and imaged by a Zeiss Orion Plus He-ion microscope (Carl Zeiss, Oberkochen, Germany) using an accelerating voltage of 30 kV. Samples were transferred into the chamber, which had undergone plasma cleaning overnight prior to loading samples, using a load lock. The working distance was 8 mm and a 10 μm beam limiting aperture was used. The probe current was between 0.5 and 1.5 pA. Images were acquired by collecting the secondary electrons emitted by the interaction between the He-ion beam and the specimen with an Everhart-Thornley detector (part of the He-ion microscope system). The image signal was acquired in a 32- or 64-line integration to each contributing line of the image.

3.15 Cytokine secretion

After the selected incubation periods in presence of ASNP, TNF- α, IL-6, IL-1β production in the culture media of the cells was determined with the ELISA RayBio® kit (Ray Biotech, Norcross, GA, USA). 100 μl of medium were transferred in 96-well plates functionalized with an anti-cytokine antibody and incubated overnight at 4°C. Then, 100 μl of biotinylated antibody were added in each well and, after 1h of incubation at RT, 100 μl of streptavidin solution were added. After 45 min samples were incubated with 100 μl of the TMB One Step Reagent, contained in the kit solution; after 30 min, reaction was stopped and absorbance was immediately read at 450 nm with a plate reader. Standards were performed in the assay buffer from a solution of 50 ng/ml of the recombinant cytokine. The cytokine amount was expressed as pg/ml.

3.16 Intracellular reactive oxygen species measurement

After the selected incubation periods in presence of ASNP, the production of ROS was measured using 5-(and-6)-chloromethyl-2',7' dichlorodihydrofluorescein diacetate, acetyl ester (CM-H_2DCF-DA, Cat. No. C6827, Molecular Probes, Invitrogen, Grand Island, NY, USA). After treatment, cells were incubated with the probe (5 µM) for 2h at 37°C. Cells were then washed twice with PBS and the fluorescence was determined (485 nm λ_{ex} and 520 nm λ_{em}) with a multiplate reader. Hydrogen peroxide (6mM, one hour before adding the probe) was used as a positive control. Cell fluorescence was visualized using a fluorescence microscope (Nikon DS5MC digital camera (Nikon Instruments SpA, Firenze, Italy)., Tokyo, Japan). The intensity of fluorescence was expressed as Arbitrary Units (AU) per µg of protein.

3.17 Chemicals and Reagents

FBS and culture media were purchased from Euro-Clone SpA, Pero, Milan, Italy. Pluronic F127 and CM-H_2DCF-DA (Molecular Probes) were obtained from Invitrogen SpA (San Giuliano Milanese, Milan, Italy). The natural surfactant Curosurf®, consisting of pig lung surfactant, was kindly supplied by Chiesi Farmaceutici SpA (Parma, Italy). The Curosurf® used in this work contained phosphatidylcholine (73% of the total phosphorus) and 1.7 mg/ml of surfactant proteins (SPB and SP-C). Sigma-Aldrich (Milan, Italy) was the source of all other chemicals, whenever not specified otherwise.

3.18 Statistics

One-way ANOVA with Tukey test was used to compare TEER values and monolayer viability. Statistic evaluation of the other effects has been performed with two-tailed t test for unpaired data. Analyses were performed with Graph Pad Prism software version 4.00 (Graph Pad Software Inc., San Diego, CA). Non-linear regression analyses of viability results were performed with the same software.

CHAPTER 4

CARBON NANOTUBES

RESULTS

4.1. Physico-chemical properties of MWCNT

The four preparations of MWCNT were produced through Chemical Vapor Deposition (see introduction 1.3). According to the morphology of the tubes, we can divide the preparations of MWCNT into two groups:

- Group 1: *tangle-like* MWCNT (NM400 and NM402)
- Group 2: *needle-like* MWCNT (NM401 and MWCNT-SA)

4.1.1 NM400, NM401 and NM402

A detailed physico-chemical characterization of NM400, NM401 and NM402 was provided in the JRC Reports[90]. Transmission electron microscopy (TEM) showed that all the three preparations of MWCNT have a great variation in the types and content of impurities. All MWCNT appear to contain a fraction of micrometric size particles. Inorganic catalyst particles are abundant in the sidewalls of NM401 and appear to occur mainly at the tube ends in NM402 (Figure 7). NM401 is classified as large-diameter MWCNT (ca. 70 to 80 nm average diameter), whereas NM400 and NM402 are low-diameter MWCNT (ca. 10 to 17 nm average diameter). The average lengths vary from 846 nm (NM400) to 4.05 μm (NM401): ordered by length, NM400 < NM402 < NM401.

The composition of the MWCNT was analyzed using semi-quantitative energy dispersive X-ray spectroscopy (EDS) and was summarized in Table 2. The major impurities in NM400 and NM402 were Al and Fe. NM401 was found to contain minor impurities dominated by Cu (0.2 wt %) and Zn (0.2 wt %). Similar Cu and Zn contents were observed in NM400, whereas only traces of Cu were found in NM402.

Material	C (wt %)	Al*	Si*	Fe*	Co*	Cu*	Zn*	O calculated[#]
NM400	89.81	46100	400	7600	2500	2000	1900	4.15
NM401	99.19		500			2300	2200	0.6
NM402	92.97	21100	500	29800		400		1.93

Table 2. Elemental concentrations by EDS measurements on NM400, NM401 and NM402.
*****ppm by weight, # calculated by difference

Identification of the potential presence of organic contaminants was assessed by sample mass-loss during heating using thermogravimetric analysis. NM400 showed a strong, wide exothermic peak between 500 and 600 °C corresponding to the temperature range with high weight loss in TGA. The first derivative showed more than one decomposition temperature for the two large samples, indicating more than one type of carbon material. The small sample contained only one type of carbon nanotube.

The curves for the decomposition of different NM401 masses appeared highly repeatable and the decomposition temperature was approximately the same for all runs. However, considering also the residual, there was a large amount of catalyst in the samples, based on which the material appears to be non-homogenous.

The analyses of NM402 also indicate non-homogenous material. The results of TGA are summarized in Table 3.

MWCNT samples	Weight catalyst (%)	Main decomposition temperature (°C)
NM400	16.2±2.9	563±8
NM401	18.1±6.7	729±2
NM402	10.6±0.4	555±9

Table 3. TGA analysis of NM400, NM401 and NM402

XRD (X-Ray Diffraction) analyses were performed on NM400 and NM402. For NM400, impurities were identified as Al_2O_3, or a closely related structure (or phase). For NM402, the crystalline material was hematite (Fe_2O_3).

The 24hour dissolution ratio of the three preparations of MWCNT was measured in three different media: 0.05% batch dispersion BSA in water, Gambles solution (represents the interstitial fluid deep within the lung, composed by several salts, among which sodium chloride and sodium hydrogen carbonate are the most abundant) and Caco-2 medium (Eagle's Minimum Essential Medium). The three media give only minor background concentrations of Si, Al, Fe, Co, and Ni, which were the key target elements for assessing the 24 hour NM dissolution ratios.

The media were preliminarily assayed without any MWCNT, giving the media background. Then, known amounts of the MWCNT preparations were added for 24 hours to the three media, the background subtracted and the resulting concentrations were the 24h solubility of the impurities. In this study, Al, Co, Fe and Ni were used as indicators for the catalyst dissolution. In the three incubation media, Al and/or Fe are the major impurities in the three preparations of MWCNT.

The measured concentrations of Al and Fe reached percent levels in NM400 (1.0 wt % Al; 0.2 wt % Fe) and inNM402 (1.3 wt % Al; 1.6 wt % Fe). The concentrations of the four selected elements were too low in NM401 ($\leq$ 0.06 wt %) for reliable assessment. Moreover, for NM401 and NM402, no dissolution was detected in BSA water and Caco2 cell medium.

Finally, the specific surface area (SSA) of NM400, NM401 and NM402 are, respectively, 254, 140.46 and 226.4 m^2/g.

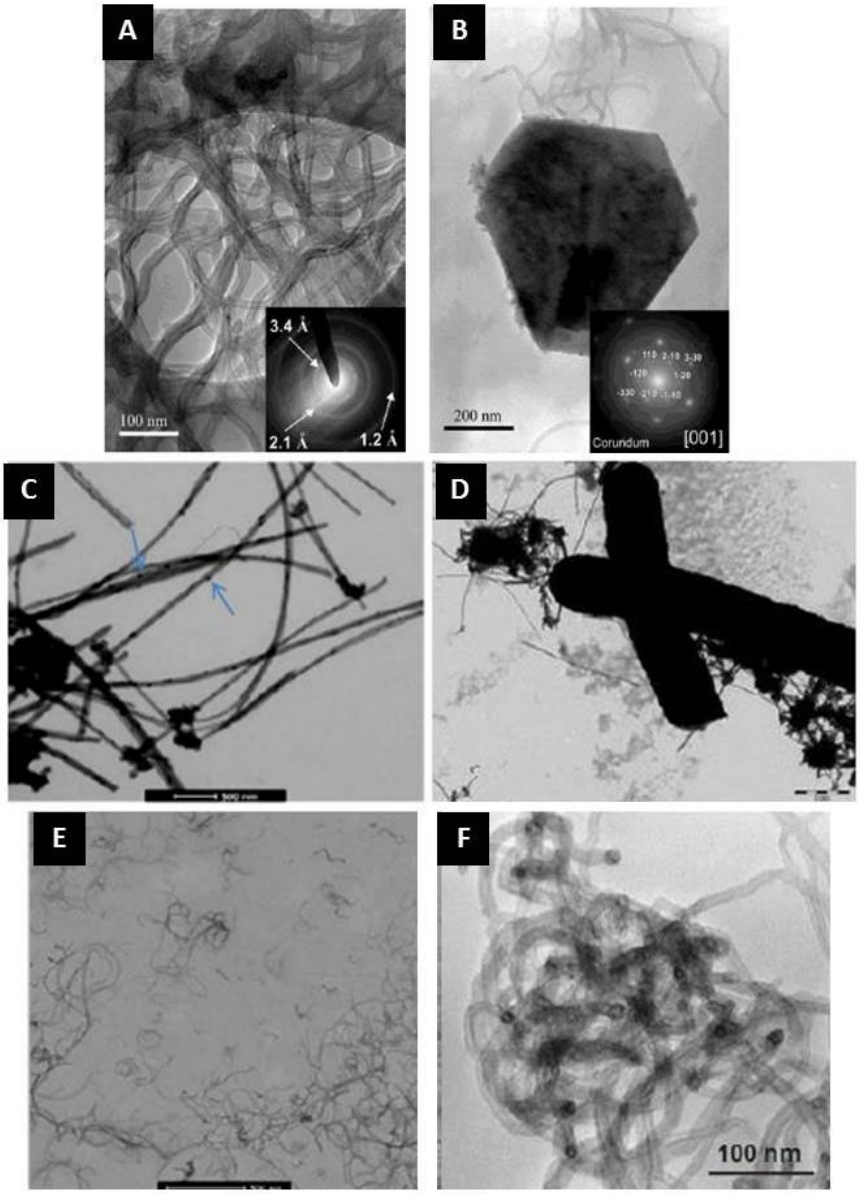

Figure 7. Representative TEM micrograph of NM400, NM401 and NM402.: (A) NM-400, Typical selected area electron diffraction (SAED) pattern is shown in insert (scale bar 100 nm). (B) Example of euhedral foreign particles - catalyst support corundum viewed down [001]. SAED pattern is shown in insert (scale bar 200 nm). (C) NM-401, dark spots, of which two are indicated with blue arrows in the MWCNT sidewall are catalyst impurities (scale bar 500 nm). (D) Example of "megatubes" and μm-size dense aggregates and agglomerates in the NM (Scale bar 2 μm). (E) NM-402, highly dispersed MWCNT in NM-402. (F) Image showing the structure of dense "particle" areas, which consist of highly entangled MWCNT (scale bar 100 nm)[90].

4.1.2 MWCNT-SA

Commercial Multi-Walled Carbon Nanotubes (MWCNT-SA), has an average diameter of 110-170 nm and an average length of 5-9 μm. As by manufacturer analysis, the percentage of MWCNT content was at least 90% with a residual amorphous carbon content present in the sample. The iron concentration declared by the manufacturer was less than 0.1%. High-resolution transmission electron microscopy (HR-TEM) images of MWCNT-SA showed a clean material composed mainly of individual tubes with lengths in order of several microns and diameters ranging from 100 nm to 200 nm (Figure 8A-C), consistently with the dimensions declared by the manufacturer. HR-TEM images did not show the presence of any iron impurities, which should be visible by TEM as black particles because of the high diffraction contrast of this metal. Dark areas were observable on the MWCNT-SA surface and they were associated to synthetic defects onto the graphitic structure of the tubes. HR-TEM results were confirmed by TGA. TGA was performed on MWCNT-SA in air. A residual ash content of 0% (corresponding to a weight loss equal to 100%) was recorded at 900 °C, demonstrating that no detectable traces of the metal catalyst used during MWCNT-SA synthesis were present in the sample. Additionally, the absence of weight loss below 500 °C, which is attributed to the decomposition of organic groups in the carbon nanotubes material, confirmed that no organic chemical contaminants were present in the MWCNT-SA sample. MWCNT, dispersed in the same culture medium used for cellular tests, exhibited a negative ζ potential (-12.01 ± 2.57 mV) at neutral pH. Similar to what is observed with aqueous colloidal particles and what is reported in previous studies on carbon nanotubes, our results were indicative of a non-stable MWCNT dispersion in culture medium (dispersion with ζ potential above +30 mV or below -30 mV correspond to stable solutions). Therefore, MWCNT incubated with the cell cultures were likely to be in the form of aggregates when suspended in culture medium.

Cells monolayers tested in this study were therefore exposed to MWCNT aggregates, which ranged from less than 20 μm of diameter to more than 80 μm. Such aggregates were persistent for several days. Finally, SSA of the MWCNT-SA sample was 22.6 ± 0.38 $m^2 \cdot g^{-1}$. This physico-chemical characterization is largely taken from Rotoli et al [91].

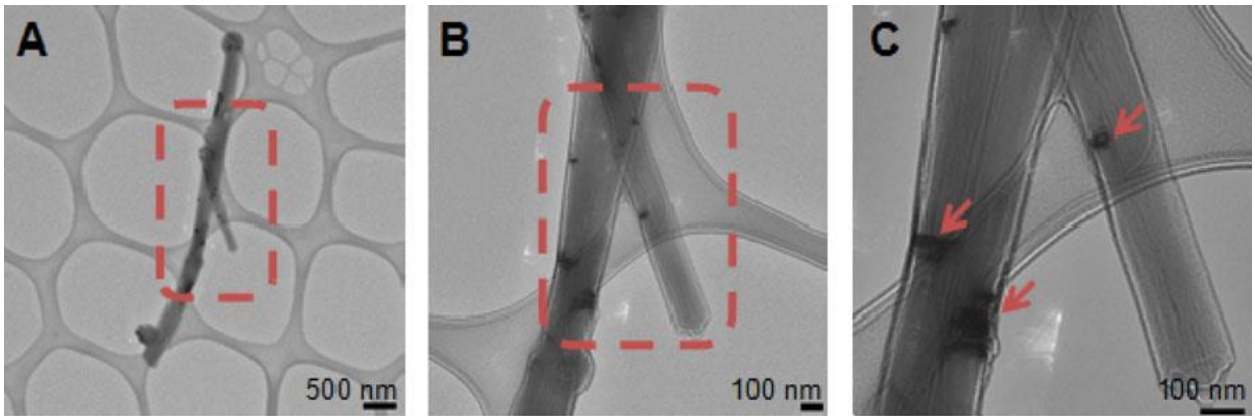

Figure 8. HR-TEM images of MWCNT-SA. (A-C). HR-TEM images of MWCNT on 200-mesh Cu holey carbon grids demonstrating the absence of metal impurities in the specimen. Images B and C are enlargements of the field showed in image A: red boxes highlight the areas analyzed in detail. Examples of defects in the graphitic structure of the tubes, visible as darker areas on the MWCNT surface, are indicated by arrows[91].

4.2 Effects on macrophage viability of MWCNT

The effects on macrophage viability of four preparations of MWCNT (range of doses from 0 to 80 µg/cm^2; exposure time 72h), were assessed with resazurin assay (Figure 9). In both the macrophage cell lines, NM400 and NM402 showed a modest 40% viability decrease at the maximal dose of 80 µg/cm^2. A clear cut dose-dependent toxicity was evident for NM401 and MWCNT-SA, with a marked decrease in viability detected in either cell line at doses up to 10 µg/cm^2. The viability of the two macrophage lines was completely suppressed by MWCNT-SA at the highest doses.

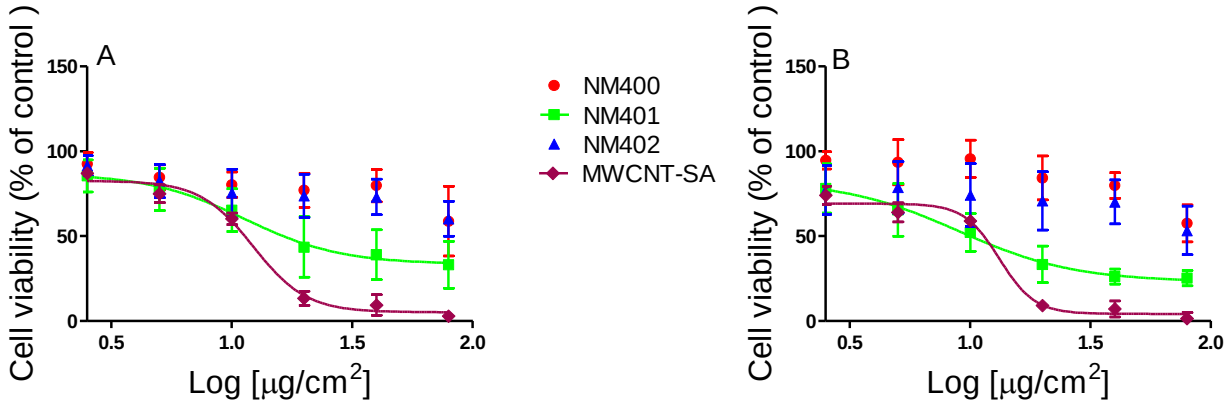

Figure 9. Viability of MH-S and RAW264.7 cells after exposure to MWCNT. Cells, grown for 24h in complete growth medium, were treated for 72h with the indicated preparations of MWCNT (range of doses from 0 to 80 µg/cm^2). At the end of the incubation, cell viability was assessed with resazurin assay. Panel A. MH-S; Panel B. RAW264.7 cells. Data are means +/- SD of 10 independent determinations in two separate experiments.

4.3 Effects of MWCNT on the phagocytic activity

The effects of the four preparations of MWCNT on phagocytic activity, an indicator of functional competence in RAW264.7 cells, is showed in Figure 10. For the experiment, RAW264.7 cells were treated for 24h with MWCNT at the dose of 10 μg/cm^2 (non-cytotoxic dose). The results obtained showed that NM400 and NM402 did not affect phagocytosis, whereas NM401 and MWCNT-SA produced a decrease in phagocytic activity by almost 80% .

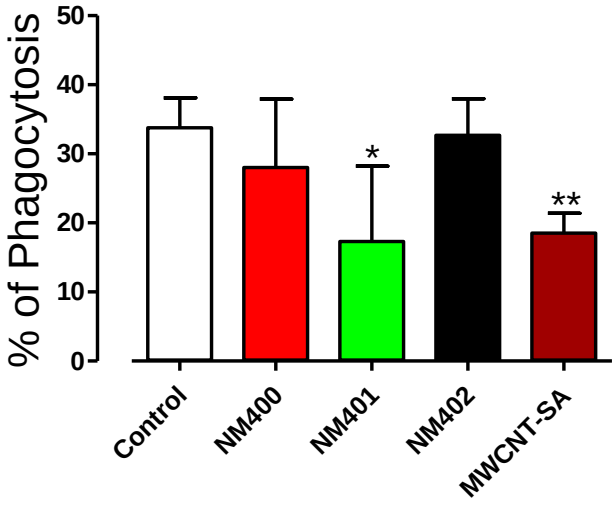

Figure 10. Phagocytic activity of RAW264.7 cells after exposure to MWCNT. Cells, grown for 24h in complete growth medium, were treated for 24h with the indicated preparations of MWCNT at the dose of 10μg/cm^2. At the end of the incubation, phagocytic activity was assessed (see Methods). Data are means +/- SD of 5 independent fields (about 150 cells/field) . *p<0.05, **p<0.01 vs untreated, control cells.

4.4 Effects of MWCNT on M1-macrophage activation

Figure 11A reports *Nos2* mRNA expression after 48h of treatment of MH-S macrophages with non-cytotoxic doses (5 or 10 μg/cm^2) of MWCNT preparations. *Nos2* was significantly induced with NM400 and NM402 (at 10 μg/cm²). This effect corresponded to a clear cut increase in NO production after 72h of treatment (Figure 11C). NM400, at 5 μg/cm^2, determined an increase in nitric oxide production. In RAW264.7 cells *Nos2* messenger was significantly induced with NM400 (at 10 μg/cm^2, Figure 11B). This effect was associated with increased nitrite production (Figure 11D). A significant increase of nitrites was registered also with NM402 at 10 μg/cm^2 . On the contrary, NM401 and MWCNT-SA, did not seem to promote MH-S or RAW264.7 activation either at 5 μg/cm^2 or at 10 μg/cm^2.

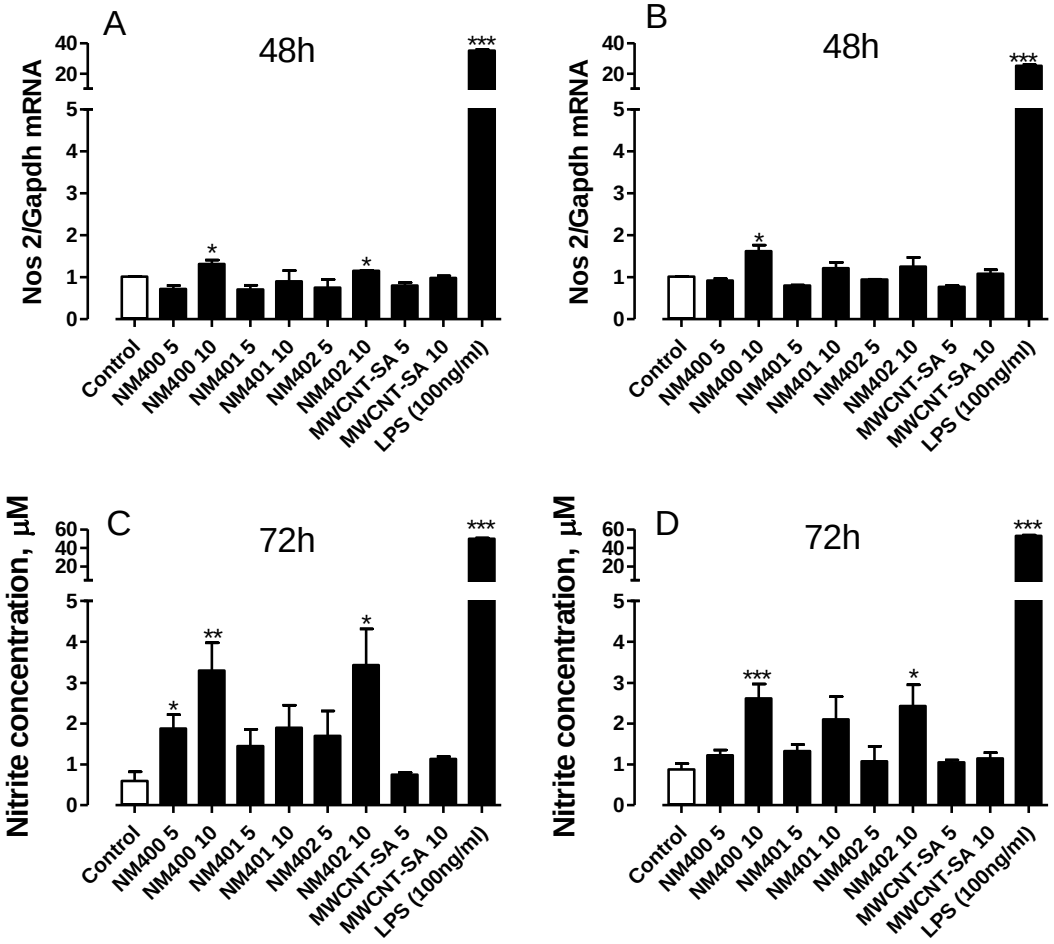

Figure 11. Effects of MWCNT preparations on *Nos2* expression and on nitrites productions in MH-S and RAW264.7 cells. Cells, grown for 24h in complete growth medium, were treated with MWCNT preparations at the doses of 5 and 10 µg/cm^2, or with LPS (100 ng/ml), used as a positive control. After 48h, mRNA was extracted and the expression of *Nos2* evaluated with qRT-PCR, panels A-B. After 72h, nitrite concentration was determined in the culture medium of the cells, panels C-D. For A and B, data are means ± S.D. of 2 independent determinations, each performed twice. For C and F, data are means of five independent determinations ± S.D. *p<0.05, **p<0.01 and ***p<0.001 *vs.* untreated, control cells.

4.5 Analyses in live cell monolayers

TEER measurement were carried out on Calu-3 cell monolayers to identify the responses of these cell cultures following exposure to NM400, NM401, NM402 and MWCNT-SA (80 µg/cm^2). After 8 days of exposure, TEER measurements showed that a significant decrease in TEER was detectable with all the four preparations of MWCNT (Figure 12 A), with the highest effects for NM401 and MWCNT-SA. Calu-3 cell monolayer integrity was biochemically assessed by resazurin assay. After exposure to MWCNT preparations, no significant alteration of the monolayer was detectable by this assay with all the materials tested (Figure12B). Consistently, no increase in caspase activity was detected in cell lysates of MWCNT-SA-treated monolayers (Figure 12C).

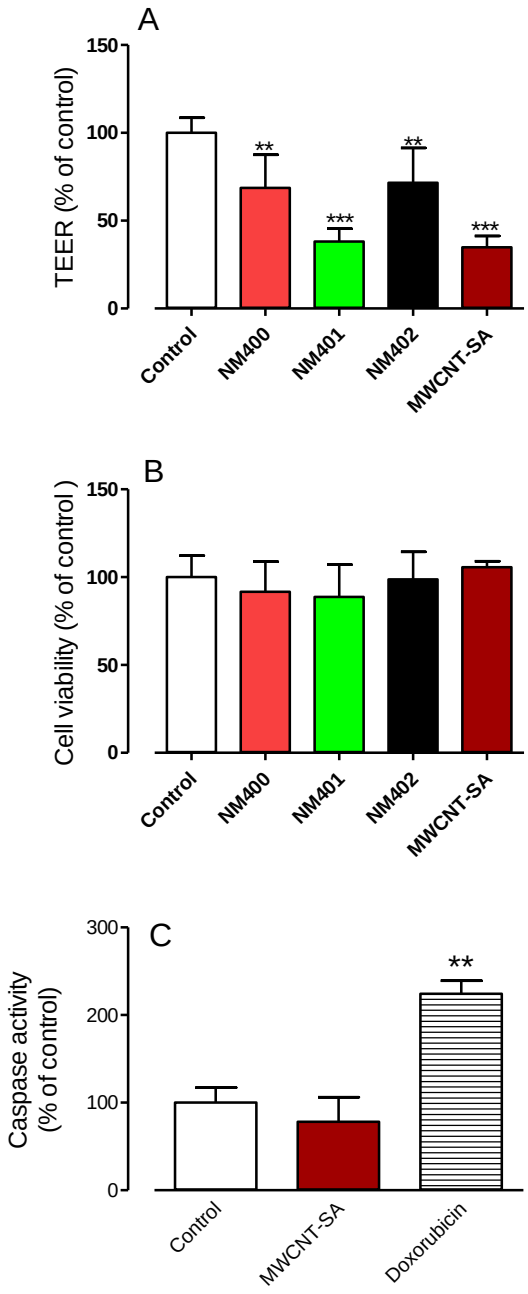

Figure 12. Determination of TEER, cell viability and caspase activity in MWCNT-treated Calu-3 cell monolayers. Cells were incubated with the indicated materials at the dose of 80 μg/cm^2. After 8 days, (A) TEER, (B) cell viability (assessed with the resazurin assay) and (C) caspase activity(assessed in cell lysates), were determinated. For (A) and (B), four MWCNT preparations (NM400, NM401, NM402 and MWCNT-SA) were used. For (C), only MWCNT-SA were used, while doxorubicin (1μM, 1d) was the positive control. Data are means ± SD. **p<0.01, ***p<0.001, versus control, untreated cultures.

Automated epifluorescence microscopy analysis of cell monolayers stained with calcein/propidium iodide confirmed the resazurin measurements, showing no significant changes in cell viability when Calu-3 cell monolayers were exposed to MWCNT-SA (data not shown). The relationship between MWCNT aggregation and TEER decrease was investigated in the experiment recounted in Figure

13. In this experiment, natural and synthetic surfactants were used to delay MWCNT-SA aggregation (Figure 13A-C). The decrease in TEER, already detectable after 3 days of exposure to aggregated MWCNT-SA (Figure 13D), was no longer observable after exposure to MWCNT-SA dispersed in the presence of the natural surfactant Curosurf® (0.8 mg/ml). Interestingly, no significant TEER changes were detected when the natural surfactant was used alone. The decrease in TEER induced by MWCNT-SA was instead comparable in the absence or in the presence of the synthetic surfactant Pluronic (1 mg/ml), which, however, produced a significant TEER decrease even when added alone. Viability measurements (Figure 13E), performed in the same monolayers used for the TEER determinations, indicated that no significant decrease in viability was detected under any of the conditions tested.

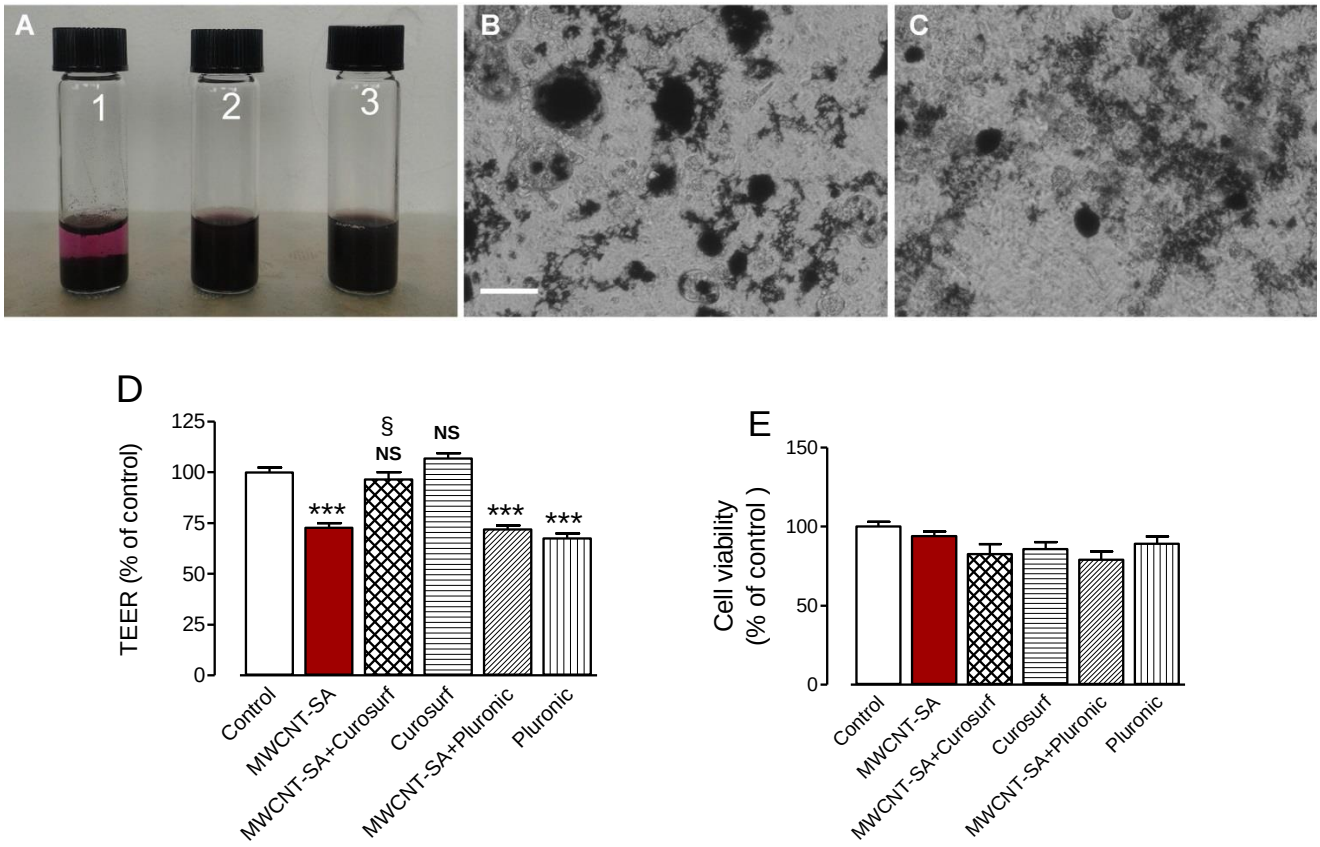

Figure 13. Effect of natural surfactant on MWCNT-SA aggregation and MWCNT-SA-induced TEER decrease. (A) MWCNT-SA (1 mg/ml) were suspended in non-supplemented culture medium (EMEM, 1) or in medium supplemented with Pluronic F127 (10 mg/ml, 2) or Curosurf® (8 mg/ml, 3), and the suspension was sonicated for 30 min. The image was taken 60 min after sonication. (B, C) MWCNT-SA (80 µg/cm^2) were added to Calu-3 monolayers in the absence (B) or in the presence (C) of Curosurf® (0.8 mg/ml). Images were taken after 3 d (bar=50 mm). (D and E) Confluent Calu-3 monolayers were incubated in normal culture medium or in culture medium supplemented with the natural surfactant Curosurf® (0.8 mg/ml) or with pluronic F127 (1 mg/ml). The incubation was performed in the absence or in the presence of MWCNT-SA (80µg/cm2). After 3 d, TEER (D) and cell viability (E) (resazurin method) were measured in the same monolayers. Data are shown as mean (n_{test}=4) ±S.D. As a negative control, cells were incubated without either surfactants or MWCNT. (D) ***p<0.001 versus control; NS, not significant versus control; § p<0.05 versus cells exposed to MWCNT without surfactants.

To investigate the mechanisms underlying the discrepancy between TEER measurements and cell viability assay in MWCNT-SA-treated monolayers, we investigated the response of Calu-3 cells by confocal microscopy.

4.5.1 Calcein/Propidium Iodide assay

Untreated Calu-3 cell monolayers accumulated calcein rather homogeneously, while very few cells were propidium positive (Figure 14A). These findings were confirmed by analysis of vertical sections (Figure 14B) and three-dimensional reconstructions (Figure 14C), which showed that the untreated Calu-3 cell monolayers were planar and intact. Propidium-positive (i.e. dead) cells appeared in Calu-3 cell monolayers exposed to MWCNT-SA for 24h (Figure 14D). However, the distribution of dead cells was not uniform throughout the cell population because propidium-positivity was detected mainly in the close proximity of MWCNT-SA aggregates. The vertical section at 24h of exposure (Figure 14E), taken in correspondence of the largest aggregates, also confirmed that the injury was restricted to cells in direct contact with the MWCNT-SA aggregate (arrows), while the remaining portion of the monolayer preserved its viability. Interestingly, there was no evidence of live cells present at top surface of the aggregates (imaged in reflection mode and showed in grey as pseudo-colour). The top surface resulted to be completely cell-free, as demonstrated in both the vertical section and the 3D reconstruction images (Figure 14F). On the contrary, after 8d of exposure to MWCNT-SA, confocal analysis showed that the tangles were almost covered by a monolayer of cells (Figures 14G, base of the aggregate; Figure 14H, aggregate top). The vertical section (Figure 14I) and the 3D reconstruction (Figure 14L) images evidenced that the majority of cells lying on the top of the aggregates were dead, with a minority of viable cells stained with green calcein (shown in Figure 14H by arrowheads). Notably, since propidium-positive cells were detected around the aggregates of smaller sizes than those shown in Figure14 (Figure 15) no definite threshold size of aggregates could be determined for contact-mediated cytotoxicity. Contact-mediated cytotoxicity was also found in monolayers treated with *tangle-like* MWCNT (NM400 and NM402); also in this case, propidium-positive cells were detectable in close contact with the aggregates (Figure 16).

In addition, the contact-mediated cytotoxicity was also observed in other two airway epithelial cell lines, BEAS-2B and A549 treated with MWCNT-SA (Figure 17).

Finally, the quantitative relationship between MWCNT-SA dose and cytotoxicity was determined by quantifying the number of propidium-positive cells. For the concentrations range adopted (0, 15, 30, 45 and 80 $\mu g/cm^2$), a significant linear relationship existed between MWCNT-SA mass

concentration and the percentage of dead cells after 8d exposure (Figure 18A). This result was in agreement with the TEER data which evidenced a significant linear dose-effect relationship between the change in resistance of the Calu-3 cell monolayer and the MWCNT dose (Figure 18B).

4.5.2 Caspase activity

Confocal microscopy analysis showed that after 8d of exposure to MWCNT-SA, caspase activity increased in several cells growing on the top of the aggregate (Figure 19A-B), whereas no caspase fluorescence was observed in untreated monolayers (Figure 19C). When co-stained with calcein, caspase-negative cells located at the top of the MWCNT-SA aggregates showed calcein positivity (Figure 19A-B), exhibiting a granular intracellular distribution of the dye (arrowheads). This distribution differed from the intracellular distribution exhibited by untreated cells (Figure 19C), which were completely filled with calcein, with some areas of enhanced positivity. Positive control was taken as a Calu-3 cell monolayer treated with pro-apoptotic drug doxorubicin (1 µM) for 24h (Figure 19D). Doxorubicin-treated monolayers (used as a positive control for apoptosis) exhibited widespread caspase activity similar to MWCNT-treated cultures, with several caspase-positive cells and calcein-positive cells characterized by the granular staining pattern.

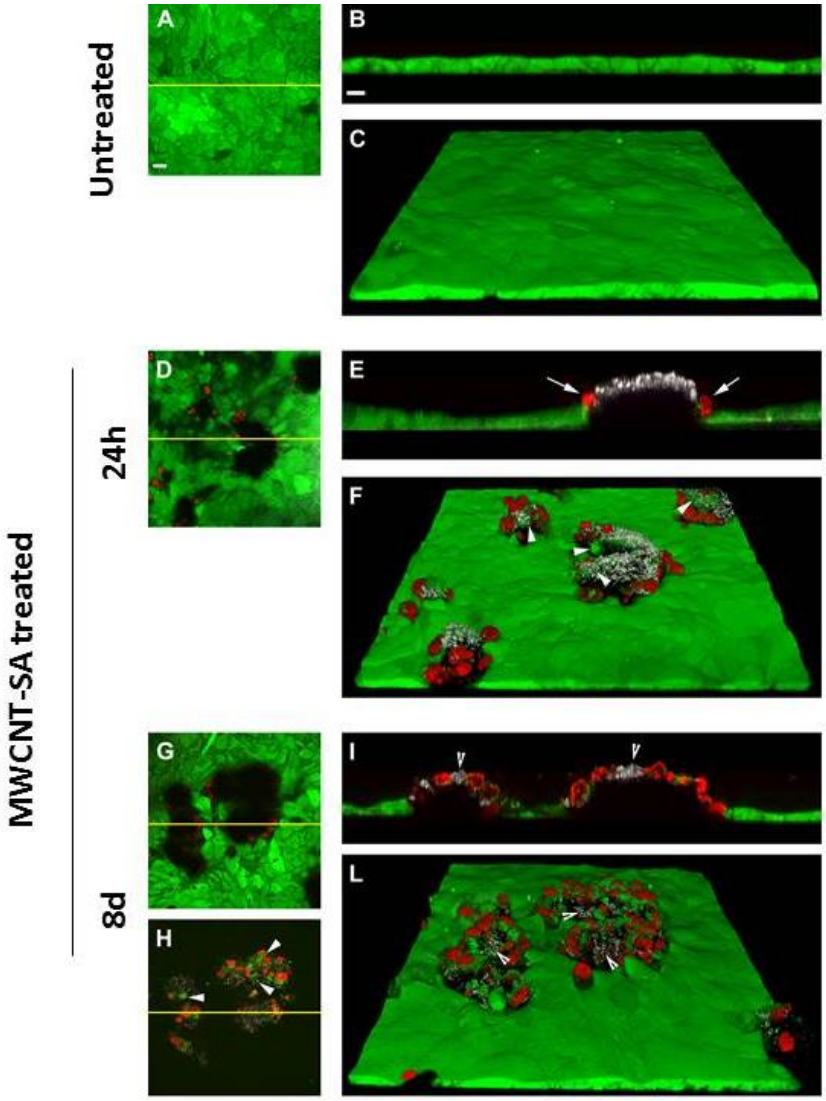

Figure 14. Confocal analysis of Calu-3 cell monolayers treated with MWCNT-SA. Confluent monolayers of Calu-3 cells were incubated in the absence (A–C) or in the presence of MWCNT-SA (80 μg/cm^2) for 24 h (D–F) or 8 d (G–L). Live cells are shown in green (calcein), while dead cells are visualized in red (propidium iodide, PI) and aggregate free surface, visualized from the reflected light, in grey. (A, D, G, and H) Single horizontal confocal sections taken at the level of the monolayer (A, D, G) or at the top of the MWCNT-SA aggregate (H). (B, E, and I) Vertical sections taken on the plan marked by the line shown in panels A, D, and G, respectively. (C, F, and L) Three dimensional reconstructions of z-stack confocal images. Scale bar: 20 μm. The experiment was repeated five times with comparable results.

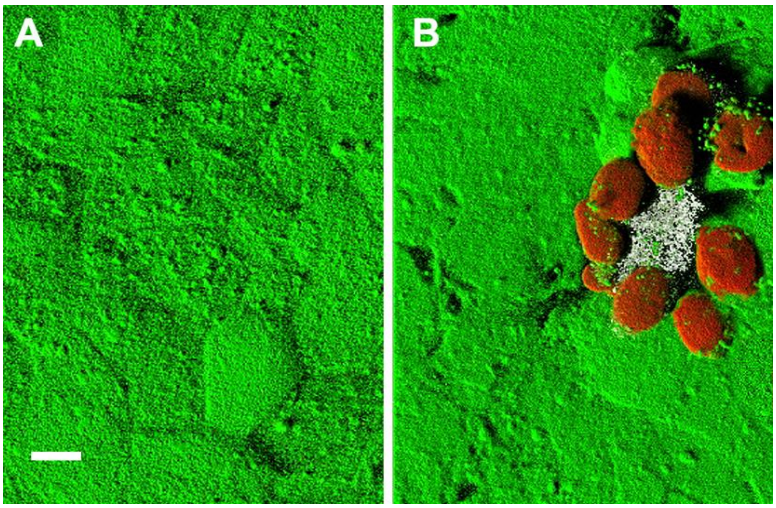

Figure 15. Contact-mediated cytotoxicity is observed also with small MWCNT-SA aggregates. Confluent monolayers were incubated for 8d in the absence (A) or in the presence (B) of MWCNT-SA (80 μg/cm^2), added to the apical chamber of the culture insert. Cells were pre-incubated with calcein-AM and propidium iodide for 15 min before the observation and observed with CLSM through a 63x (1.4 NA) oil objective. Three-dimensional reconstructions of the monolayers using the "shadow" algorithm of the software are shown (see Methods). Signals of calcein (live cells), propidium (dead cells), and reflected light (MWCNT-SA aggregates) are rendered in green, red, and grey scales, respectively. Bar = 10 μm.

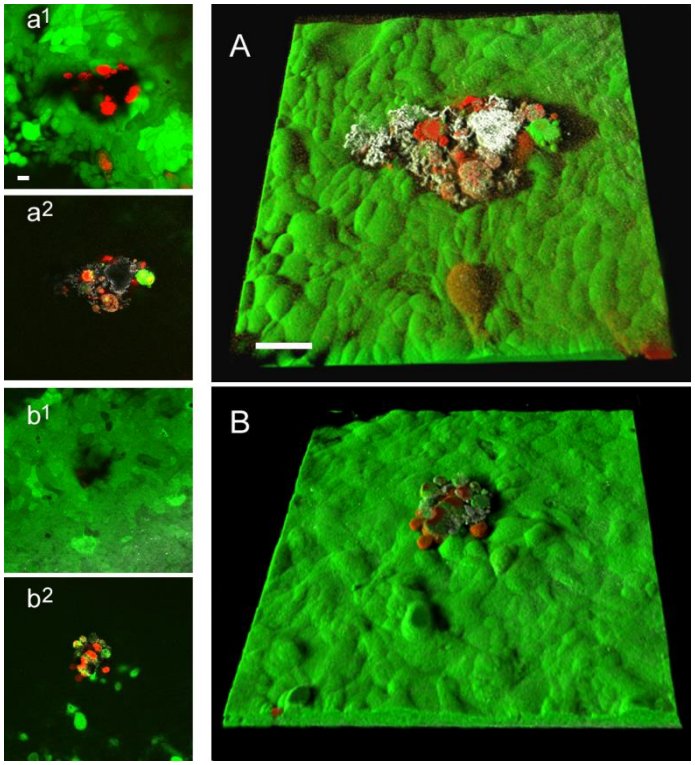

Figure 16. Confocal images of Calu-3 cell monolayers treated with NM400 (A, a1, a2) and NM402 (B, b^1, b^2) MWCNT (both at 80 μg/cm^2) for 8d. Live cells are shown in green (calcein), while dead cells are visualized in red (PI). (a^1, a^2, b^1, b^2) Single horizontal confocal sections taken at the level of the monolayer (a^1, b^1) or next the top of the MWCNT aggregate(a^2, b^2). (A, B) Three-dimensional reconstructions of z-stack confocal images. The free surface of MWCNT aggregates is visualized in grey. Scale bars: 20 μm, a^1, a^2, b^1, b^2; 50 μm, A, B. The experiment was repeated 3 times with comparable results.

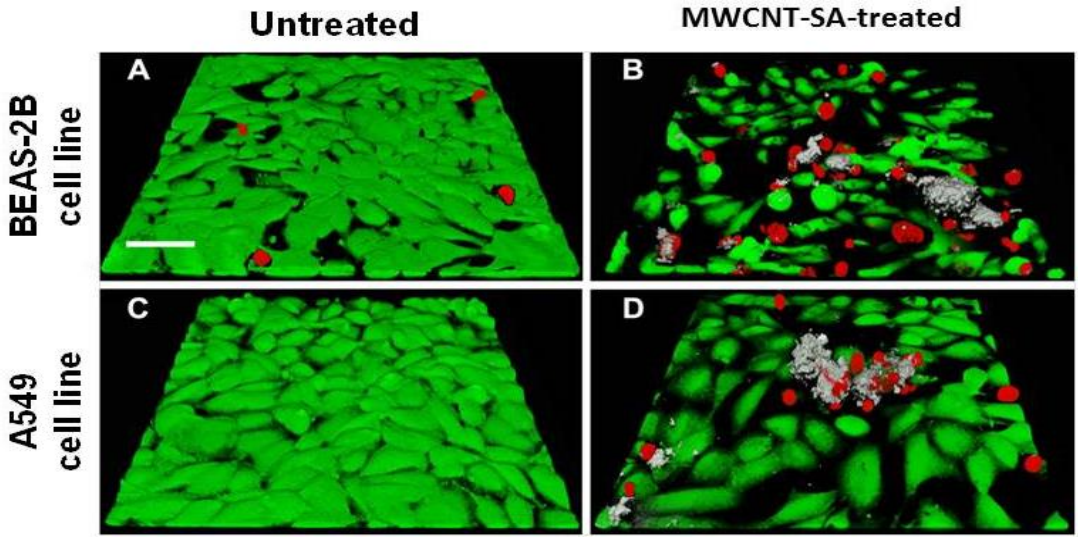

Figure 17. Cytotoxicity induced by MWCNT-SA aggregates in BEAS-2B and A549 cells. Three-dimensional reconstructions of z-stack confocal images of representative fields of BEAS-2B (A, B) and A549 (C, D) cell monolayers stained with calcein-AM (in green) and propidium iodide (in red). (A, C) Untreated monolayers; (B, D) monolayers incubated with MWCNT-SA (80 μg/cm^2, 8d). Scale bar: 50 μm

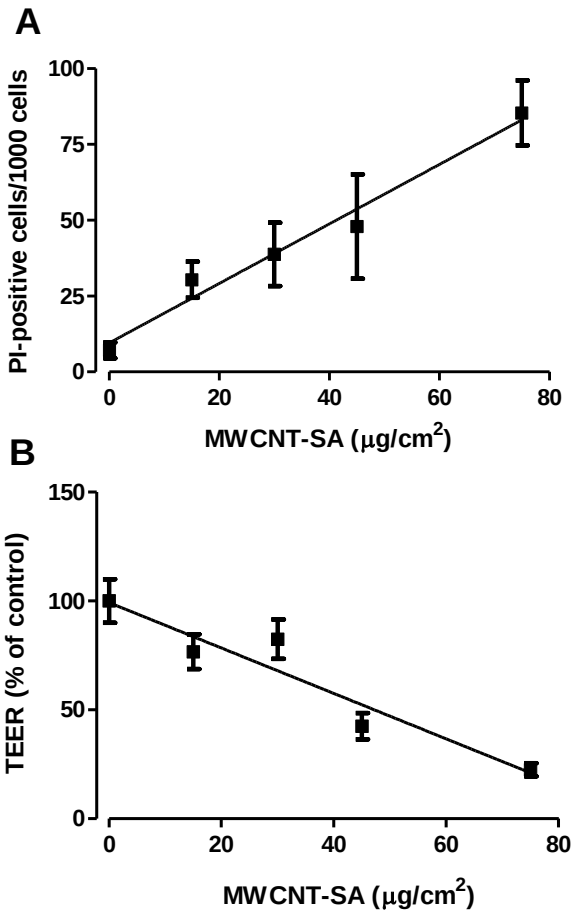

Figure 18. Dose-dependency of MWCNT-SA-induced changes in TEER and cell viability. Confluent monolayers of Calu-3 cells were incubated in the absence or in the presence of increasing doses of MWCNT-SA (15-80 μg/cm^2). After 8d TEER was measured (B) monolayers were visualized at confocal microscope (see Figure 12) and propidium-positive cells were counted (see Methods). Data are shown as (A) mean values (n_{test} = 4) ± S.D. and as (B) mean TEER changes (% of control, n_{test} = 4) ± S.D. Straight lines represent the best fit linear regressions.

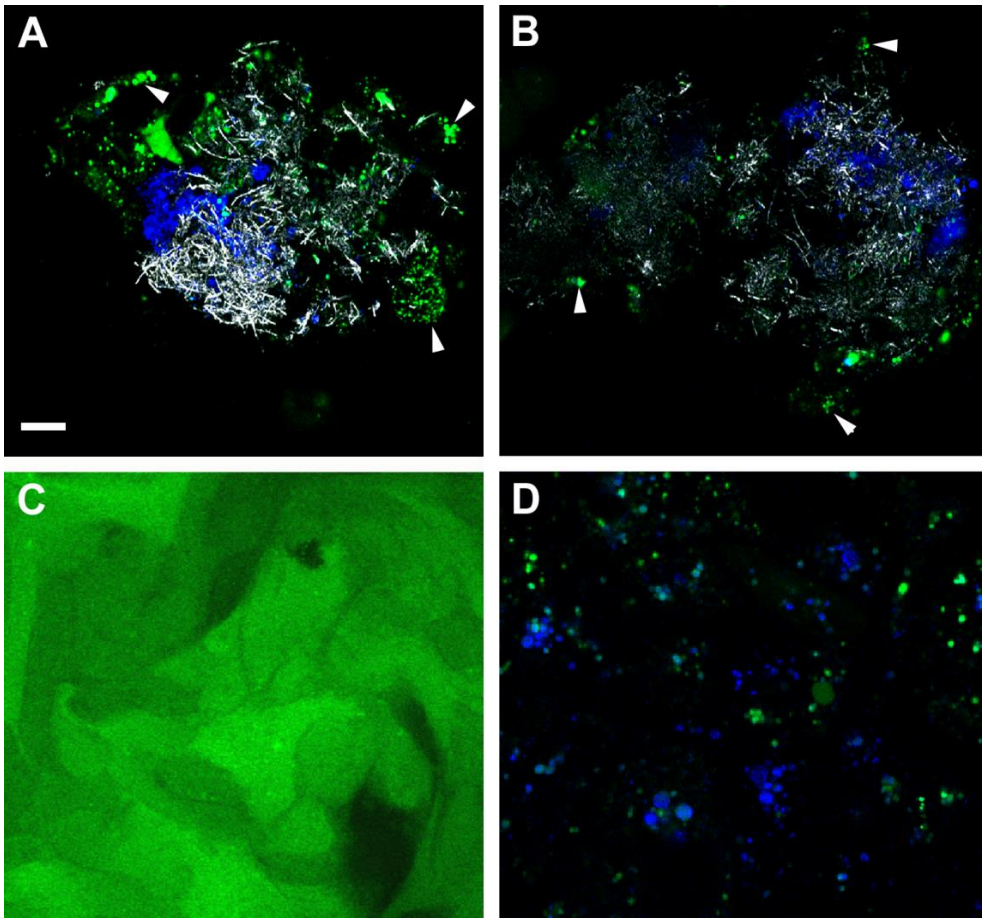

Figure 19. Caspase-positivity in MWCNT-SA-treated Calu-3 monolayers. Figure reports representative confocal images of Calu-3 cell monolayers treated with MWCNT-SA (A and B) (80 µg/cm^2, 8d); untreated (C); or treated for 1d with 1 µM doxorubicin, used as a positive control for apoptosis (D). Monolayers were stained with calcein-AM and with sulforhodamine-labelled caspase-inhibitor (for caspase activity). (A, B) Cells adherent to MWCNT-SA aggregates showed high caspase activity. Single horizontal sections, taken at the top of two MWCNT aggregates, are shown. (C) Representative field of an untreated Calu-3 cell monolayer. (D) Representative field of a caspase-positive Calu-3 cell population. Caspase signal is rendered in a blue scale, while calcein is in green and MWCNT surface is in grey. Scale bar: 10 µM.

4.6 Analyses in fixed cell monolayers

4.6.1 Cell proliferation

The positivity to the nuclear Ki-67 antigen was used to evaluate the proliferative behaviour of Calu-3 cell monolayers incubated for 8d in the absence or in the presence of MWCNT-SA. This assay has been widely adopted in the scientific literature to detect actively cycling cells in normal and tumour tissues[88]. Although several isolated Ki-67-positive cells were detectable in the untreated Calu-3 cell monolayers (due to their origin from a neoplastic population with high basal

proliferative activity), an increased presence of cells in active proliferation were detectable in proximity and around MWCNT aggregates (Figure 20).

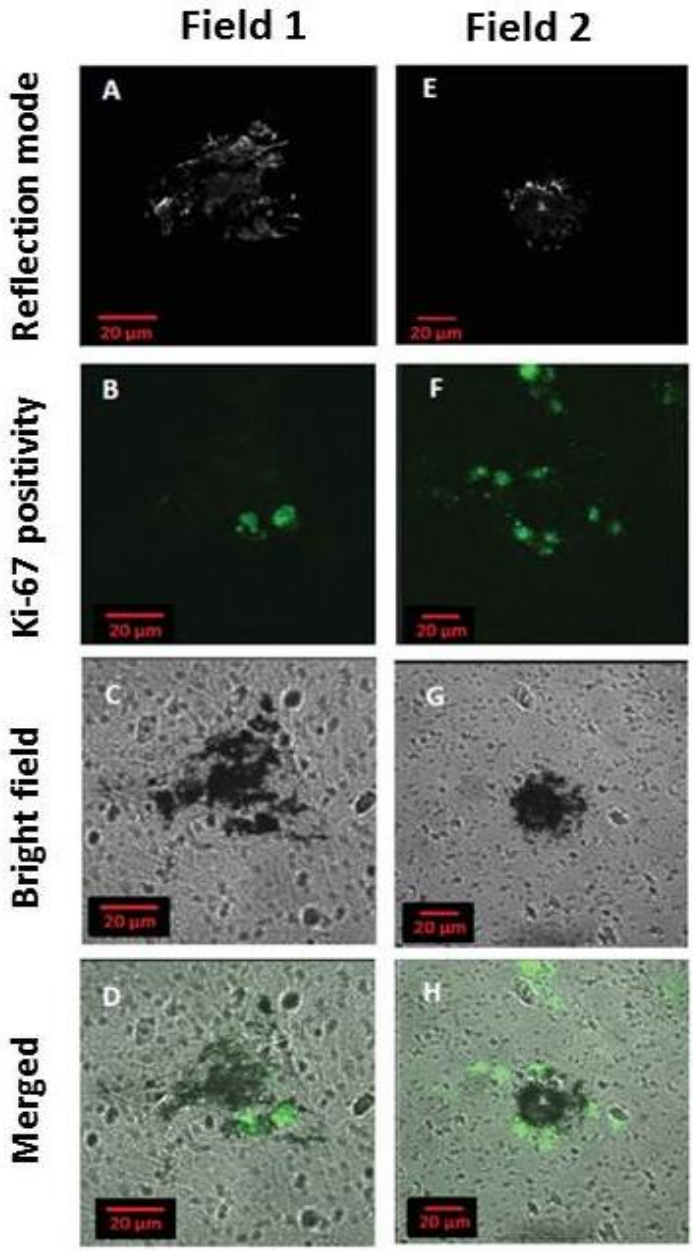

Figure 20. Confocal microscopy images of Calu-3 cell monolayers treated with MWCNT-SA (80 µg/cm^2, 8d) and stained for Ki-67 positivity. Two representative fields (A-D and E-H) are shown. (A, E) Reflection mode showing the surface of MWCNT-SA aggregates in grey scale. (B, F) Ki-67 positivity (green scale): actively proliferating Calu-3 cells are visible in close proximity to MWCNT aggregates. (C,G) Bright field images: MWCNT-SA aggregates appear as black masses. (D, H) Merged images of (A. B, C) and (E, F, G), respectively. Scale bars: 20 µm.

4.6.2 Changes in the organization of F-actin filaments

Actin organization was investigated after exposure to MWCNT-SA and compared to untreated control (Figure 21).Untreated cell monolayers showed evident, well-organized cortical actin and tightly packed cells (Figure 21A). Differently, after exposure to MWCNT-SA for 8d (Figure 21B), cells in direct contact to MWCNT aggregates changed their shape, so as to ensure a close contact with the surface of the aggregates of nanofibers. The rest of the monolayer appeared unchanged, thus suggesting that rearrangement took place only in focal areas in close contact with the MWCNT-SA aggregates.

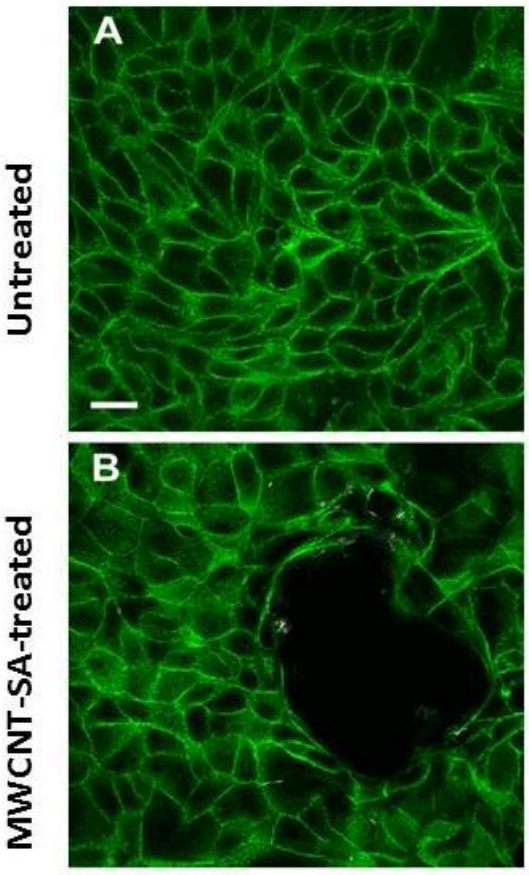

Figure 21. Confocal microscopy images of Calu-3 cell monolayers incubated for 8d (A) in the absence or (B) in the presence of MWCNT-SA (80 μg/cm^2). F-actin filaments were stained in green. Direct contact with MWCNT aggregates modified the organization of the actin filaments. Scale bar: 20 μM

4.6.3 NF-κB

The nuclear factor NF-κB pathway has long been considered a prototypical proinflammatory signaling pathway [92]. The translocation of the transcription factor NF-kB into the cell nucleus was used to evaluate the pro-inflammatory response of Calu-3 cell monolayers incubated for 8d in the absence or in the presence of MWCNT-SA. An increased expression of NF-κB, limited to cells adjacent to MWCNTs aggregates, was evident (Figure 22).

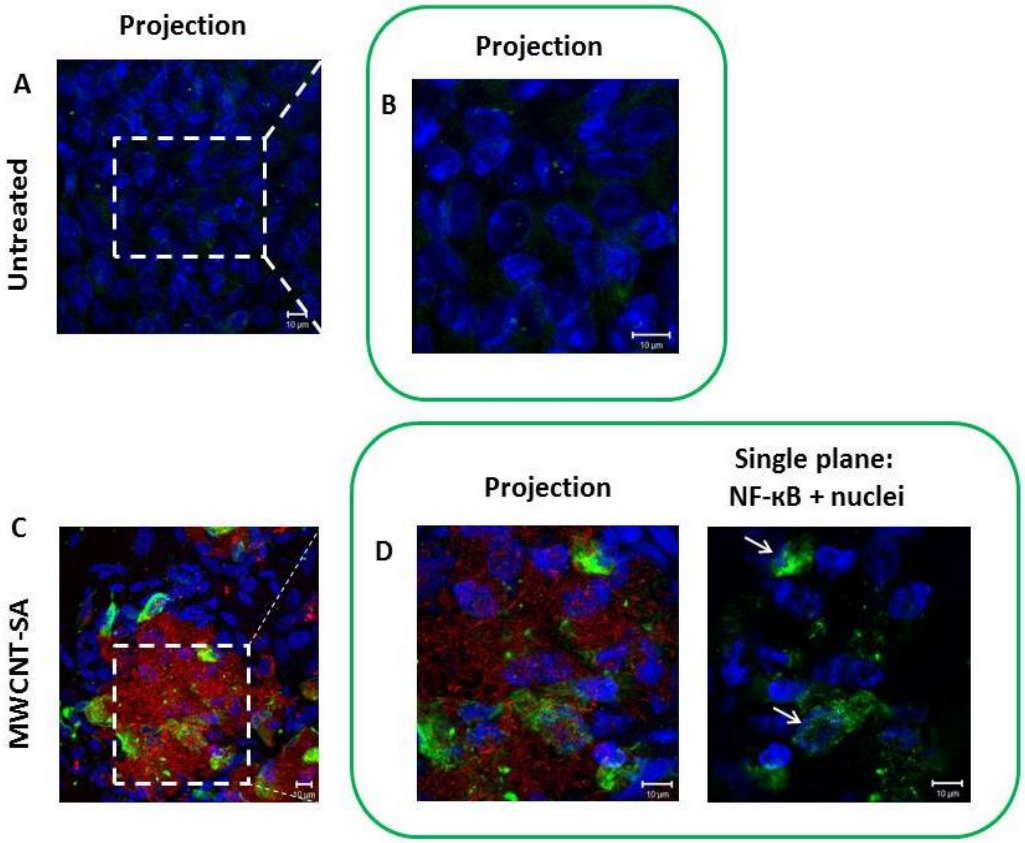

Figure 22. Confocal microscopy images of Calu-3 cell monolayers treated with MWCNT-SA (80 µg/cm^2, 8d) and stained for NFκB. (A-D) Representative confocal images of cell monolayers (A,B) untreated or (C,D) exposed to MWCNT-SA and stained for NFκB (in green) and nuclei (in blue). MWCNT-SA were imaged in reflectance mode and are shown in red as pseudo-colour. Scale bars: 10 µm (63× magnification). (B, D) Magnification of image A and B, respectively. Translocation of NFκB into the cell nucleus is highlighted by arrow.

DISCUSSION

In this part of the thesis we focus our attention on the identification of structural determinants of toxicity, *in vitro*, of four preparations of multi-walled carbon nanotubes with different length, morphology, and level of metal contaminants. It is important to study the toxicity of these materials, because MWCNT are suspected to have potential toxic properties analogous to those observed with other fibrous particles, such as asbestos[63]. We have assessed, the biological effects of NM400, NM401, NM402 and MWCNT-SA on macrophage cell lines and epithelial cells.

These four preparations of MWCNT are commercially available multi-walled carbon nanotubes, and more specifically, NM400, NM401 and NM402 belong to the JCR Repository of Representative Test Materials, and they will be likely reference materials in nanotoxicology studies.

4.7 Determinants of toxicity in macrophages

Since inhalation is the major way of interaction with MWCNT, their effects were studied on two macrophage cell lines (MH-S and RAW264.7) which, *in vivo*, are the first to contact the inhaled particles. Indeed, they are designate for engulf and digest cellular debris, foreign substances, microbes, and cancer cells in a process called phagocytosis. They play a critical role in innate immunity, determining the final outcome of the interaction between the organism and the material. Airway macrophages are specialized for interacting with inhaled particles and their exposure to MWCNT may lead to distinct types of macrophage activation, which account for different pathologic outcomes.

To study the biological effects of MWCNT on macrophage cell lines we analyzed different endpoints, such as cell viability, phagocytic activity and pro-inflammatory M1 macrophage activation. The main result obtained is that NM401 and MWCNT-SA are more toxic than NM400 and NM402. The interpretation of these results requires some considerations about the structural properties of the four preparations of MWNCT[93].

From the morphological point of view, NM400 and NM402 are *tangle-like* MWNCT; they tend to agglomerate in a structure like tangles, whereas NM401 and MWCNT-SA are *needle-like* MWCNT, longer, rigid and straight fibres as those observed with asbestos. Moreover, significant differences also exist for the length, with NM401 and MWCNT-SA much longer than NM400 and NM402 (MWCNT-SA>NM401>NM402>NM400). Length has been suggested to play a critical role in the MWCNT biological reactivity after inhalation. According to a well-established paradigm for high aspect ratio nanomaterials, MWCNT with length superior to that phagocytic cells can

induce inflammatory response, which is an important event contributing to tissue remodeling and carcinogenesis[93]. Indeed, MWCNT of length >8μm cannot be easily engulfed by macrophages leading to frustrated phagocytosis[94-95].

The diameter is another critical factor that must be taken into account in the toxicological assessment of MWCNT[96-97]. Fenoglio et al. and Nagai et al. reported that thinner MWCNT appear more toxic than thicker MWCNT both in *in vitro* and *in vivo* experiments. In our hands, the two preparations of MWCNT (NM401 and MWCNT-SA) which are more toxic are also the thicker ones. Therefore, the biological effects of MWCNT observed here do not seem to follow the predictions of Fenoglio and Nagai.

Also metal impurities are important determinant for the evaluation of toxicity of MWNCT. Several studies, for example, compare the toxic effects of MWCNT with an high level of Co, Fe, Mo e Ni, and MWCNT without metal impurity, finding a greater toxicity of the MWCNT with metal contaminants[98-99] which can diffuse in the medium of cells. In this study (see *results 4.1*) we have reported no dissolution of the metal contaminants in cell medium for NM401, NM402 and MWCNT-SA. Thus, the greater toxicity of NM401 and MWNCT-SA cannot be due to the metal contaminants. Instead, maybe there is a correlation between the low toxicity of NM402 and the absence of metal contaminants in the medium of cells. The very low toxicity of NM400 suggest that the concentrations of metal impurities present in the incubation medium are too low to affect toxicity.

Finally, after the treatments with NM400 and NM402, but not with NM401 and MWCNT-SA, in both macrophage cell lines, we reported an increase in *Nos2* expression and a corresponded increase in NO production, markers of the pro-inflammatory M1 macrophage activation. Therefore, the two shorts and tangle-like preparations of MWCNT, likely engulfed by macrophages, are able to activate these cells, as opposed to long and *needle-like* MWNCT. The activation of RAW264.7, after exposure to MWCNT, as demonstrated by the induction of *Cox-2* and *Nos2*, had been already demonstrated by Lee et al[100]. Moreover, Bussy et al[93] demonstrated that short MWCNT enhanced pro-inflammatory and pro-oxidative response more than long MWNCT. These data and our results suggest that phagocytosis is a main step for the M1 macrophage activation by nanomaterials with a low acute toxicity.

In conclusion, we found that the main determinants of toxicity for macrophage cell lines, are likely the length and the *needle-like* shape, which hinder, or even prevent, phagocytosis. Indeed, the greater toxicity of NM401 and MWCNT-SA, demonstrated by the decrease in cell viability and the alteration of functional activity, are ascribable to their greater length and to their morphological

structure. On the contrary, reduced length and *tangle-like* shape (NM400 and NM402) promote M1 macrophage activation since these materials are completely engulfed by macrophages.

4.8 Determinants of toxicity in epithelial cells

Airway epithelium represents one of the first body barrier encountered by MWCNT dispersed in the environment[101]. An *in vitro* model consisting of Calu-3 cell monolayers grown on permeable filters in a double-chamber culture system was adopted to mimic the airway epithelial barrier. Under these conditions, Calu-3 cells, which are derived from a human lung adenocarcinoma, form tight junctions, show strictly polarized secretory and transport functions, prevent the trans-epithelial passage of paracellular substrates and participate in signal transduction[102-103], thus representing an *in vitro* model of a functional epithelial barrier. For this reason, Calu-3 cells have been used to predict the behavior of the respiratory barrier *in vivo*[104] and as a model to study airway permeability to nanomaterials[105-106-107]. Monolayers of human bronchial epithelial cells (BEAS-2B) and human lung alveolar carcinoma cells (A549) were also used for comparison.

Given the high tendency of MWCNT to aggregate[108-109-110] and the presence of aggregates in the airway walls of exposed animals[111-112-113], our working hypothesis was that MWCNT aggregates might elicit peculiar toxic responses in the lungs. Indeed, numerous *in vivo* studies have already demonstrated that MWCNT, when instilled into the lungs of rodents, have the potential to cause transient inflammatory changes, granuloma formation, and fibrosis in the lung tissue[11]. Long (>20 μm), straight MWCNT have also been shown to have the potential to cause inflammation and granuloma formation in the mesothelial lining of the pleura, consistent with the pathogenic behavior of asbestos. Therefore, our aim is to investigate if MWCNT produced a barrier impairment. The behavior of epithelial cells was studied both at the monolayer (cell population) and at the single-cell level. At a cell-population level, Trans-Epithelial Electrical Resistance (TEER) was used as an indicator of barrier competence, caspase activity was assessed with standard biochemical assays, and cell viability was investigated with both standard biochemical techniques and an high throughput (HTP) technique, based on automated epifluorescence microscopy, whereas at cell level the response to MWCNT was investigated with confocal microscopy, by evaluating cell death (calcein/propidium iodide), proliferation (Ki-67), inflammation (NF-κB) and apoptosis (caspase activity).

We decided to focus our attention on MWCNT-SA since they are *needle-like* shape and the longest MWCNT used for this work (5-9μm vs 2-6 μm of NM401, other *needle-like* MWCNT). It is well know that the *needle-like* shape and the greater length are two of the main structural parameters involved in the fibre paradigm[63]. The results presented in this study show that aggregated

MWCNT-SA hinder the barrier properties of airway cells, as demonstrated by a dose-dependent decrease in TEER.

We have concluded from pre-existing evidence on carbon nanotubes[115] and asbestos[63], as well as from our own experimental results, that aggregates of MWCNT-SA are endowed with peculiar toxic properties, such as the ability to decrease TEER. Indeed, when MWCNT-SA aggregation tendency was decreased with a natural surfactant, TEER decrease was prevented, indicating that it was attributable to aggregates rather than dispersed MWCNT-SA. In addition, several findings[116-117] support our assumption that the possibility of being exposed to single MWCNT is low, due to their tendency to aggregate into bundles. These main findings were confirmed also with NM400 and NM402 (the two *tangle-like* MWCNT used here) which are much thinner but nonetheless also form aggregates as shown in Figure 16.

The importance of aggregation for the pulmonary toxicity was also proposed for single-walled carbon nanotubes (SWCNT), leading to the speculation that the aggregation of these materials, rather than their large aspect ratio accounted for the toxic effects[118]. In particular, foci of granulomatous lesions and collagen deposition were associated with dense particle-like SWCNT agglomerates[119]. Although no changes in cell viability are detected by different biochemical assays at the cell population level, confocal microscopy on living monolayers showed a noteworthy difference. In particular, confocal microscopy analysis demonstrated that the viability of cells adherent to MWCNT-SA aggregates was severely affected, as indicated by the positivity of these cells to PI. Propidium-positive cells were already detectable after a 24 h contact with MWCNT-SA aggregates, indicating that short-term exposure times were sufficient to induce cell death and localized cell monolayer damage. Interestingly, cell monolayers impairment was dose-dependent and correlated well with the TEER changes. The dose–effect relationship shown in Figure 18A indicates that propidium-positive cells correspond to approximately 8% of the total cell population at the maximal mass concentration of MWCNT-SA tested. This low percentage may well explain why MWCNT-SA-induced cytotoxicity is not detected by conventional assays at whole cell population level. Additionally, these results are in agreement with the low cytotoxicity of MWCNT reported on epithelial models in vitro[120] and with the transient inflammatory changes detected in the lungs in vivo[111]. Finally, the absence of a widespread damage to the cell monolayer is hardly compatible with the potential sequestration of essential components from the medium by adsorption onto MWCNT surface, a mechanism proposed to account for MWCNT cytotoxicity[121]. In contrast, HR-TEM and TGA analyses (see physico-chemical results, 4.1.2) ruled out that MWCNT-SA cause cell damage through the diffusion in the medium of toxic factors, such as possible metal or organic contaminants, which were not detected in the MWCNT-SA preparation. The visualization of F-actin

filaments constituting the cell cytoskeleton (Figure 21) demonstrates that Calu-3 cells react to the presence of MWCNT-SA aggregates changing their shape and cytoskeletal organization. Thus, similarly to what observed for SWCNT aggregates[122], Calu-3 cells adhered actively to MWCNT tangles, as the first step in a colonization process. A direct interaction between actin cytoskeleton and SWCNT has been also recently described[123]. However, in that case, SWCNT were dispersed and aggregates eliminated before cell treatment. In the experiment shown in Figure 21, no dispersing agent was utilized making, therefore, unlikely a direct interaction between the actin and the nanomaterial. Conversely, it is likely that epithelial cells reorganize their cytoskeleton to allow an active and close adherence to the nanomaterial. It is known that the characteristics of the adhesion surfaces have considerable consequences on the cell shape and, hence, on the cell fate[124-125]. MWCNT-SA surface is highly irregular, as clearly shown by the confocal images in reflection mode (Figure 14), and may not allow firm focal adhesions by the epithelial cells[126-127]. In addition, epithelial cells are more sensitive than other cell types to anoikis, a form of apoptosis promoted by absent or wrong signals from membrane adhesion complexes[128]. Since the death process triggered by MWCNT-SA aggregates seems asynchronous and involves individually caspase-positive cells, we suggest that anoikis-mediated apoptosis is a likely mechanism of the localized cytotoxicity of MWCNT-SA aggregates, although further studies are needed to confirm this form of cell death. However, as in the case of cell viability, conventional assays of caspase activity at whole cell population level did not detect significant apoptotic changes (Figure 12C). Singularly localized apoptotic death would also be consistent with the relatively small inflammatory response associated with exposure to MWCNT found in vivo[129-111]. Apoptosis occurrence in epithelial monolayers exposed to nanomaterials has been also described in Caco-2 cells treated with polystyrene nanoparticles[130]. In our in vitro model, proliferating cells were detected at high frequency in proximity of MWCNT-SA aggregates, as evidenced by the Ki-67 positivity (Figure 20). It is tempting to attribute this behavior to the proliferative drift due to the MWCNT-induced cell death and the consequent loss of contact inhibition in the monolayer. Intriguingly, also the exposure of airway epithelium to MWCNT in vivo is associated with an hyper proliferative behavior, consisting in areas of epithelial hyperplasia[129] or ‘‘thickening of epithelial cell layers’’[131] detected in close proximity of nanomaterial aggregates. Moreover, we reported an increase in expression of NF-κB only close to MWCNT-SA aggregates (Figure 22) suggesting an up-regulation of this molecular pathway, as demonstrated in THP-1 cell exposed to functionalized MWCNT[132]. Here, we proposed a pro-inflammatory response based on the role of NF-κB in the expression of pro-inflammatory genes including cytokines, chemokines, and adhesion molecules, although further studies are needed to confirm this theory.

In conclusion, we found that the main determinant of toxicity for epithelial cells depends on the actual shape in which MWCNT get in contact with the cells and, in particular, if they form aggregates. We showed that when human airway epithelial cells are exposed to MWCNT aggregates, distinctive, localized cytotoxic effects are detectable only when adopting an advanced imaging approach. Thus, our results not only support previous data showing the potential for MWCNT aggregates to induce lung toxicity at relatively low doses but also provide methodological tools for advanced imaging of MWCNT–cell interaction.

CHAPTER 6

AMORPHOUS SILICA NANOPARTICLES

RESULTS

6.1 Physico-chemical properties of ASNP

The synthetic amorphous silicon dioxides (SAS) used in this work are produced industrially by two general methods: wet route (precipitation) or thermal route (pyrogenesis). NM200 (colloidal silica) was produced by wet route, in which a solution of alkali metal silicate is acidified to produce a gelatinous precipitate that is washed and then dehydrated to produce colourless microporous silica particles. NM203 (pyrogenic silica) was produced via the thermal route, that is burning $SiCl_4$ in an oxygen-rich hydrocarbon flame to produce a fume of SiO_2.

A detailed physico-chemical characterization of NM200 and NM203 was provided in the JRC Reports [133]. Primary particle size of NM200 and NM203 measured by TEM are in the range 14 ± 7 nm and 13 ± 6 nm, respectively. TEM analysis showed that NM200 and NM203 consist of highly porous nanostructured materials that are agglomerates and aggregates of primary particles. The pyrogenic NM203 seems to have more complex and branched structure than the precipitated NM200.

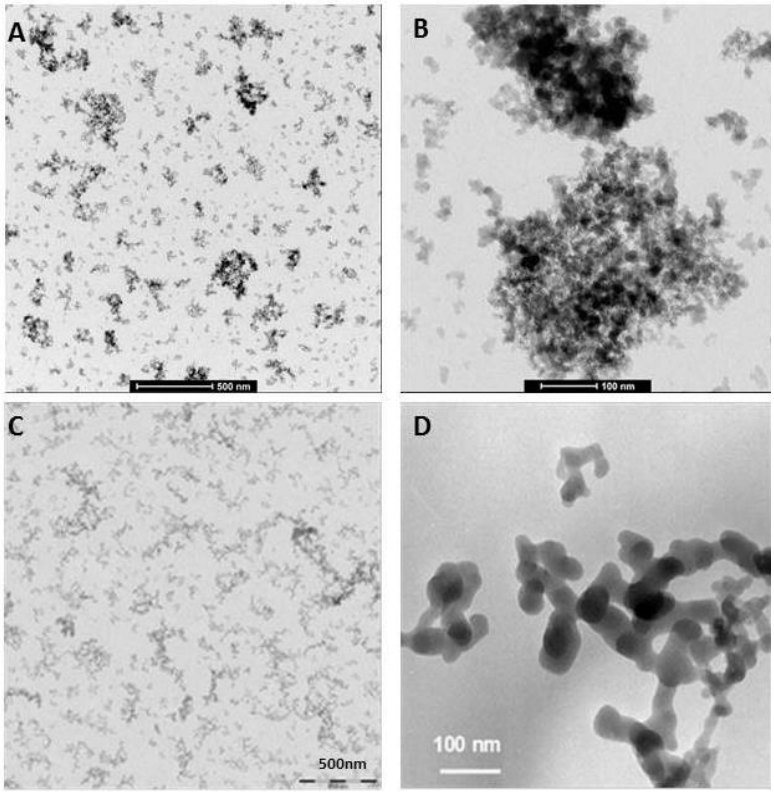

Figure 23. Representative TEM micrograph of NM200 (A-B) and NM203 (C-D). TEM micrograph of well-dispersed sample taken for quantitative TEM-analysis; scale bar is 500nm (A-C). (B) Micrograph of NM200, illustrating the occurrence of large agglomerates of aggregates; scale bar is 100nm. (D) TEM micrograph showing the complex open network structure in the silicon dioxide aggregates; scale bar is 100nm.

The ASNP, NM200 and NM203 are rather homogenous and pure consisting of 96% and 99% of SiO_2, respectively. NM200 contains Al (4600 ppm), Na (8800 ppm) and S (8700 ppm) impurities identified by ICP-OES; S and Na are present as Na_2SO4 which is a by-product from the synthesis. NM203 contained impurities of Al (4300 ppm) and S (400 ppm) identified by EDS. The TGA analysis showed a significant mass loss below 100°C for NM200, which may be assigned to the loss of water absorbed on the surface. NM203 exhibits a phase transition at 324°C observed by Differential Thermal Analysis (DTA). The measured 24-hour dissolution ratio (for methods see *Results 4.1*) revealed that both ASNP and the Al impurities are partially soluble in the three media but the amounts vary considerably depending on medium, as does the relative amounts of dissolved Al impurities compared with dissolved Si, suggesting that the solubility behaviour depends on the medium. The evolution of O_2 (to measurement of hydro-chemical O_2 Activity) level during 24 hour incubation was measured in the same three different media used for the measurement of dissolution ratio. In the 0.05% BSA-water and Gambles solution NM200 showed negligible reactivity. In Caco-2 media, a negative dose-response relation was observed with decreasing dO_2 level with increasing concentration of NM200. The results suggest that NM-200 is inactive or reductive in the different

incubation media. Conversely, in all the three media the level of dO2 increased with increased concentration of NM-203, suggesting an oxidative reactivity.

As zeta potential is concerned, samples were stable and no sedimentation occurred during the measurements. The average aggregate sizes measured by DLS were roughly constant over the pH range. When dispersed in PBS, the PdI (polydispersity index) of NM200 remained quite high (> 0.3), consistently with the presence of large aggregates, while for the NM203 no big aggregates were seen. When NM200 and NM203 were dispersed in culture media without serum protein, NM200 presented some turbidity as in water and a high PdI (≈ 0.5), while NM203 was well dispersed with a relatively low PdI (≈ 0.2). When NM200 and NM203 were dispersed in culture media with serum proteins, an increased diameter of the particles was observed in both cases, even if NM203 remained rather well dispersed (PdI < 0.2). The use of different media inevitably has influences on the measured size. Depending on ionic strength, pH and presence of proteins etc., a corona of specific thickness is formed around the nanoparticles influencing their hydrodynamic size Finally, the Zeta potential values measured in pure water for both ASNP, had a nominal value larger than 30 mV, indicating a good stability of the suspension.

Both ASNP have SSA of the same order of magnitude: 189.2 m^2/g (NM200) and 203.9 m^2/g (NM203), as measured by the BET method.

6.2 Effects on macrophage viability of ASNP

The effects on cell viability of NM200 and NM203 (doses range from 0 to 80 $\mu g/cm^2$; exposure times 24, 48 and 72h) were assessed in both MH-S and RAW264.7 macrophage cells with the resazurin assay. In MH-S cells a marked dose-dependent decrease of viability was recorded throughout the range of NM200 and NM203 doses, with an larger effect observed with NM203 (Figure 24A-B). In RAW264.7 cells, NM200 caused a mild cytotoxicity, while NM203 caused a significant dose-dependent decrease of cell viability only at 72h (Figure 24C-D). In summary, for MH-S cells, the IC_{50} values (72h) were 16.2 $\mu g/cm^2$ for NM200 and 3.9 $\mu g/cm^2$ for NM203; for RAW264.7 cells the IC_{50} values (72h) were >80 $\mu g/cm^2$ for NM200 and 40 $\mu g/cm^2$ per NM203.

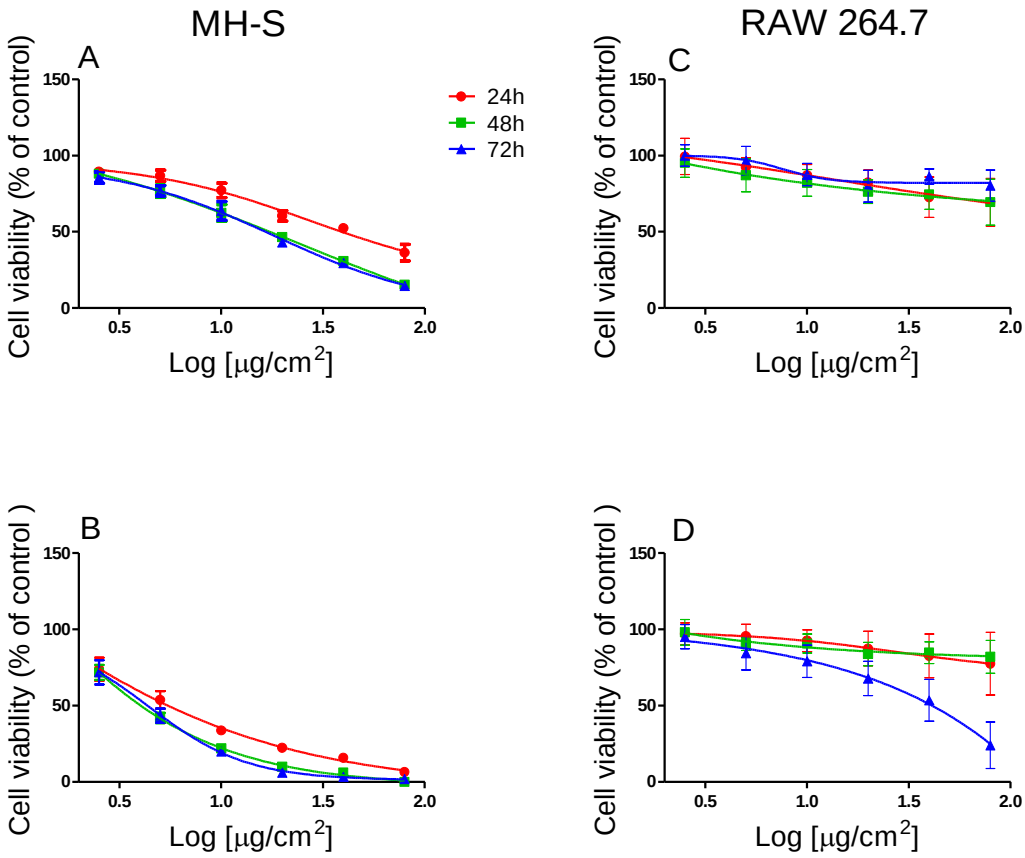

Figure 24. Viability of MH-S and RAW264.7 cells after exposure to ASNP. Cells, grown for 24h in complete growth medium, were treated for 24, 48 and 72h with NM200 (A-C) and NM203 (B-D). At the end of the incubation, cell viability was assessed with the resazurin assay. Data are means +/- SD of 10 independent determinations in two separate experiments.

6.3 Interaction of ASPN with MH-S and RAW264.7 macrophages

The internalization of ASNP was assessed in MH-S (Figure 25A) and RAW264.7 (Figure 25B) cells after a 24h-exposure. Confocal microscopy images evidenced that ASNP (imaged in reflectance mode) were effectively internalized into the macrophages and detected within the cells cytoplasm (Figure 25). No significant differences in the cell internalization were evidenced between MH-S and RAW264.7 cells when exposed to ASNP or between cells exposed to NM200 or NM203.

MH-S (Figure 26) and RAW264.7 (Figure 27) cells were imaged by He-Ion Microscopy (HIM) after 24h-exposure to NM200 and NM203. Untreated cells cultured for 24 h were also imaged for comparison. Interestingly, with this technique many ASNP aggregates could be found in close proximity of the exposed cells and, in some cases, cells surface was partially or completely covered by a ASNP layer. In general, as shown by the representative fields shown in Figures 26 and 27,

NM203 seemed to form aggregate layers onto the cell surface more readily than NM200. Moreover, MH-S interacted with NM200 aggregates more closely than RAW264.7 cells.

In general, as suggested by the representative fields shown in Figures 26 and 27, NM203 seemed to form aggregate layers onto the cell surface more readily than NM200. Moreover, MH-S interacted with NM200 aggregates more closely than RAW264.7 cells.

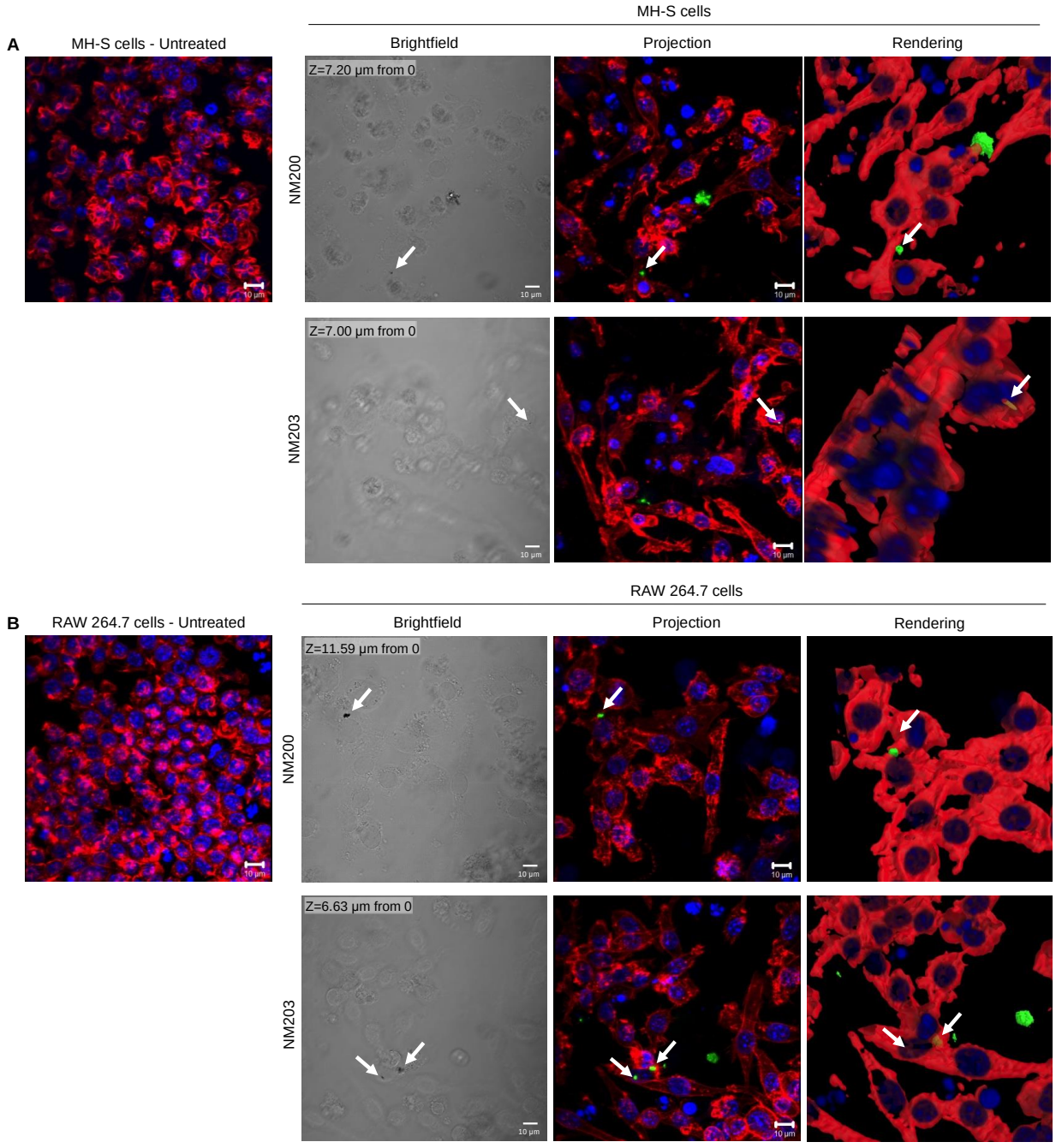

Figure 25. Cellular internalization of ASNP in MH-S and RAW264.7 cells after a 24h exposure to 10 µg/cm^2 of the indicated ASNP. Projections and rendered reconstructions of representative confocal images of MH-S (A) and RAW264.7 (B) cells stained with rhodamine phalloidin (F-actin, in red) and Hoechst 33342 (nuclei, in blue) are shown. ASNP were imaged in confocal reflectance mode and are shown in green as pseudo-color. The localization of ASNP (indicated by arrows) in the cell cytoplasm is evident. Brightfield single-plane images showing the ASNP aggregates are black spots (indicated by arrows) are also reported. Scale bars: 10 µm (63× oil objective lens).

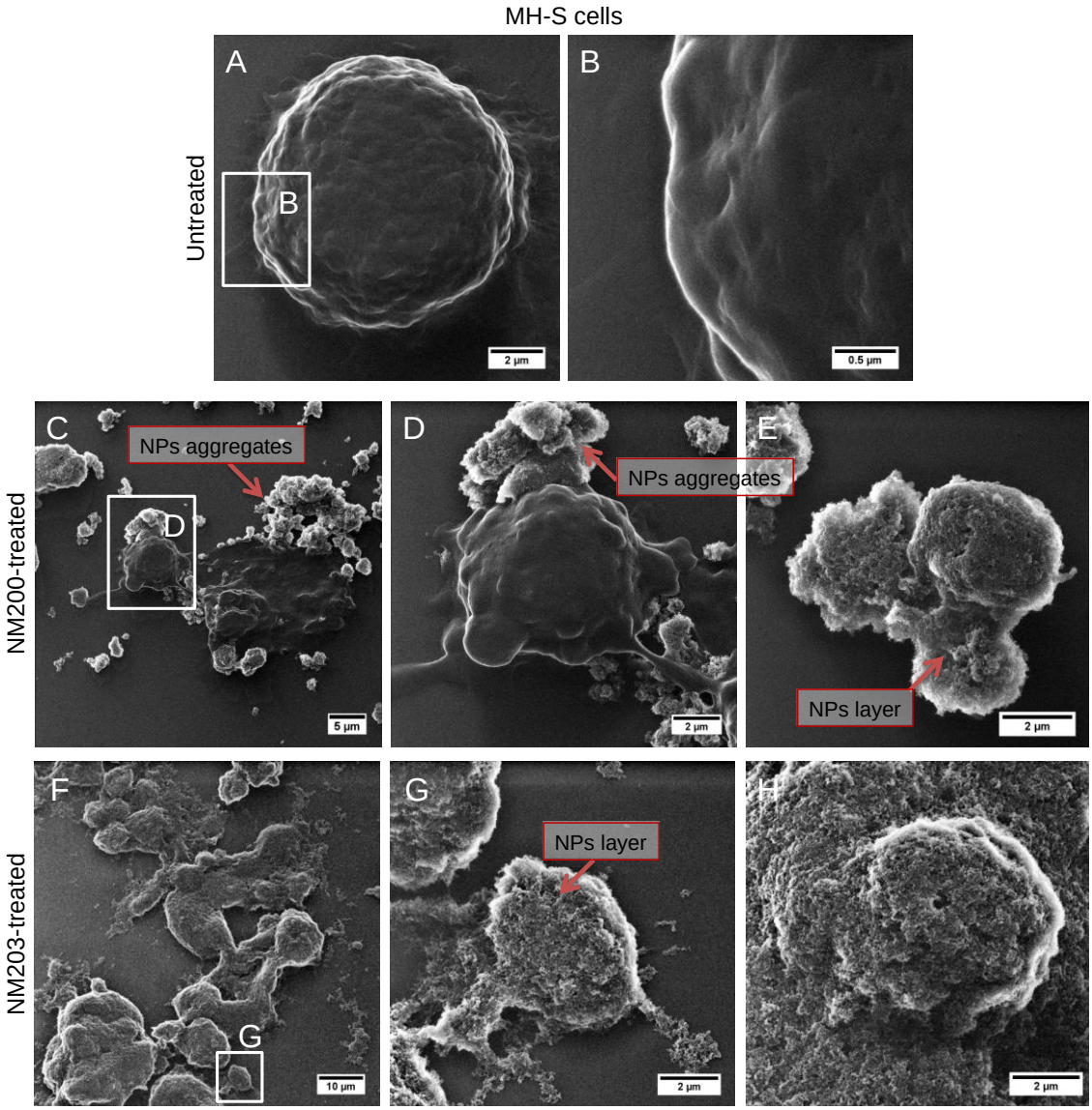

Figure 26. He-Ion Microscopy (HIM) images of MH-S. (A-B) untreated, (C-E) NM200-treated and (F-H) NM203-treated MH-S cells. (C-H) Large ASNP aggregates were visible, as well as partial or complete coverage of cell surface. Images B, D and G are magnifications of images A, C and F, respectively.

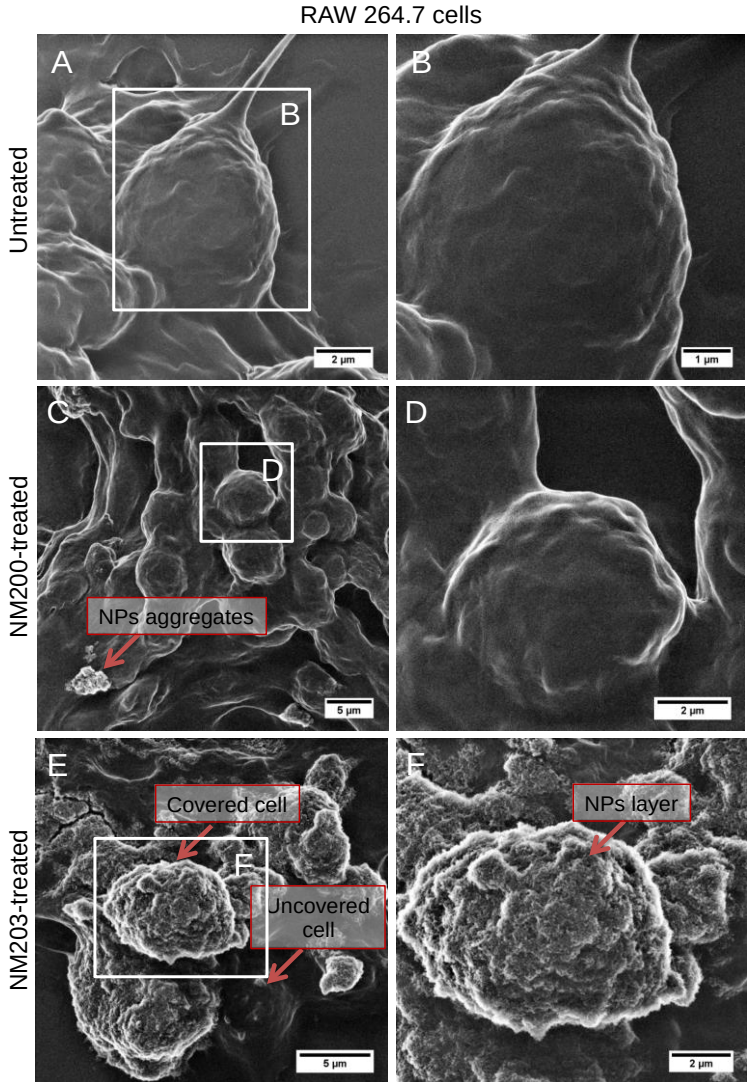

Figure 27. He-Ion Microscopy (HIM) images of RAW264.7. (A-B) untreated, (C-D) NM200-treated and (E-F) NM203-treated RAW264.7 cells. (**C-F**) Cell surface is partially or completely covered by ASNP. Images B, D and F are magnifications of images A, C and E, respectively.

6.4 Pyrogenic ASNP induce a stronger NO production than colloidal ASNP

Figure 28A reports *Nos2* mRNA expression after 24h of treatment of MH-S macrophages with non-cytotoxic doses (5 or 10 µg/cm^2) of NM200 or NM203. *Nos2* was significantly induced with either NM200 (at 10 µg/cm²) or NM203 (at both 5 and 10 µg/cm²). This effect was confirmed at protein level (Figure 28B) and corresponded to a clear cut increase in NO production (Figure 28C). In RAW264.7 cells *Nos2* messenger was modestly induced compared with control (2-fold) under all the experimental conditions (Figure 28D) but *Nos2* protein appeared barely detectable only in cells treated with NM203 and, consistently, increased accumulation of nitrites in the medium was observed only under this condition (Figure 28E-F).

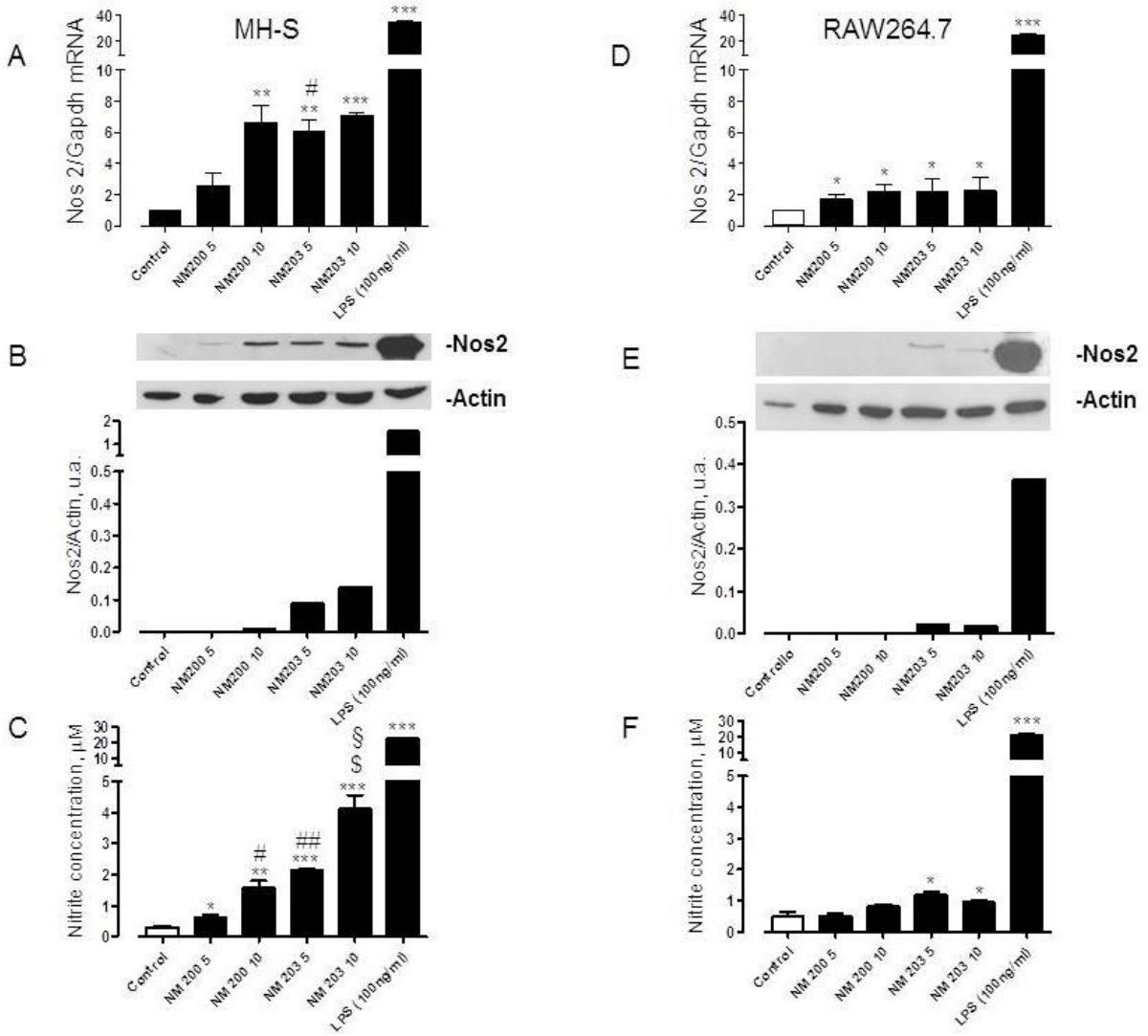

Figure 28. Effects of ASNP (NM200 and NM203) on *Nos2* expression and NO production in MH-S and RAW264.7 cells. Cells, MH-S (**A-C**) and RAW264.7 cells (**D-F**), grown for 24h in complete growth medium, were treated with 5 or 10 µg/cm^2 of NM200 and NM203, or with LPS (100 ng/ml), used as a positive control. A-D. After 24h of treatment, mRNA was extracted and the expression of *Nos2* evaluated as described in Materials and Methods B-E. The expression of the protein Nos2 was assessed through Western Blot in cultures treated in parallel and extracted after 48h of treatment. A representative blot is shown, with actin used for loading control (upper panel). In the lower panel the densitometric analysis of the same blot is shown. The experiment was performed twice with comparable results. C-F. Nitrite concentration was determined in the culture medium of the cells used for the experiment shown in B. For A and D, data are means ± S.D. of 2 independent determinations, each performed twice. For C and F, data are means of four independent determinations ± S.D. *p<0.05, **p<0.01 and ***p<0.001 *vs.* untreated, control cells. #p<0.05 and ##p<0.01 *vs.* 5 µg/cm^2 of NM200. $p<0.05 *vs.* 10 µg/cm^2 of NM200. §p<0.05 *vs.* 5 µg/cm^2 of NM203.

6.5 Secretion of pro-inflammatory cytokines in MH-S and RAW264.7 cells exposed to ASNP

The secretion of the pro-inflammatory cytokines TNF-α, IL-6 and IL-1β was quantified after the treatment of MH-S and RAW264.7 cells with NM200 and NM203 (5 or 10 μg/cm²). TNF-α, substantially absent in the medium of control cells, was readily determined after 6h of exposure to the two types of ASNP in both cell lines (Figure 29A-D). The production of IL-6 and IL-1β was assessed at longer times (after 12 and 48h of treatment, respectively). In both cell lines the exposure to ASNP produced a significant and marked increase of medium IL-6 (Figure 29B-E), which was more evident in MH-S than in RAW264.7 cells. Also IL-1β secretion (Figure 29C-F) was promoted by exposure to ASNP (again more evidently in MH-S than in RAW264.7 cells). In this case, NM203 had a markedly larger effect than NM200.

6.6. ROS production and Hmox-1 induction in ASNP-treated murine macrophages

ROS production was investigated in both macrophage lines upon a 24h-exposure to NM200 and NM203 (Figure 30). A significant, dose-dependent increase of fluorescence, an indicator of enhanced ROS production, was detectable in treated MH-S (Figure 30A) but not in RAW264.7 cells (Figure 30B). NM203 had a much higher effect than NM200 (Figure 30A), with a marked, dose dependent increase in fluorescence detected at both 5 and 10 μg/cm^2. On the contrary, NM200 promoted ROS production only at 10 μg/cm^2. The increase of fluorescence in MH-S cells treated with NM203 was also evident in fluorescence microscopy (Figure 30, bottom).

Hmox-1 (hemeoxygenase-1) is known to play a major role in the cell response to oxidative stress-mediated injuries[134]. *Hmox-1* expression was assessed after 6h of treatment with NM200 and NM203. In MH-S cells, a dose-dependent increase in expression of HO-1 messenger was evident for both ASNP, with a much higher effect with NM203 (10 and 12-fold respectively for 5 and 10 μg/cm² vs. 3 and 6-fold respectively for 5 and 10 μg/cm² for NM200) (Figure 31A). On the contrary, in RAW264.7 cells, only NM203 caused a significant increase in the expression of Hmox-1 compared with control (6 and 9-fold respectively for 5 and 10 μg/cm², Figure 31B).

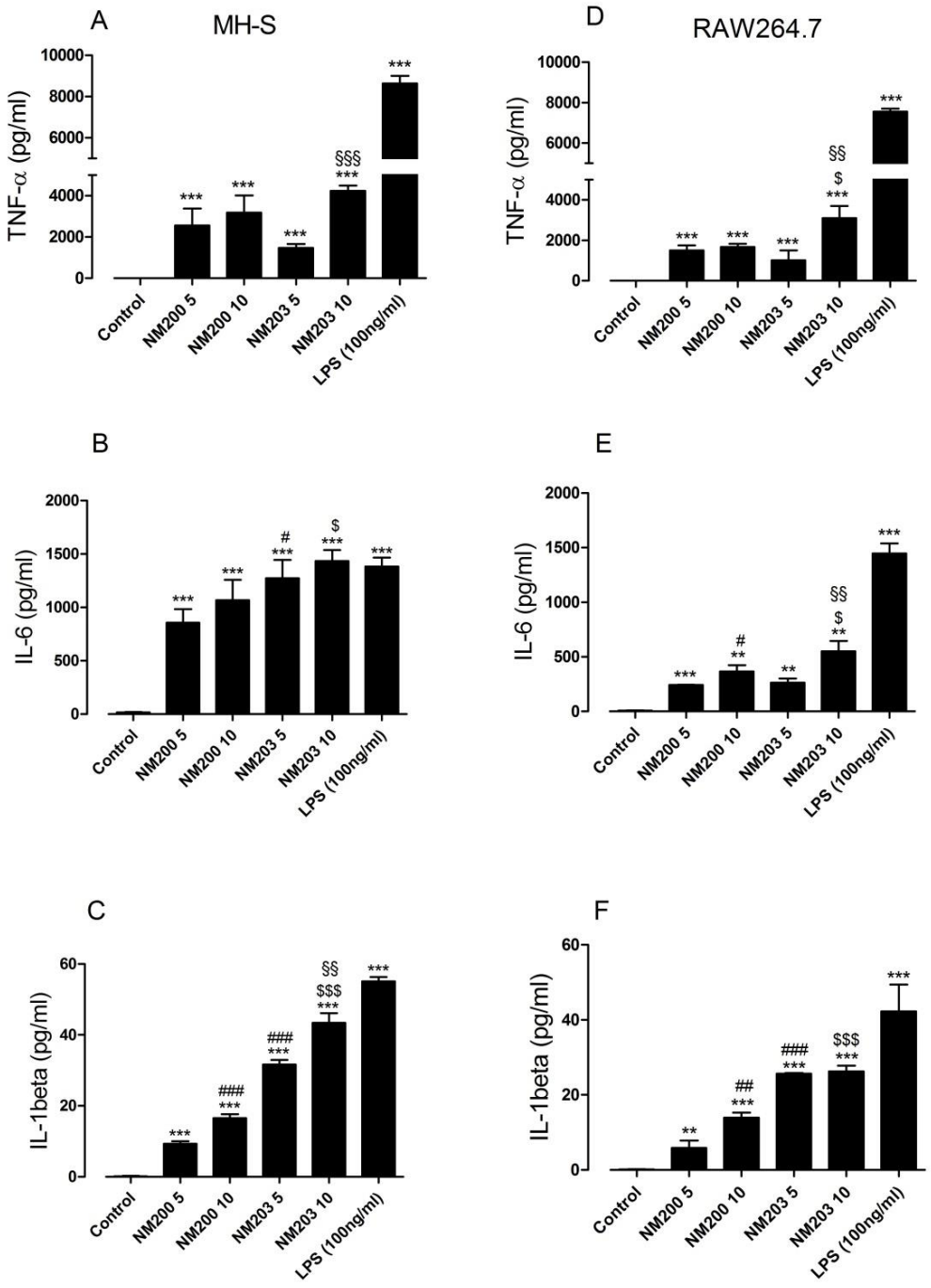

Figura 29. TNF-α, IL-6 and IL-1β secretion in MH-S and RAW264.7 cells. Cells, grown for 24h in complete growth medium, were treated with 5 or 10 μg/cm^2 of ASNP (NM200 or NM203, as indicated) or with LPS (100 ng/ml) as a positive control. After 6, 12 and 48h of treatment, the indicated cytokines were measured in the extracellular medium, as described under Materials and Methods. Panel **A**-**B**-**C**: MH-S; Panel **D**-**E**-**F**: RAW264.7. Data are means of 3 independent determinations ± S.D. **p<0.01 and ***p<0.001 vs. untreated, control cells; #p<0.05, ##p<0.01 and ###p<0.001 *vs.* 5 μg/cm^2 of NM200. $p<0.05 and $$$p<0.001 *vs.*10 μg/cm^2 of NM200. §§p<0.01 and §§§p<0.001 *vs.* 5 μg/cm^2 of NM203.

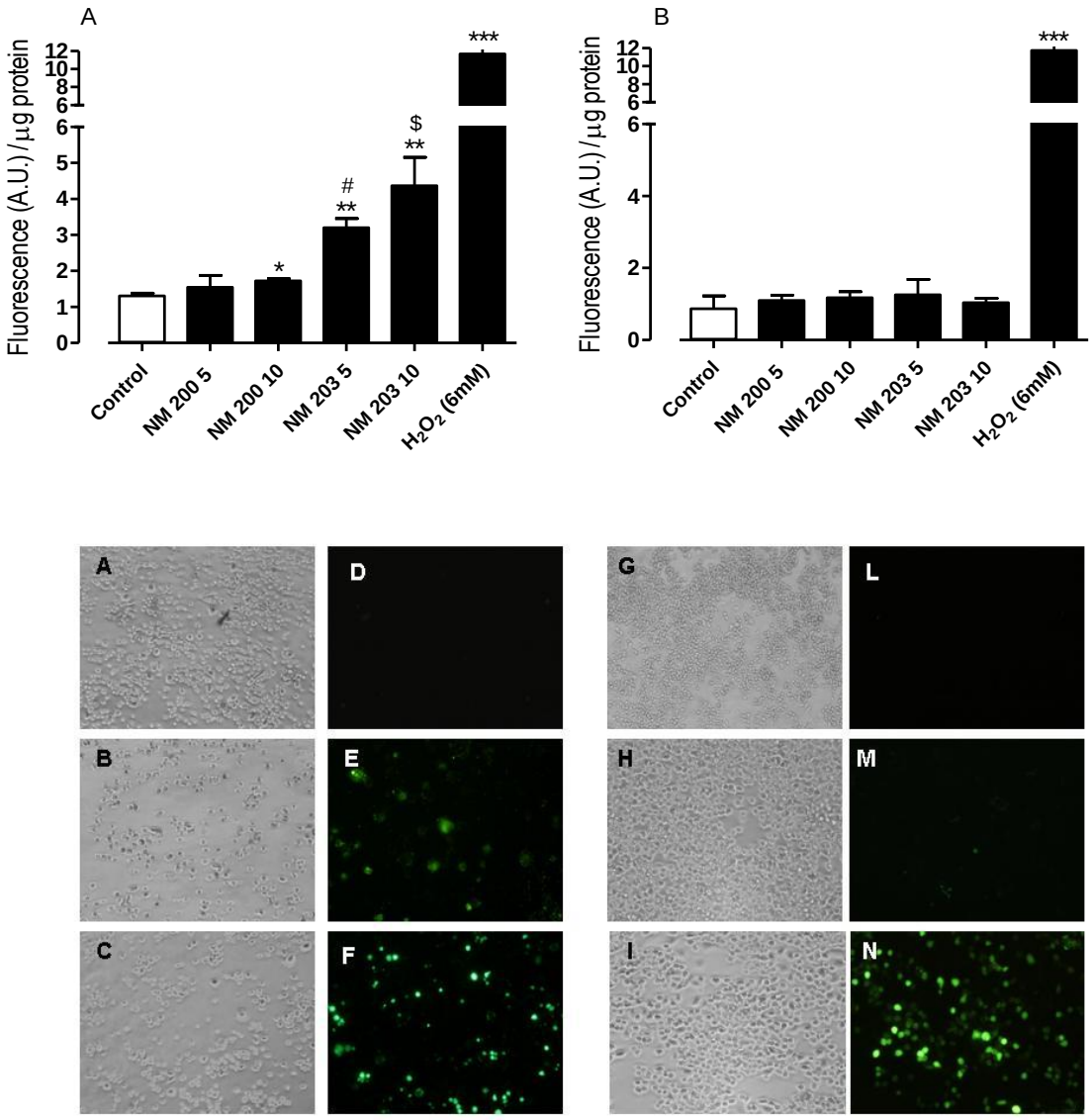

Figure 29. ROS production in MH-S and RAW264.7 cells. Cells, grown for 24h in complete growth medium, were treated with 5 or 10 µg/cm^2 of NM200 or NM203 or with H_2O_2 (6 mM), as a positive control. After 24h of treatment, cells were incubated for 2h with CM-H_2DCF-DA (5µM). Fluorescence was determined as described under Materials and Methods. Top. Panel A: MH-S; Panel B: RAW264.7. Data are means ± S.D. of 3 independent determinations, each performed twice, *p<0.05, **p<0.01 and ***p<0.001 *vs.* untreated, control cells; #p<0.05 *vs.* 5 µg/cm^2 of NM200. $p<0.05 *vs.* 10 µg/cm^2. Bottom. Before the determination of the intracellular CM-H_2 DCF-DA, images of representative fields were taken in phase contrast (A-B-C-G-H-I) or with fluorescence microscope (D-E-F-L-M-N). A,D. MH-S control, untreated cultures; B,E. MH-S, NM203 treated; C,F. MH-S, H_2O_2 treated; G,l. RAW264.7 control, untreated cultures; H,M. RAW264.7, NM203 treated; I,N. RAW264.7, H_2O_2 treated. x100.

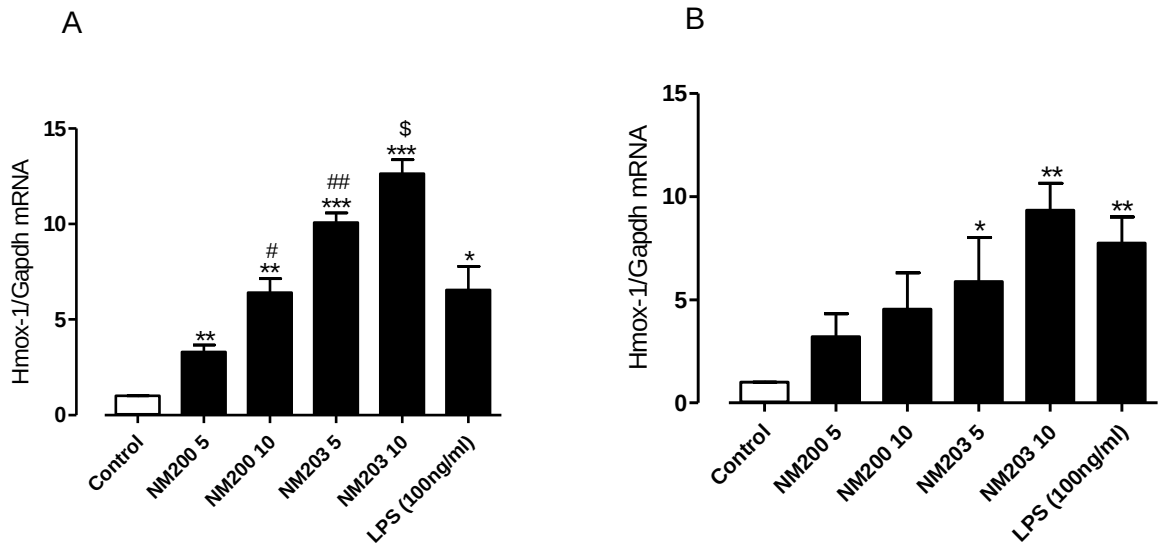

Figure 30. Effect of ASNP (NM200 and NM203) on Hmox-1 mRNA. Cells, grown for 24h in complete growth medium, were treated with 5 or 10 μg/cm^2 of NM200 or NM203 or with LPS (100 ng/ml) as a positive control. After 6h of treatment, mRNA was extracted and the expression of HO-1 evaluated as described in Materials and Methods. Panel **A**: MH-S; Panel **B**: RAW264.7. Data are means ± S.D. of 2 independent determinations, each performed twice. *p<0.05, **p<0.01 and ***p<0.001 *vs.* untreated, control cells; #p<0.05 and ###p<0.001 *vs.* 5 μg/cm^2 of NM200; $p<0.05 *vs.* 10 μg/cm^2 of NM200

6.7 ASNP enhance LPS effects on macrophage activation

The effects of a simultaneous exposure to ASNP and LPS on medium nitrite concentration, as a proxy of NO production by macrophages, is reported in Figure 8. As expected (Figure 32), at the dose employed (10 μg/cm^2) ASNP had no (NM200) or little (NM203) on NO production, which was, instead, markedly stimulated by LPS. However, the co-treatment with both ASNP caused a further, significant stimulation of NO production, with a much higher effect for NM203 (+52%) compared to NM200 (+18%).

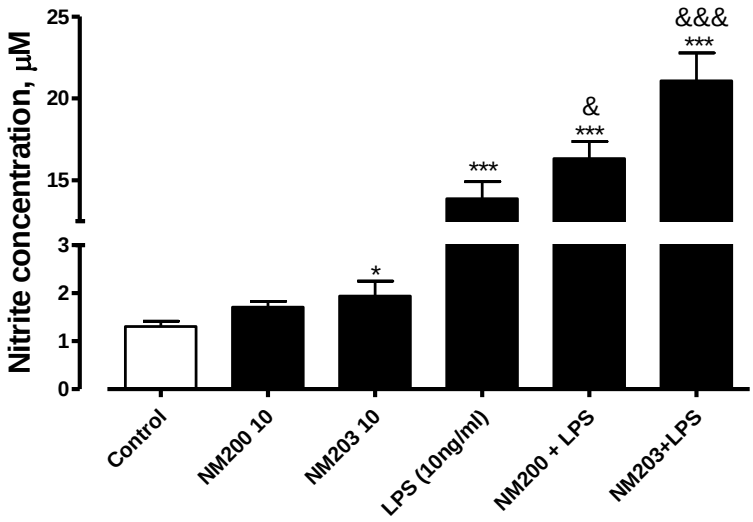

Figure 32. Synergistic effects of ASNP and LPS on nitrite production by RAW264.7 macrophages. RAW264.7 cells, grown for 24h in complete growth medium, were treated with 10 $\mu g/cm^2$ of NM200 or NM203 in the absence or in the presence of LPS (10 ng/ml). After 48h of treatment, nitrite concentration was determined in the culture medium. Data are means ± S.D. of 3 independent determinations. *p<0.05 and ***p<0.001 *vs.* untreated, control cells; &p<0.05 and &&&p<0.001 *vs.* LPS.

DISCUSSION

This part of the thesis is focused on the identification of structural toxicity determinants of two preparations of amorphous silica nanoparticles of comparable size, but produced through colloidal (NM200) or pyrogenic (NM203) processes. Here, we compare the ability of the two two preparations to exert toxic effects and to induce activation in two murine macrophage cell lines. Macrophages are particularly sensitive to ASNP compared with other cell types and are thought to play a crucial role in the toxic response to these nanomaterials[135].

6.8 Determinants of toxicity

Amorphous silica is considered to be safer than crystalline silica and is integrated in a wide variety of commercial materials for human use, such as pharmaceutical products, paints, cosmetics and food. The toxicity of crystalline silica has been studied extensively since this material is considered the toxic form of inhaled silica. For instance, it is well known that exposure to quartz particles can induce fibrotic lung alterations characterised by diffuse fibrosis and characteristic granulomas or silicotic nodules[136-137]. However, whereas crystalline silica is well defined structurally, the structure of amorphous silica is strongly dependent on kinetic and environmental factors. Due to such variety of possible ASNP structures, the toxicological behaviour of amorphous silica is not well characterized.

Several studies have reported that pyrogenic ASNP are more reactive than colloidal ASNP. In an inhalation toxicity study in Wistar rats, Art et al.[76] demonstrated that daily exposure to pyrogenic and colloidal ASNP for five consecutive day results in treatment-related adverse effects in the respiratory tract. At the highest doses used, pyrogenic silica induced more pronounced increases of lung inflammation markers than the colloidal form. Although ASNP clearance from the lung of exposed animals was rapid and inflammatory changes were transient for all the nanomaterials, histopathological changes were different for the two materials and more severe for pyrogenic ASNP. In particular, all the animals exposed to the highest dose of pyrogenic ASNP (25 mg/m^3) developed macrophage aggregates (an initial step in granuloma formation) in tracheobronchial lymph nodes, similarly to animals exposed to quartz.

High reactivity of pyrogenic ASNP for macrophages has also been described in several in vitro studies. For instance, in MH-S macrophages, pyrogenic ASNP were remarkably more active than colloidal ASNP as far as reactive oxygen species production, nitric oxide synthesis and secretion of

TNF-α are concerned[138]. Moreover, pyrogenic, but not colloidal ASNP induce a dose-dependent increase in IL-1β in THP-1 macrophages[80]. However, examples also exist in which pyrogenic ASNP are less reactive than non-pyrogenic counterparts. For instance, Sandberg et al.[139] indicate that ASNP produced by a sol-gel process elicit a greater IL-1β secretion by LPS-primed macrophages than pyrogenic counterparts, when compared on a surface basis.

The results presented in this work indicate that pyrogenic ASNP have greater cytotoxic and activating effects than colloidal counterparts on innate immunity cells. In particular, NM203 is more cytotoxic than NM200 for both the macrophage lines used, suggesting that production by thermal process is correlated to the presence of important toxicity determinants, as indicated by the lower IC_{50} values obtained for NM203. Pyrogenic ASNP also cause higher levels of oxidative stress than NM200 and trigger a clear cut anti-oxidative response at gene level.

Moreover, higher levels of all the pro-inflammatory parameters tested (Nos2 induction at both protein and gene level, NO production, TNF-α, IL-6 and Il-1β secretion, synergy with LPS) were recorded in NM203-treated cells, pointing to a significantly greater ability to promote M1-activation by pyrogenic compared with colloidal ASNP. In these experiments, non-cytotoxic or poorly cytotoxic doses (as demonstrated by viability test) were used. Importantly, although, overall, the effects were more evident in MH-S cells than in RAW 264.7, the rank of toxicity (NM203>NM200) was consistently observed for all the effects in both macrophage cell lines. These results are consistent with other recent studies that have reported higher reactivity of pyrogenic ASNP towards macrophages[80-138].

Pyrogenic ASNP generate more hydroxyl radicals than colloidal silica and, therefore, NM203, but not NM200, exibit oxidative reactivity[133]. Also Pavan et al.[78] correlated the more evident hemolytic activity of pyrogenic ASNP to their higher potential to induce ROS formation. On the other hand, it is known that the activation of inflammatory cells is associated with oxidative stress[140]. Thus, it is tempting to attribute the higher cytotoxicity and the greater pro-inflammatory responses induced by NM203 in both macrophage cell lines to higher levels of oxidative stress. Actually, pyrogenic ASNP were more powerful than colloidal ASNP as inducers of Hmox-1, one of the most sensitive and reliable indicators of the cell response to oxidative stress and a parameter linked to inflammation triggering[141-142]. Moreover, Hnox-1 induction is more evident in MH-S cells than in RAW264.7, paralleling the behaviour of pro-inflammatory parameters, thus reinforcing the hypothesis that the level of oxidative stress is linked to the strength of the pro-inflammatory activation. It is also noteworthy that the fluorescein test revealed increased intracellular ROS production only in MH-S cells, treated with NM203 (Figure 30), but neither in RAW264.7 cells nor in MH-S treated with NM200. It is important to emphasize that the absence of fluorescein-positive

ROS production and Hmox-1 induction in the same cells, as in the case of RAW264.7 cells treated with NM203, are not necessarily conflicting results. Indeed, the two assays are sensitive to different signals. While *Hmox-1* expression has been extensively regarded as an adaptive cellular response against oxidative injury by various stressors[141], the CM-H_2DCFDA assay is highly sensitive to OH• but not towards O2•- [142].

In MH-S cells exposed to ASNP, a significant, the dose-dependent increase of IL-1β, particularly evident in NM203-treated macrophages, pointed to the activation of the inflammosome, as already reported[80-138]. However, those studies were performed on monocytes-macrophages primed with phorbol esters (in the case of THP-1cells) or with LPS (in the case of RAW264.7 cells) exposed to high doses of ASNP (50-200 μg/ml). Conversely, in this study we demonstrated the activation of inflammosome in naïve macrophages exposed to relatively low doses of ASNP. Since maturation of IL-1beta is tightly regulated by NLRP3, one of the four inflammosome types, these results would suggest that even low doses of pyrogenic (and, less evidently, of colloidal) silica are able to stimulate both *Il1* expression and proIL-1β processing.

In the attempt to identify the mechanism(s) underlying the different biological reactivity of the two materials, the surface properties of pyrogenic and colloidal ASNP have been extensively studied with opposing results. One study, performed in MH-S cell, reported that colloidal and pyrogenic ASNP do not obviously differ as far as internalization is concerned, although the TEM images shown in that contribution do not allow a clear cut identification of the subcellular compartment in which NP agglomerates localize[138]. On the contrary, another study demonstrated that pyrogenic ASNP were mostly associated with the external cell surface membrane, while the colloidal ASNP were taken up by THP-1 (as well as by the bronchial epithelial BEAS-2B cells)[80]. In the present contribution, while confocal images pointed to the internalization of both NM200 and NM203, helium ion microscopy analysis showed a different interaction of ASNP with the cell surface (Figures 26 and 27). NM203 seemed to form readily detectable aggregated layers onto the plasma membrane of both macrophage lines so that the cell surface was completely covered by the nanoparticles. These data would suggest that the greater toxicity of NM203 could be due, in part, to a closer interaction with the cell surface.

Surface chemistry of NP may also determine the ability of nanomaterials to bind macromolecules present in biological media or environmental contaminants, such as the bacterial lipopolysaccharide (LPS, endotoxin). It is likely that the binding to these molecules markedly affects the bio-reactivity of the NP. For instance, as far as ASNP are concerned, Shi et al[144] recently reported that LPS and ASNP have synergistic cytotoxic and oxidative effects on A549 lung epithelial cells. Recently, we demonstrated that the interaction between TiO_2 NP and LPS strongly potentiates macrophage

activation, suggesting that the presence of environmental contaminants may enhance the pro-inflammatory activity of nanomaterials[145]. Consistently, we report here that also ASNP synergized LPS effects on macrophage activation, with a much higher effect observed for the pyrogenic NM203. This effect supports the possibility that the higher activity of pyrogenic ASNP can effectively derive from their different surface properties. If this hypothesis would be verified, an additional mechanism of toxicity may be proposed, consisting in the greater capability of pyrogenic ASNP to bind biologically active compounds, such as LPS, thus enhancing their effects. These data suggest that the toxicity of pyrogenic ASNP may be of particular concern in subjects presenting inflammatory or infectious conditions.

In conclusion, we found that the preparation route, modifying the surface properties of the NP, constitutes a main determinant of toxicity of ASNP.

CHAPTER 7

CONCLUSION

This thesis concerns the assessment of the toxic effects of ENM on the cells of innate immunity and the identification of structural determinants of toxicity. We focused our attention on two distinct types on ENM: multi walled carbon nanotubes (MWCNT) and amorphous silica nanoparticles (ASNP), both widely used in many industrial fields and produced in tonnage quantities.

The results obtained demonstrate that determinants of toxicity are strongly dependent by several parameters, mostly material-specific.

As far as MWCNT are concerned, several physico-chemical or structural properties could become a determinant of toxicity, depending on the cell type or the biological endpoint considered. For example, we reported that length and the *needle-like* shape are the main determinants of toxicity for macrophages but not for epithelial cells. For the macrophages, phagocytosis represents, at the same time, the main step for material clearance but also for cell activation. We showed that, the greater length and the needle-like shape can hinder, or even prevent, phagocytosis, whereas, reduced length and *tangle-like* shape can promote macrophage activation since these materials can be completely engulfed by macrophages. In contrast, for epithelial cells, we found that the main determinant of toxicity depends on the actual shape in which MWCNT get in contact with the cells and, in particular, if they form aggregates.

The presence of metal impurities, attributable to the synthetic procedures, is usually considered another important parameter. However, metal contaminants did not seem to be relevant under our conditions, possibly for their relatively slow dissolution in the culture medium.

As far as ASNP are concerned, our data reported that, given comparable sizes and specific surface areas, a main determinant of toxicity is the preparation route. The results presented here demonstrate indeed that pyrogenic ASNP are more toxic and potentially inflammogenic than colloidal ASNP. The toxicological profiles analyzed here suggest the greater toxicity of pyrogenic ASNP may be attributable to its framework structure and its more reactive surface chemistry, both caused by high-temperature synthesis. Moreover, we found that this surface chemistry may also increase the ability of nanomaterials to bind macromolecules present in biological media or

environmental contaminants such as the bacterial lipopolysaccharide (LPS, endotoxin), thus markedly increasing their bio-reactivity.

In conclusion, this thesis highlights that determinants of toxicity of nanomaterials are strongly dependent by several parameters, which may be specific for different groups of materials. The growing production and use of engineered nanomaterials in workplaces, the potential exposure risk for an increasing number of workers make it necessary to implement the knowledge regarding the potential biological effects. Thus, the identification of these determinants appear essential for a "safety-by-design" approach.

CHAPTER 8

REFERENCES

[1] Royal Society and Royal Academy of Engineering, UK. Nanoscience and nanotechnologies: opportunities and uncertainties. July 2004.

[2] Thomas, K., Sayre ,P.. (2005). Research strategies for safety evaluation of nanomaterials, Part I: evaluating the human health implications of exposure to nanoscale materials. *Toxicol sci*, 87(2):316-21.

[3] Oberdörster, G., Oberdörster, E., Oberdörster, J. (2005). Nanotoxicology: an emerging discipline evolving from studies of ultrafine particles. *Environmental health perspectives*, 823-839.

[4] Farré, M., Gajda-Schrantz, K., Kantiani, L., Barceló, D. (2009). Ecotoxicity and analysis of nanomaterials in the aquatic environment. *Analytical and Bioanalytical Chemistry*, *393*(1), 81-95.

[5] OECD (2008). List of manufactured nanomaterials and list of endpoints for phase one of the OECD testing programme *ENV/JM/MONO*, 13. 2.

[6] Marconi, A. (2006). Particelle fini, ultrafini e nanoparticelle in ambiente di vita e di lavoro: possibili effetti sanitari e misura dell esposizione inalatoria. *G Ital Med Lav Erg*, 28(3): 258-65.

[7] Ostiguy, C., Lapointe, G., Menard, L., Cloutier, Y., Trottier, M., Boutin, M., Antoun, M., Normand, C. (2006). Les nanoparticules: Etat des connaissances sur les risques en sante et securite du travail, rapport IRSST soumis, *IRSTT*. Montreal, Canada.

[8] Christian, P., Von der Kammer, F., Baalousha, M., Hofmann, T. (2008). Nanoparticles: structure, properties, preparation and behaviour in environmental media. *Ecotoxicology*, 17:326-43.

[9] Oberdorster, G., Maynard, A., Donaldson, K., Castranova, V., Fitzpatrick, J., Ausman, K. (2005). Principles for characterizing the potential human health effects from exposure to nanomaterials: elements of a screening strategy. *Part Fibre Toxicol*. ,2:8.

[10] ICRP (1994). International Commission on Radiological Protection: human respiratory tract model for radiological protection, Publication 66 Ann ICRP, 24 (Issues 1-3)

[11] ICRP (2002). International Commission on Radiological Protection: guide for practical application of the ICRP human respiratory tract model: ICRP supporting guidance 3. Approved by ICRP committee 2 in October 2000. Ann ICRP, 32 (issues 1-2).

[12] Bailey, M. (1994). The New ICRP Model for the Respiratory Tract. *Radiat Prot Dosimetry*, 53:107-14.

[13] BéruBé, K., Aufderheide, M., Breheny, D., Clothier, R., Combes, R., Duffin, R. (2009). In vitro models of inhalation toxicity and disease. *Alternatives to Laboratory Animals, 37*(1), 89-141.

[14] Card ,J.W., Zeldin, D.C., Bonner, J.C., Nestmann, E.R. (2008). Pulmonary applications and toxicity of engineered nanoparticles. *Am J Physiol Lung Cell Mol Physiol*., 295:L400-11.

[15] Nel, A., Xia, T., Madler, L., Li, N. (2006). Toxic potential of materials at the nanolevel. *Science*, 311: 622-7.

[16] Tsuji, J.S., Maynard, A.D., Howard, P.C., James, J.T., Lam, C.W., Warheit, D.B. (2006). Research strategies for safety evaluation of nanomaterials, part IV: risk assessment of nanoparticles. *Toxicol*

Sci., 89:42-50.

[17] Borm, P.J., Robbins, D., Haubold, S., Kuhlbusch, T., Fissan, H., Donaldson, K. (2006). The potential risks of nanomaterials: a review carried out for ECETOC. *Part Fibre Toxicol*., 3:11.

[18] Warheit, D.B. (2008). How meaningful are the results of nanotoxicity studies in the absence of adequate material characterization? *Toxicol Sci*., 101:183-5.

[19] Warheit, D.B., Sayes, C.M., Reed, K.L., Swain, K.A. (2008). Health effects related to nanoparticle exposures: environmental, health and safety considerations for assessing hazards and risks. *Pharmacol Ther.*, 120:35-42.

[20] Nel, A.E., Madler, L., Velegol, D., Xia, T., Hoek, E.M., Somasundaran, P. (2009). Understanding biophysicochemical interactions at the nano-bio interface. *Nat Mater*., 8:543-57.

[21] Yang, W., Peters, J.I., Williams III R.O. (2008). Inhaled nanoparticles - A current review. *Int J Pharm*., 356:239-47.

[22] Aillon, K.L., Xie, Y., El-Gendy, N., Berkland, C.J. (2009). Effects of nanomaterial physicochemical properties on in vivo toxicity. *Adv Drug Deliv Rev*., 61:457-66.

[23] Powers, K.W., Brown, S.C., Krishna, V.B., Wasdo, S.C., Moudgil, B.M., Roberts, S.M. (2006). Research strategies for safety evaluation of nanomaterials. Part VI. Characterization of nanoscale particles for toxicological evaluation. *Toxicol Sci*., 90:296-303.

[24] Limbach, L.K., Wick, P., Manser, P., Grass, R.N., Bruinink, A., Stark W.J. (2007). Exposure of engineered nanoparticles to human lung epithelial cells: influence of chemical composition and catalytic activity on oxidative stress. *Environ Sci Technol*., 41:4158-63.

[25] Carlotti, M.E., Ugazio, E., Sapino, S., Fenoglio, I., Greco, G., Fubini, B. (2009). Role of particle coating in controlling skin damage photoinduced by titania nanoparticles. *Free Radic Res*., 43:312-22.

[26] Clift, M.J, Rothen-Rutishauser, B., Brown, D.M., Duffin, R., Donaldson, K., Proudfoot, L. (2008). The impact of different nanoparticle surface chemistry and size on uptake and toxicity in a murine macrophage cell line. *Toxicol Appl Pharmacol*., 232:418-27

[27] Gupta, A.K., Naregalkar, R.R., Vaidya, V.D., Gupta, M. (2007). Recent advances on surface engineering of magnetic iron oxide nanoparticles and their biomedical applications. *Nanomed*, 2:23-39.

[28] Leonov,A.P., Zheng, J., Clogston, J.D., Stern, S.T., Patri, A.K., Wei A. (2008). Detoxification of gold nanorods by treatment with polystyrenesulfonate. *ACS Nano*., 2:2481-8.

[29] Mancini, M.C., Kairdolf, B.A., Smith, A.M., Nie, S. (2008). Oxidative quenching and degradation of polymerencapsulated quantum dots: new insights into the long-term fate and toxicity of nanocrystals in vivo. *J Am Chem Soc*., 130:10836-7.

[30] Nakano, K., Egashira, K., Masuda, S., Funakoshi, K., Zhao, G., Kimura, S. (2009). Formulation of nanoparticle- eluting stents by a cationic electrodeposition coating technology: efficient nano-drug delivery via bioabsorbable polymeric nanoparticle- eluting stents in porcine coronary arteries. *JACC Cardiovasc Interv*., 2:277-83.

[31] Okassa, L.N., Marchais, H., Douziech-Eyrolles, L., Herve, K., Cohen-Jonathan, S., Munnier, E. (2007). Optimization of iron oxide nanoparticles encapsulation within poly(d,l-lactide-co-glycolide) sub-micron particles. *Eur J Pharm Biopharm*., 67:31-8.

[32] Ryman-Rasmussen, J.P., Riviere, J.E., Monteiro-Riviere, N.A. (2007). Surface coatings determine cytotoxicity and irritation potential of quantum dot nanoparticles in epidermal keratinocytes. *J Invest Dermatol*., 127:143-53.

[33] Murdock, R.C., Braydich-Stolle, L., Schrand, A.M., Schlager, J.J., Hussain, S.M. (2008). Characterization of nanomaterial dispersion in solution prior to in vitro exposure using dynamic light scattering technique. *Toxicol Sci*., 101:239-53.

[34] Fadeel B., Pietroiusti A., Shvedova A.A., (2012). Adverse effects of engineered nanomaterials, exposure, toxicology, and impact on human health. Elsevier Inc.

[35] Park, M. V., Lankveld, D. P., van Loveren, H., De Jong, W. H. (2009). The status of in vitro toxicity studies in the risk assessment of nanomaterials. *Nanomedicine*, *4*(6), 669-685.

[36] Singh N., Manshian B., Jenkins G.J.S., Griffith S.M., Williams P.M., Maffeis T.G.G., Wringht C.J., Doak, S.H. (2009). Nano-Genotoxicology: the DNA damaging potential of engineered nanomaterials. *Biomaterials*, :1-24.

[37] Maynard, A.D., Baron, P.A., Foley, M., Shvedova, A.A., Kissin, E.R., Castranova, V. (2004). Exposure to carbon nanotube material: aerosol release during the handling of unrefined single-walled carbon nanotubes. *J Toxicol Environ Health*, 67:87-107.

[38] Berry, J.P., Arnoux, B., Stanislas, G., Galle, P., Chretien, J. (1997). A micro analytic study of particles transport across the alveoli: role of blood platelets. *Biomedicine*, 27(9-10):354-7.

[39] Shvedova, A.A., Kisin, E.R., Mercer, R., Murray, A.R., Johnson ,V.J., Potapovich, A.I. (2005). Unusual inflammatory and fibrogenic pulmonary responses to single-walled carbon nanotubes in mice. Am J Physiol, 289 (5):L698-L708.

[40] Zhang, L.W., Zeng, L., Barron, A.R., Monteiro-Riviere, N.A. (2007). Biological interactions of functionalized single-wall carbon nanotubes in human epidermal keratinocytes. *Int J Toxicol*., 26:103-13.

[41] Chappert, P., Schwartz, R. H. (2010). Induction of T cell anergy: integration of environmental cues and infectious tolerance. *Current opinion in immunology*,*22*(5), 552-559

[42] Sakaguchi, S. (2011). Regulatory T cells: history and perspective. In*Regulatory T Cells* (pp. 3-17). Humana Press

[43] Labarre, D., Vauthier, C., Chauvierre, C., Petri, B., Muller, R., Chehimm, M.M. (2005). Interactions of blood proteins with poly (isobutylcyanoacrylate) nanoparticles decorated with a polysaccharidic brush. *Biomaterials*, 26: 5075-81.

[44] Moghim, S.M., Patel, H.M. (1998). Serum-mediated recognition of liposomes by phagocytic cells of the reticuloendothelial system. The concept of tissue specificity. *Adv Drug Delivery Rev*., 32:45-61.

[45] Koyama, S., Endo, M., Kim, Y-A, Hayashi, T., Yanagisawa, T., Osaka, K., Koyama, H., Haniu, H., Kuroiwa, N. (2006). Role of systemic T-cells and histopathological aspects after subcutaneous implantation of various carbon nanotubes in mice. *Carbon*., 44:1079-92.

[46] Linse, S., Cabaleiro-Lago, C., Xue, W-F, Lynch, I., Lindman, S., Thulin, E., Radford, S.E., Dawson, K.A. (2007). Nucleation of protein fibrillation by nanoparticles. PNAS., 8691-7.

[47] Park, E. J., Bae, E., Yi, J., Kim, Y., Choi, K., Lee, S. H., Park K. (2010). Repeated-dose toxicity and inflammatory responses in mice by oral administration of silver nanoparticles. *Environmental toxicology and pharmacology*, *30*(2), 162-168.

[48] Zhang, X. D., Wu, H. Y., Wu, D., Wang, Y. Y., Chang, J. H., Zhai, Z. B., Fan, F. Y. (2010). Toxicologic effects of gold nanoparticles in vivo by different administration routes. *International journal of nanomedicine*, *5*, 771.

[49] Kim, Y. S., Song, M. Y., Park, J. D., Song, K. S., Ryu, H. R., Chung, Y. H., Yu, I. J. (2010). Subchronic oral toxicity of silver nanoparticles. *Particle and fibre toxicology*, *7*(1), 20.

[50] Chen, Z., Meng, H., Xing, G., Chen, C., Zhao, Y., Jia, G., ... & Wan, L. (2006). Acute toxicological effects of copper nanoparticles in vivo. *Toxicology letters*,*163*(2), 109-120.

[51] Meng, H., Chen, Z., Xing, G., Yuan, H., Chen, C., Zhao, F., ... & Zhao, Y. (2007). Ultrahigh reactivity provokes nanotoxicity: explanation of oral toxicity of nano-copper particles. *Toxicology letters*, *175*(1), 102-110.

[52] Gerloff, K., Albrecht, C., Boots, A. W., Förster, I., & Schins, R. P. (2009). Cytotoxicity and oxidative DNA damage by nanoparticles in human intestinal Caco-2 cells. *Nanotoxicology*, *3*(4), 355-364.

[53] Bastian S., Busch W., Kuhnel D. (2009). Toxicity of tungsten carbide and cobalt-doped tungsten carbide nanoparticles in mammalian cells *in vitro*. *Environ Health Perspect*, 117:530-6.

[54] Limor, H. A., James, K. C., Rafi, K., Patrice, N. M., Oded, M., Jessica, P., ... & Christian, V. (2011). Predictive toxicology of cobalt nanoparticles and ions: comparative in-vitro study of different cellular models using methods of knowledge discovery from data. *Toxicological Sciences*, 122:489-501.

[55] Kayat, J., Gajbhiye, V., Tekade, R. K., Jain, N. K. (2011). Pulmonary toxicity of carbon nanotubes: a systematic report. *Nanomedicine: Nanotechnology, Biology and Medicine*, *7*(1), 40-49.

[56] Jorio, A., Saito, R., Hafner, J. H., Lieber, C. M., Hunter, M., McClure, T., Dresselhaus, M. S. (2001). Structural (n, m) determination of isolated single-wall carbon nanotubes by resonant Raman scattering. *Physical Review Letters*,*86*(6), 1118.

[57] Hou, P. X., Xu, S. T., Ying, Z., Yang, Q. H., Liu, C., Cheng, H. M. (2003). Hydrogen adsorption/desorption behavior of multi-walled carbon nanotubes with different diameters. *Carbon*, *41*(13), 2471-2476.

[58] Popov, V. N. (2004). Carbon nanotubes: properties and application. *Materials Science and Engineering: R: Reports*, *43*(3), 61-102.

[59] De Heer, W. A., Chatelain, A., Ugarte, D. (1995). A carbon nanotube field-emission electron source. *Science*, *270*(5239), 1179-1180.

[60] Kempa, K., Kimball, B., Rybczynski, J., Huang, Z. P., Wu, P. F., Steeves, D., Ren, Z. F. (2003). Photonic crystals based on periodic arrays of aligned carbon nanotubes. *Nano Letters*, *3*(1), 13-18.

[61] O'connell, M. J., Bachilo, S. M., Huffman, C. B., Moore, V. C., Strano, M. S., Haroz, E. H., Smalley, R. E. (2002). Band gap fluorescence from individual single-walled carbon nanotubes. *Science*, *297*(5581), 593-596.

[62] Cherukuri, P., Bachilo, S. M., Litovsky, S. H., Weisman, R. B. (2004). Near-infrared fluorescence microscopy of single-walled carbon nanotubes in phagocytic cells. *Journal of the American Chemical Society*, *126*(48), 15638-15639.

[63] Donaldson, K., Murphy, F. A., Duffin, R., Poland, C. A. (2010). Asbestos, carbon nanotubes and the pleural mesothelium: a review of the hypothesis regarding the role of long fibre retention in the parietal pleura, inflammation and mesothelioma. *Part Fibre Toxicol*, *7*(5), 5.

[64] Kreyling, W. G., Möller, W., Semmler-Behnke, M., Oberdörster, G. (2007). Particle dosimetry: deposition and clearance from the respiratory tract and translocation towards extra-pulmonary sites. *Particle toxicology*, 2007.

[65] Schlesinger, R. B., Ben-Jebria, A., Dahl, A. R., Snipes, M. B., Ultman, J. (1997). Disposition of inhaled toxicants. *Handbook of human toxicology*, 493-550.

[66] Searl, A., Buchanan, D., Cullen, R. T., Jones, A. D., Miller, B. G., Soutar, C. A. (1999). Biopersistence and durability of nine mineral fibre types in rat lungs over 12 months. *Annals of Occupational Hygiene*, *43*(3), 143-153.

[67] Hesterberg, T. W., Miiller, W. C., Musselman, R. P., Kamstrup, O., Hamilton, R. D., Thevenaz, P. (1996). Biopersistence of man-made vitreous fibers and crocidolite asbestos in the rat lung following inhalation. *Fundamental And Applied Toxicology*, *29*(2), 267-279.

[68] Poland, C. A., Duffin, R., Kinloch, I., Maynard, A., Wallace, W. A., Seaton, A., Donaldson, K. (2008). Carbon nanotubes introduced into the abdominal cavity of mice show asbestos-like pathogenicity in a pilot study. *Nature nanotechnology*, *3*(7), 423-428.

[69] Nagai, H., Okazaki, Y., Chew, S. H., Misawa, N., Yamashita, Y., Akatsuka, S.,Toyokuni, S. (2011). Diameter and rigidity of multiwalled carbon nanotubes are critical factors in mesothelial injury and carcinogenesis. *Proceedings of the National Academy of Sciences*, *108*(49), E1330-E1338.

[70] Fenoglio,I., Aldieri, E., Gazzano, E., Cesano, F., Colonna, M., Scarano, D., Mazzucco, G., Attanasio, A., Yakoub, Y., Lison, B., Fubini, I. (2012). Thickness of multiwalled carbon nanotubes affects their lung toxicity. *Chem. Res. Toxicol*, 25, 74-82.

[71] Greenberg, M. I., Waksman, J.,Curtis, J. (2007). Silicosis: a review. *Disease-a-Month*, *53*(8), 394-416.

[72] Merget, R., Bauer, T., Küpper, H., Philippou, S., Bauer, H., Breitstadt, R., Bruening, T. (2002). Health hazards due to the inhalation of amorphous silica. *Archives of toxicology*, *75*(11-12), 625-634.

[73] Reiser K.M., Last J.A. (1979). Silicosis and fibrogenesis: fact and artifact. *Toxicology*, 13,51-72.

[74] Koskela, R. S., Klockars, M., Laurent, H., Holopainen, M. (1994). Silica dust exposure and lung cancer. *Scandinavian journal of work, environment & health*, 407-416.

[75] ECETOC, 2006. Synthetic Amorphous Silica (CAS No. 7631-86-9), Joint Assessment of Commodity Chemicals (JACC) report No. 51, M. Gribble (Ed.), Brussels, Belgium.

[76] Arts, J. H., Muijser, H., Duistermaat, E., Junker, K., Kuper, C. F. (2007). Five-day inhalation toxicity study of three types of synthetic amorphous silicas in Wistar rats and post-exposure evaluations for up to 3months. *Food and chemical toxicology*, *45*(10), 1856-1867.

[77] Ambrosone, A., di Vettimo, M. R. S., Malvindi, M. A., Roopin, M., Levy, O., Marchesano, V., Tino, A. (2014). Impact of Amorphous SiO2 Nanoparticles on a Living Organism: Morphological, Behavioral, and Molecular Biology Implications. *Frontiers in bioengineering and biotechnology*, *2*.

[78] Pavan, C., Tomatis, M., Ghiazza, M., Rabolli, V., Bolis, V., Lison, D., Fubini, B. (2013). In Search of the Chemical Basis of the Hemolytic Potential of Silicas. *Chemical research in toxicology*, *26*(8), 1188-1198.

[79] Kaewamatawong, T., Kawamura, N., Okajima, M., Sawada, M., Morita, T., & Shimada, A. (2005). Acute pulmonary toxicity caused by exposure to colloidal silica: particle size dependent pathological changes in mice. *Toxicologic pathology*, *33*(7), 745-751.

[80] Zhang H.Y., Dunphy D.R., Jiang X.M, Meng H., Sun B.B., Tarn D., Xue M., Wang X., Lin S.J., Ji Z.X., Li RB., Garcia F.L., Yang J., Kirk M.L., Xia T., Zink J.I. Nel A. *Brinker CJ:* Processing pathway dependence of amorphous silica nanoparticle toxicity: colloidal vs pyrolytic. *J Am Chem Soc*. 134:15790–15804, 2012.

[81] NANOGENOTOX - Final protocol for producing suitable manufactured nanomaterial exposure media (Standard Operation Procedure), 2011.

[82] O'Brien, J., Wilson, I., Orton, T., Pognan, F. (2000). Investigation of the Alamar Blue (resazurin) fluorescent dye for the assessment of mammalian cell cytotoxicity. *Eur J Biochem*, 267:5421-5426

[83] Barilli, A., Rotoli, BM., Visigalli, R., Bussolati, O., Gazzola, GC., Gatti, R., Dionisi-Vici, C., Martinelli, D., Goffredo, BM., Font-Llitjóse M., Mariani, F., Luisetti, M., Dall'Asta, V. (2012). Impaired phagocytosis in macrophages from patients affected by lysinuric protein intolerance. *Molecular Genetics and Metabolism*, 105, 585–589.

[84] Bustin, S. A. (2000). Absolute quantification of mRNA using real-time reverse transcription polymerase chain reaction assays. *Journal of molecular endocrinology*, *25*(2), 169-193.

[85] Sala, R., Rotoli, B. M., Colla, E., Visigalli, R., Parolari, A., Bussolati, O., Gazzola, G. C., Dall'Asta V. (2002). Two-way arginine transport in human endothelial cells: TNF-alpha stimulation is restricted to system y(+). *Am J Physiol Cell Physiol*, 282, C134-143.

[86] Salem, L. B., Bosquillon, C., Dailey, L. A., Delattre, L., Martin, G. P., Evrard, B., Forbes, B. (2009). Sparing methylation of β-cyclodextrin mitigates cytotoxicity and permeability induction in respiratory epithelial cell layers< i> in vitro</i>. *Journal of Controlled Release*, *136*(2), 110-116.

[87] Gatti, R., Orlandini, G., Uggeri, J., Belletti, S., Galli, C., Raspanti M. (2008). Analysis of living cells grown on different titanium surfaces by time-lapse confocal microscopy. Micron, 39:137-143.

[88] Scholzen, T., Gerdes, J. (2000). The Ki-67 protein: from the known and the unknown. *Journal of cellular physiology*, 182(3), 311-322.

[89] Bell, DC. (2009). Contrast mechanisms and image formation in helium ion microscopy. *Microscopy and Microanalysis*, *15*(02), 147-153.

[90] Rasmussen K. , Mast J., De Temmerman P-J, Verleysen E., Waegeneers N., Van Steen F., Pizzolon J. C.,, De Temmerman L., Van Doren E., Jensen K.A., Birkedal R. et al. (2014). Multi-walled Carbon Nanotubes, NM-400, NM-401, NM-402, NM-403: Characterisation and Physico-Chemical Properties. 44 JRC Repository: NM-series of Representative Manufactured Nanomaterials. In: JRC Scientific and Policy Reports. ISBN 978-92-79-39648-9, EUR 26796 EN.

[91] Rotoli BM., Gatti R., Movia D., Bianchi MG., Di Cristo L., Fenoglio I., Sonvico F., Bergamaschi E., Prina-Mello A., Bussolati O. (2014). Identifying contact-mediated, localized toxic effects of MWCNT aggregates on epithelial monolayers: A single-cell monitoring toxicity assay. *Nanotoxicology*, 29:1-12.

[92] Lawrence, T. (2009). The nuclear factor NF-κB pathway in inflammation. *Cold Spring Harbor perspectives in biology*, *1*(6), a001651.

[93] Bussy, C., Pinault, M., Cambedouzou, J., Landry, M. J., Jegou, P., Mayne-L'hermite, M., Lanone, S. (2012). Critical role of surface chemical modifications induced by length shortening on multi-walled carbon nanotubes-induced toxicity. *Part Fibre Toxicol*, *9*(46), 1-15.

[94] Poland, C. A., Duffin, R., Kinloch, I., Maynard, A., Wallace, W. A., Seaton, A., Donaldson, K. (2008). Carbon nanotubes introduced into the abdominal cavity of mice show asbestos-like pathogenicity in a pilot study. *Nature nanotechnology*, *3*(7), 423-428.

[95] Murphy, F. A., Poland, C. A., Duffin, R., Al-Jamal, K. T., Ali-Boucetta, H., Nunes, A., Donaldson, K. (2011). Length-dependent retention of carbon nanotubes in the pleural space of mice initiates sustained inflammation and progressive fibrosis on the parietal pleura. *The American journal of pathology*,*178*(6), 2587-2600.

[96] Fenoglio, I., Aldieri, E., Gazzano, E., Cesano, F., Colonna, M., Scarano, D., Fubini, B. (2011). Thickness of multiwalled carbon nanotubes affects their lung toxicity. *Chemical research in toxicology*, *25*(1), 74-82.

[97] Nagai, H., Okazaki, Y., Chew, S. H., Misawa, N., Yamashita, Y., Akatsuka, S., Toyokuni, S. (2011). Diameter and rigidity of multiwalled carbon nanotubes are critical factors in mesothelial injury and carcinogenesis.*Proceedings of the National Academy of Sciences*, *108*(49), E1330-E1338.

[98] Jacobsen, N. R., Pojana, G., White, P., Møller, P., Cohn, C. A., Smith Korsholm, K., Wallin, H. (2008). Genotoxicity, cytotoxicity, and reactive oxygen species induced by single-walled carbon nanotubes and C60 fullerenes in the FE1-Muta™ Mouse lung epithelial cells. *Environmental and molecular mutagenesis*, *49*(6), 476-487.

[99] Pacurari, M., Yin, X. J., Zhao, J., Ding, M., Leonard, S. S., Schwegler-Berry, D., Vallyathan, V. (2008). Raw single-wall carbon nanotubes induce oxidative stress and activate MAPKs, AP-1, NF-kappaB, and Akt in normal and malignant human mesothelial cells. *Environ Health Perspect*, *116*(9), 1211-1217.

[100] Lee, J.K., Sayers, B.C., Chun, K.S., Lao, H.C., Shipley-Phillips, J.K., Bonner, J.C., Robert Langenbach, R. (2012). Multi-walled carbon nanotubes induce COX-2 and iNOS expression via MAP Kinase-dependent and -independent mechanisms in mouse RAW264.7 macrophages. *Particle and Fibre Toxicology*, 9:14.

[101] Smart, S.K., Cassady, A.I., Lu, G.Q., Martin, D.J. (2006). The biocompatibility of carbon nanotubes. *Carbon* 44: 1034-1047.

[102] Matter, K., Balda, M.S. (2007). Epithelial tight junctions, gene expression and nucleo-junctional interplay. *J Cell Sci* 120: 1505-1511.

[103] Cereijido, M., Contreras, R.G., Shoshani, L., Flores-Benitez, D., Larre, I. (2008). Tight junction and polarity interaction in the transporting epithelial phenotype. *Biochim Biophys Acta* 1778: 770-793.

[104] Sakagami, M. (2006). In vivo, in vitro and ex vivo models to assess pulmonary absorption and disposition of inhaled therapeutics for systemic delivery. *Adv Drug Deliv Rev* 58: 1030-1060.

[105] Teijeiro-Osorio, D., Remunan-Lopez, C., Alonso, M.J. (2009). New generation of hybrid poly/oligosaccharide nanoparticles as carriers for the nasal delivery of macromolecules. *Biomacromolecules* 10: 243-249.

[106] Grainger, C.I., Greenwell, L.L., Martin, G.P., Forbes, B. (2009). The permeability of large molecular weight solutes following particle delivery to air-interfaced cells that model the respiratory mucosa. *Eur J Pharm Biopharm* 71: 318-324.

[107] Daum, N., Neumeyer, A., Wahl, B., Bur, M., Lehr, C.M. (2009). In vitro systems for studying epithelial transport of macromolecules. *Methods Mol Biol* 480: 151-164.

[108] Muller, J., Huaux, F., Moreau, N. et al. (2005). Respiratory toxicity of multi-wall carbon nanotubes. *Toxicol Appl Pharmacol* 207: 221-231.

[109] Rotoli, B.M., Bussolati, O., Bianchi, M.G., Barilli, A., Balasubramanian, C., Bellucci, S., Bergamaschi, E. (2008). Non-functionalized multi-walled carbon nanotubes alter the paracellular permeability of human airway epithelial cells. *Toxicol Lett* 178: 95-102.

[110] Kishore, A.S., Surekha, P., Murthy, P.B. (2009). Assessment of the dermal and ocular irritation potential of multi-walled carbon nanotubes by using in vitro and in vivo methods. *Toxicol Lett* 191: 268-274.

[111] Park, E.J., Cho, W.S., Jeong, J., Yi, J., Choi, K., Park, K. (2009). Pro-inflammatory and potential allergic responses resulting from B cell activation in mice treated with multi-walled carbon nanotubes by intratracheal instillation. *Toxicology* 259: 113-121.

[112] Reddy, A.R., Reddy, Y.N., Krishna, D.R., Himabindu, V. (2010). Pulmonary toxicity assessment of multiwalled carbon nanotubes in rats following intratracheal instillation. *Environ Toxicol* 27: 211-219.

[113] Pauluhn, J. (2009). Comparative pulmonary response to inhaled nanostructures: considerations on test design and endpoints. *Inhal Toxicol* 21 Suppl 1: 40-54.

[114] Murphy, F.A., Poland, C.A., Duffin, R. et al. (2011). Length-dependent retention of carbon nanotubes in the pleural space of mice initiates sustained inflammation and progressive fibrosis on the parietal pleura. *The American journal of pathology* 178: 2587-2600

[115] Donaldson, K., Aitken, R., Tran, L., Stone, V., Duffin, R., Forrest, G., Alexander, A. (2006). Carbon nanotubes: a review of their properties in relation to pulmonary toxicology and workplace safety. *Toxicol Sci* 92: 5-22.

[116] Carrero-Sanchez, J.C., Elias, A.L., Mancilla, R., Arrellin, G., Terrones, H., Laclette, J.P., Terrones, M. (2006). Biocompatibility and toxicological studies of carbon nanotubes doped with nitrogen. *Nano Lett* 6: 1609-1616.

[117] Maynard, A.D., Baron, P.A., Foley, M., Shvedova, A.A., Kisin, E.R., Castranova, V. (2004). Exposure to carbon nanotube material: aerosol release during the handling of unrefined single-walled carbon nanotube material. *J Toxicol Environ Health* A 67: 87-107.

[118] Mutlu, G.M., Budinger, G.R., Green, A.A. et al. (2010). Biocompatible nanoscale dispersion of single-walled carbon nanotubes minimizes in vivo pulmonary toxicity. *Nano Lett* 10: 1664-1670.

[119] Murray, A.R., Kisin, E.R., Tkach, A.V., Yanamala, N., Mercer, R., Young, S.H., Fadeel, B., Kagan, V.E., Shvedova, A.A. (2012). Factoring-in agglomeration of carbon nanotubes and nanofibers for better prediction of their toxicity versus asbestos. *Part Fibre Toxicol* 9: 10.

[120] Pulskamp, K., Diabate, S., Krug, H.F. (2007). Carbon nanotubes show no sign of acute toxicity but induce intracellular reactive oxygen species in dependence on contaminants. *Toxicol Lett* 168: 58-74.

[121] Casey, A., Herzog, E., Lyng, F.M., Byrne, H.J., Chambers, G., Davoren, M. (2008). Single walled carbon nanotubes induce indirect cytotoxicity by medium depletion in A549 lung cells. *Toxicol Lett* 179: 78-84.

[122] Worle-Knirsch, J.M., Pulskamp, K., Krug, H.F.(2006). Oops they did it again! Carbon nanotubes hoax scientists in viability assays. *Nano Lett* 6: 1261-1268.

[123] Holt, B.D., Short, P.A., Rape, A.D., Wang, Y.L., Islam, M.F., Dahl, K.N. (2010). Carbon nanotubes reorganize actin structures in cells and ex vivo. *Acs Nano* 4: 4872-4878.

[124] Vogel, V., Sheetz, M. (2006). Local force and geometry sensing regulate cell functions. *Nat Rev Mol Cell Biol* 7: 265-275.

[125] Vogel, V., Sheetz, M.P. (2009). Cell fate regulation by coupling mechanical cycles to biochemical signaling pathways. *Curr Opin Cell Biol* 21: 38-46.

[126] Cui, D., Tian, F., Ozkan, C.S., Wang, M., Gao, H. (2005). Effect of single wall carbon nanotubes on human HEK293 cells. *Toxicol Lett* 155: 73-85.

[127] Lu, J., Rao, M.P., MacDonald, N.C., Khang, D., Webster, T.J. (2008). Improved endothelial cell adhesion and proliferation on patterned titanium surfaces with rationally designed, micrometer to nanometer features. *Acta Biomater* 4: 192-201.

[128] Gilmore, A.P. (2005). Anoikis. *Cell Death Differ* 12 Suppl 2: 1473-1477.

[129] Ma-Hock, L., Treumann, S., Strauss, V. et al. (2009). Inhalation toxicity of multiwall carbon nanotubes in rats exposed for 3 months. *Toxicol Sci* 112: 468-481.

[130] Thubagere, A., Reinhard, B.M. (2010). Nanoparticle-induced apoptosis propagates through hydrogen-peroxide-mediated bystander killing: insights from a human intestinal epithelium in vitro model. *Acs Nano* 4: 3611-3622.

[131] Pauluhn, J. (2010). Subchronic 13-week inhalation exposure of rats to multiwalled carbon nanotubes: toxic effects are determined by density of agglomerate structures, not fibrillar structures. *Toxicol Sci* 113: 226-242.

[132] Pescatori, M., Bedognetti, D., Venturelli, E., Ménard-Moyon, C., Bernardini, C., Muresu, E., Delogu, L.G. (2013). Functionalized carbon nanotubes as immunomodulator systems. *Biomaterials*, *34*(18), 4395-4403.

[133] Rasmussen, K., Mech , A., Mast, J., De Temmerman P.J., Waegeneers , N., Van Steen , F., Pizzolon, JC., De Temmerman L., Van Doren, E., et al. (2013). Synthetic Amorphous Silicon Dioxide (NM-200, NM-201, NM-202, NM-203, NM-204): Characterisation and Physico-Chemical

Properties. JRC Repository: NM-series of Representative Manufactured Nanomaterials. ISBN 978-92-79-32323-2. EUR 26046 EN.

[134] Bhaskaran, N., Shukla, S., Kanwal, R., Srivastava, J.K., Gupta, S. (2012). Induction of heme oxygenase-1 by chamomile protects murine macrophages against oxidative stress. *Life Sciences* 90, 1027–1033.

[135] Costantini, L.M., Gilberti, R.M., Knecht, D.A. (2011). The phagocytosis and toxicity of amorphous silica. *PLoS One* 6(2):e14647.

[136] Mossman, B.T., Churg, A. (1998). Mechanisms in the pathogenesis of asbestosis and silicosis. *Am J Respir Crit Care Med* 157:1666-1680

[137] Weill, H., Jones, R.N., Parkes, W.R. (1994). Silicosis and related diseases. *Occupational lung disorders.* 3rd ed. London: Butterworth-Heinemann Ltd, 285-339.

[138] Gazzano, E., Ghiazza, M., Polimeni, M., Bolis, V., Fenoglio, I., Attanasio, A., Ghigo, D. (2012). Physico-chemical determinants in the cellular responses to nanostructured amorphous silicas. *Toxicological Sciences*, kfs128.

[139] Sandberg, W. J., Lag, M., Holme, J. A., Friede, B., Gualtieri, M., Kruszewski, M., Refsnes, M. (2012). Comparison of non-crystalline silica nanoparticles in IL-1beta release from macrophages. *Part Fibre Toxicol*, *9*(1), 32.

[140] Park, E. J., Park, K. (2009). Oxidative stress and pro-inflammatory responses induced by silica nanoparticles in vivo and in vitro. *Toxicology letters*, *184*(1), 18-25.

[141] Poss, K. D., Tonegawa, S. (1997). Reduced stress defense in heme oxygenase 1-deficient cells. *Proceedings of the National Academy of Sciences*, *94*(20), 10925-10930.

[142] Naito, Y., Takagi, T., Higashimura, Y. (2014). Heme oxygenase-1 and anti-inflammatory M2 macrophages. *Archives of biochemistry and biophysics*, *564*, 83-88.

[143] Forkink, M., Smeitink, J. A., Brock, R., Willems, P. H., Koopman, W. J. (2010). Detection and manipulation of mitochondrial reactive oxygen species in mammalian cells. *Biochimica et Biophysica acta (BBa)-Bioenergetics*, *1797*(6), 1034-1044.

[144] Shi, Y., Yadav, S., Wang, F., Wang, H. (2010). Endotoxin promotes adverse effects of amorphous silica nanoparticles on lung epithelial cells in vitro.*Journal of Toxicology and Environmental Health, Part A*, *73*(11), 748-756.

[145] Bianchi, M.G., Allegri, M., Costa, A.L., Blosi, M., Gardini, D., Del Pivo, C., Prina Mello, A., Di Cristo, L., Bussolati, O., Bergamaschi, E. (2014). Titanium dioxide nanoparticles enhance macrophage activation by LPS through a TLR4-dependent intracellular pathway. DOI:10.1039/C4TX00193A.